



HAL
open science

ANALYSIS AND OPTIMIZATION OF DENSE GAS FLOWS: APPLICATION TO ORGANIC RANKINE CYCLES TURBINES

Pietro Marco Congedo

► **To cite this version:**

Pietro Marco Congedo. ANALYSIS AND OPTIMIZATION OF DENSE GAS FLOWS: APPLICATION TO ORGANIC RANKINE CYCLES TURBINES. Modeling and Simulation. Università degli studi di Lecce, 2007. English. NNT: . tel-00349762

HAL Id: tel-00349762

<https://theses.hal.science/tel-00349762v1>

Submitted on 4 Jan 2009

HAL is a multi-disciplinary open access archive for the deposit and dissemination of scientific research documents, whether they are published or not. The documents may come from teaching and research institutions in France or abroad, or from public or private research centers.

L'archive ouverte pluridisciplinaire **HAL**, est destinée au dépôt et à la diffusion de documents scientifiques de niveau recherche, publiés ou non, émanant des établissements d'enseignement et de recherche français ou étrangers, des laboratoires publics ou privés.

UNIVERSITA' DEL SALENTO

**Dipartimento di Ingegneria dell'Innovazione
CREA – Centro Ricerche Energie ed Ambiente**

**Ph.D. Thesis
in “Sistemi Energetici ed Ambiente”
XIX Ciclo**

**ANALYSIS AND OPTIMIZATION OF DENSE GAS
FLOWS: APPLICATION TO ORGANIC RANKINE
CYCLES TURBINES**

Coordinatore del Ph.D.

Ch.mo Prof. Ing. Domenico Laforgia

Tutor

Ch.ma Prof.ssa Ing. Paola Cinnella

Studente

Ing. Pietro Marco Congedo

Anno Accademico 2006/2007

A tutti coloro che credono in me. Io continuerò sempre a credere in loro.

ANALYSIS AND OPTIMIZATION OF DENSE GAS FLOWS: APPLICATION TO ORGANIC RANKINE CYCLES TURBINES

by

Pietro Marco Congedo

(ABSTRACT)

This thesis presents an accurate study about the fluid-dynamics of dense gases and their potential application as working fluids in Organic Rankine Cycles (ORCs). The ORCs are similar to a steam Rankine Cycle where an organic fluid is used instead of steam, which ensures better efficiency for low-temperature sources. Specific interest is developed into a particular class of dense gases, the Bethe-Zel'dovich-Thompson (BZT) fluids, which exhibit negative values of the Fundamental Derivative of Gasdynamics Γ in the vapor phase, for a range of temperatures and pressures of the order of magnitude of those of the liquid/vapor critical point, just above the upper coexistence curve. Transonic and supersonic flows in a region of negative Γ are characterized by nonclassical gasdynamic behaviors, such as the disintegration of compression shocks. Owing to this effect, the use of BZT gases as working fluids in ORCs is particularly attractive, since it may reduce losses due to wave drag and shock/boundary layer interactions. This advantage can be further improved by a proper design of the turbine blade.

The present work is devoted to improve the understanding of the peculiar fluid-dynamic behavior of dense gases with respect perfect ones and to the research of suitable aerodynamic shapes. To this purpose, a dense-gas Navier-Stokes (NS) numerical solver is coupled with a multi-objective genetic algorithm. The Navier-Stokes solver employs equations of state of high accuracy within the thermodynamic region of interest and suitable thermophysical models for the fluid viscosity and thermal conductivity. Different computations are performed for transonic flows over isolated airfoils and through turbine cascades to evaluate the influence of the upstream kinematic and thermodynamic conditions on the flow patterns and the system efficiency, and possible advantages deriving from the use of a non-conventional working fluid are pointed out. Then, high performance airfoils and turbine blade shapes for transonic flows of BZT fluids are constructed using the CFD solver coupled with a multi-objective genetic algorithm. Shape optimization allows to strongly increase flow critical Mach Number, delaying the appearance of shock waves, while ensuring high lift (for an airfoil) and efficiency.

A careful analysis of the convergence behavior of Genetic Algorithms has also been undertaken by means of statistical tools. Genetic Algorithm exhibit a marked sensitivity to the shape of the response surface and to its numerical representation. Some strategies are proposed to systematically evaluate GAs convergence capabilities for a given problem and to enhance their convergence properties for dense gas optimization problems.

Acknowledgments

I am greatly indebted to Dr Paola Cinnella and Dr Domenico Laforgia for their guidance and financial support over the last three years. I have to thank Dr Christophe Corre for his strong support during my research period at the Ensam in Paris, and for his collaboration in the period after.

I would like to thank my family for always supporting me through good and difficult times in the past years.

A last thought is directed to all my best friends, Carlo, “Il Romanista”, Paola, “Mia Moglie”, Maria, “L’amica di Famiglia”, Saverio, “Il vecchio Sav”, Luisa, “Lou”, Marcos, “Le surrealiste”, Marcio, “Valderrama”, Sarvjit, “Crazy English”, James, “Invisible Man”, Maurizio, “L’oriundo”, Stefano, “A noi”. It has been a pleasure, nothing would be the same without you.

Publications

Journal Papers

- [1] P. Cinnella, P.M. Congedo, 2005, "Numerical solver for dense gas flows". *AIAA Journal*, Vol.43, No.11, pp.2458-2461
- [2] P. Cinnella, P.M. Congedo, 2005, "Aerodynamic performance of transonic BZT flows past an airfoil", *AIAA Journal*, Vol. 43, No.2, pp.370-378.
- [3] P.M. Congedo, C. Corre, P. Cinnella, 2005, "Airfoil shape optimization for transonic flows of Bethe-Zel'dovich-Thompson fluids". Accepted for publication in *AIAA Journal*.
- [4] P.Cinnella, P.M.Congedo, 2005, "Inviscid and viscous behavior of dense gas flows past an airfoil", *J. Fluid Mech.* 580(2007), 179-217
- [5] P.Cinnella, P.M. Congedo, 2006, "Optimal airfoil shapes for viscous dense gas flows", accepted for publication in *Computer and Fluids*

International Conferences

- [1] P. Cinnella, P.M. Congedo, 2004, "A numerical solver for dense gas flows", *AIAA Paper 2004-2137*. 34h *AIAA Fluid Dynamics Conference and Exhibit*, Portland, Oregon, 28 june-1^{er} july 2004.
- [2] P. Cinnella, P.M. Congedo, D. Laforgia, 2004, "Transonic BZT flows through turbine cascades", *Proceedings of ICCFD3*, 3rd *International Conference on Computational Fluid Dynamics*,- Toronto, Canada, 12-16 july 2004. In press by Springer.
- [3] P.Cinnella, P.M. Congedo, D. Laforgia, 2004, « Investigation of BZT transonic flows past an airfoil using a 5th power virial equation of state". *Proceedings of ECCOMAS*

2004 (on CD-ROM), *European Conference on Computational Mechanics and Applied Sciences*, Jyväskylä, Finland, 24–28 July 2004. ISBN: 951-39-1868-8.

[4] P. Cinnella, P.M. Congedo, 2005, “Optimal airfoil shapes for viscous dense gas flows”, Paper 2006-3881, presented to the 36th AIAA Fluid Dynamic Conference, San Francisco, June 2006

[5] P. Cinnella, P.M. Congedo, 2006, “GA-Hardness of dense-gas flow optimization problems”, Paper 522-151. *Proceedings of 15th IASTED International Conference on Applied Simulation and Modelling*, Rhodes, Greece, June 2006. ISBN: 0-88986-561-2, pp. 489-494

[6] P.M. Congedo, P. Cinnella, , C. Corre, 2006, “Shape optimization for dense gas flows through turbine cascades”, submitted to the 4th International Conference on Computational Fluid Dynamics (ICCFD 4), Ghent, Belgium, July 2006

[7], P. Cinnella, P.M. Congedo , 2007, “GA-Hardness of Aerodynamic Optimization Problems: Analysis and Proposed Cures”, accepted to the 37th AIAA Fluid Dynamic Conference, Miami, June 2007

National Conferences

[1] P. Cinnella, P.M. Congedo, 2004, “Analysis and Optimization of Viscous Dense Gas Flow”, 18h AIMETA Congress of Theoretical And Applied Mechanics, September 2007.

Reports

Master Thesis, “Optimisation de forme pour des écoulements de gaz denses” (in french), ENSAM, Paris, 2005.

Seminars

[1] *“Introduction to dense gas flows: exploitation of non-classical properties for energy applications.”*, invited seminar, National Institute of Aerospace (NIA), Hampton, Virginia, August 2006

[2] *“Dense gas flows: exploitation of non-classical properties.”*, invited seminar, Cha-Cha Days, College of Charleston, South Carolina, October 2006

List of Symbols

Alphanumeric Symbols

a	: Sound speed
A_2, B_2, C_2	: Coefficient for MAH equations
A_3, B_3, C_3	: Coefficient for MAH equations
A_4, B_5	: Coefficient for MAH equations
c_v	: Specific heat at constant volume
c_p	: Specific heat at constant pressure
dS	: Infinitesimal surface
e	: Internal energy
E	: Total internal energy
E_j	: distance of the individual from the individual of the training set
Ec	: Eckert number
f	: Inviscid flux function
f_v	: Viscous flux function
Fc	: Coefficient for the viscosity computation
h_j	: approximation function
H	: Total enthalpy
\bar{I}	: Unit tensor
M	: Mach number
M_∞	: Freestream Mach number
M_w	: Molecular weight
\vec{n}	: Outer normal to $d\Omega$
k	: Thermal conductivity
p	: Pressure
p_c	: Crossover probability
p_m	: Mutation probability
Pr	: Prandtl number
\vec{q}	: Heat flux vector
r	: attenuation coefficient

R	: Gas universal constant
s	: Entropy
t	: Time
T	: Absolute temperature
v	: Specific volume
V_c	: Critical Volume in cm^3/mol
\vec{v}	: Velocity vector
x	: input design variable vector
w	: Conservative variable vector

Greek Symbols

α_1	: Coefficient for thermal conductivity
α_{vdw}	: Coefficient for VDW equation
β	: Coefficient for thermal conductivity
β_{vdw}	: Coefficient for VDW equation
δ	: Dipole moment
δr	: Dimensionless dipole moment
μ	: Viscosity
ω	: Acentric factor
ρ	: Density
τ	: Viscous stress
Ω	: Volume
Ω_V	: Viscosity collision integral
σ	: Sharing parameter
Ψ	: Coefficient for thermal conductivity
Ξ	: Coefficient for thermal conductivity
Γ	: Fundamental derivative of gasdynamics
Λ	: Second non linearity parameter
Γ_∞	: Freestream fundamental derivative of gasdynamics
Λ_∞	: Freestream second non linearity parameter

Abbreviations

ANN	: Artificial Neural Network
BFGS	: Broyden-Fletcher-Goldfar-Shanno Method
BL	: Baldwin-Lomax turbulence model
BZT	: Bethe-Zel'dovich Thompson fluids
CFL	: Courant-Friedrich-Lewy
CPU	: Computational Processor Unit
DOE	: Design of Experiment
FDC	: Fitness Distance Correlation
HLL	: Hartex, Lax, Van Leer
HP	: High pressure transonic BZT regime
LP	: Low pressure transonic BZT regime
MAH	: Martin-Hou equation of state
MOGA	: Multi-Objective Genetic Algorithm
MUSCL	: Monotone Upstream-centered Schemes for Conservation Laws
NS	: Navier-Stokes
NSGA	: Non-Dominated Sorting Genetic Algorithm
ORC	: Organic Rankine Cycles
PFG	: Perfect Gas equation of state
PP10	: Heavy fluorocarbon pf-perhydrouorene
RANS	: Reynolds-averaged Navier-Stokes
SGS	: Structured Grid Solver
UGS	: Unstructured Grid Solver
VDW	: van der Waals equation of state

Contents

Acknowledgments	4
Publications.....	5
Journal Papers	5
International Conferences	5
National Conferences.....	6
Reports.....	6
Seminars.....	7
List of Symbols.....	8
Alphanumeric Symbols.....	8
Greek Symbols.....	9
Abbreviations.....	10
Contents	11
List of Figures.....	13
1. Introduction.....	17
1.1. State of Art.....	20
1.1.1. Fluid-Dynamic of Dense Gas Flow	21
1.1.2. Shape optimization for dense gas flows	27
1.1.3. GA-Hardness of Dense gas Flow optimization problems	29
1.2. Overview of the following chapters.....	31
2. Governing equations and flow solvers.....	32
2.1. The Euler and Navier-Stokes equations for single-phase non reacting flows	32
2.1.1. Rans Equations	32
2.2. Thermodynamic models	34
2.2.1. Equations of state.....	34
2.2.2. Laws for viscosity and thermal conductivity	37
2.3. Flow solvers.....	38
2.3.1. Structured solver	38
2.3.2. Unstructured solver.....	39
2.3.3. How a more complex equation of state affects a NS code	40

3.	Optimization tool	41
3.1.	Genetic Algorithms	41
3.2.	Gradient Based Methods	42
3.3.	Metamodels	43
3.3.1.	Artificial Neural Network	43
3.3.2.	Richardson Extrapolation	44
4.	Results	47
4.1.	Dense gas flow past an airfoil	47
4.1.1.	Choice of the operating conditions	47
4.1.2.	Inviscid Flow behavior	49
4.1.3.	Viscous flow behavior	59
4.2.	Transonic dense gas flow through turbine cascade	65
4.3.	Shape Optimization of an isolated Airfoil	69
4.3.1.	Inviscid Case	69
4.3.1.1.	Drag Minimization for a symmetric airfoil	69
4.3.1.2.	Performance Optimization for a Lifting Airfoil	80
4.3.2.	Viscous Case	90
4.3.2.1.	Drag Minimization for a Symmetric Airfoil	90
4.3.2.2.	Performance optimization for a Lifting Airfoil	96
4.4.	Efficiency Maximization for a turbine cascade	101
4.5.	GA-Hardness of Drag minimization problem	106
4.5.1.	Drag Minimization for a Symmetric Airfoil	106
4.5.2.	Cures to GA-Hardness	112
5.	Conclusions	116
	Suggestion for futures study	119
6.	Bibliography	120

List of Figures

Figure 1: Amagat diagrams for a van der Waals BZT gas with $\gamma=1.0125$ (a) and for the heavy fluorocarbon PP10 modeled through the Martin-Hou equation of state (b). The shaded region represents the inversion zone.....	36
Figure 2: Location of the operation points in the $p - v$ diagram.	48
Figure 3: Fundamental derivative versus pressure along selected isentropes.	49
Figure 4: Aerodynamic coefficients versus free-stream fundamental derivative for flow at	54
Figure 5: Pressure coefficient contours and $\Gamma = 0$ contours for operating conditions.....	54
Figure 6: Wall distributions of the Mach number, pressure coefficient, fundamental derivative	55
Figure 7: Pressure coefficient contours and $\Gamma = 0$ contours for operating conditions.....	56
Figure 8: Wall distributions of the Mach number, pressure coefficient, fundamental derivative	57
Figure 9: Pressure coefficient contours and $\Gamma = 0$ contours for operating conditions.....	58
Figure 10: Wall distributions of the Mach number, pressure coefficient, fundamental derivative	59
Figure 11: Turbulent flow over the NACA0012 airfoil, $M_\infty = 0.85$, $\alpha = 1^\circ$, $Re = 9 \times 10^6$. Pressure coefficient contours and streamlines (left) and wall pressure coefficient (right) for a perfect gas flow (a,b) and for PP10 at operating conditions $p_\infty/p_c = 1.01$, $\rho_\infty/\rho_c = 0.676$ (c,d), $p_\infty/p_c = 1.08$, $\rho_\infty/\rho_c = 0.850$ (e,f), $p_\infty/p_c = 1.17$, $\rho_\infty/\rho_c = 1.11$ (g,h).....	62
Figure 12: Aerodynamic coefficients versus free-stream fundamental derivative for turbulent.....	63
Figure 13: Skin friction for a perfect gas flow and dense gas flows at different operating.	64
Figure 14: Isobares for a perfect gas (a), steam (b), and PP10 (c). VKI LS-59 cascade.	66
Figure 15: Cascade efficiency versus inlet Fundamental Derivative. Left: SC11 cascade;	67
Figure 16: Mach distributions at the wall. VKI LS-59 cascade.....	67
Figure 17: Pressure distributions at the wall. VKI LS-59 cascade.	68
Figure 18: Γ distributions at the wall. VKI LS-59 cascade.	68

Figure 19: Evolution of the maximal and mean value of the drag coefficient for the computed population as function of the number of generations. Mono-objective (single operation point) optimization runs for different values of the freestream Mach number....	73
Figure 20: Geometry of optimized airfoils, sonic arc, Rusak low-drag airfoil and NACA0012 airfoil.	74
Figure 21: Pressure drag versus free-stream Mach number for different airfoil shapes. Results obtained using UGS (a) and SGS (b).	75
Figure 22: Wall pressure (a) and Mach number (b) distributions for optimized airfoils, sonic arc, Rusak airfoil and NACA0012 airfoil at $M=0.95$. SGS results.	76
Figure 23: (a) optimal geometries for the drag minimization problem solved in the case of a PFG flow and a DG flow with VDW or MAH EOS. (b) Associated pressure drag as a function of the freestream Mach number.	77
Figure 24: Pressure contours around the baseline NACA0012 airfoil and optimal airfoils for perfect and dense gas flows with freestream conditions leading to an equivalent amount of wave drag for the baseline airfoil.	78
Figure 25: Mach number contours and streamlines for turbulent flows past four airfoils (right); left: close-up of the streamlines at the trailing edge (grid aspect ratio not preserved). A) OAB; B) OA095; C) NACA0012; D) Rusak-Wang. $M_\infty = 0.96$, $Re \cong 10^7$	79
Figure 26: Viscous performance of minimal-drag airfoils stemming from inviscid optimization.	80
Figure 27: Lifting airfoil 2-point performance optimization. Overview of the computed solutions during the genetic evolution process.	84
Figure 28: Lifting airfoil 2-point performance optimization. Typical optimal shape.	84
Figure 29: Lifting airfoil 2-point performance optimization. Wall distributions (a) (b) at OP#1 for the NACA0012 airfoil and an optimal airfoil for DG flow.	85
Figure 30: Lifting airfoil 2-point performance optimization. Wall distributions (a) (b) at OP#2 for the NACA0012 airfoil and an optimal airfoil for DG flow.	86
Figure 31: Evolution of aerodynamic performances (a) (b) at $M_\infty=0.85$ and $\alpha =1^\circ$ for a dense gas flow around the NACA0012 airfoil and a DG-optimized airfoil at different free-stream thermodynamic conditions.	87

Figure 32: Lifting airfoil 2-point performance optimization. Wall distributions (a) of the pressure and skin friction (b) coefficients for viscous flow at OP#1 past the NACA0012 airfoil and an optimal airfoil for DG flow.	88
Figure 33: Lifting airfoil 2-point performance optimization. Wall distributions (a) of the pressure and skin friction (b) coefficients for viscous flow at OP#2 past the NACA0012 airfoil and an optimal airfoil for DG flow.	89
Figure 34: Evolution of the maximal and mean value of the drag coefficient for the computed population as a function of the number of generations.	93
Figure 35: Geometry of minimal drag airfoils obtained by including or neglecting, respectively, viscous effects, and NACA0012 airfoil.	93
Figure 36: Mach number contours and streamlines for turbulent flows past four airfoils (right); left: close-up of the streamlines at the trailing edge (grid aspect ratio not preserved). A) NACA0012 perfect gas; B) NACA0012 dense gas; C) Shape optimized for viscous dense-gas flow; D) Shape optimized for inviscid dense-gas flow; $M_\infty=0.96$, $Re\approx 10^7$	94
Figure 37: Wall distribution of the pressure coefficient for three cases plotted in Figure 36	95
Figure 38: Drag coefficient as a function of the freestream Mach number for dense-gas viscous flow at operating conditions $p_\infty/p_c=0.985$, $\rho_\infty/\rho_c=0.622$. The figure compares the performance of an airfoil shape optimized for viscous dense gas flow, for an airfoil shape optimized for inviscid dense gas flow, and for the NACA0012 airfoil.	95
Figure 39: Lifting airfoil 2-point performance optimization. Overview of the computed solutions during the genetic evolution process.	99
Figure 40: Optimal airfoil shapes and baseline shape for the lifting flow problem.	99
Figure 41: Mach number contours and flow streamlines for Airfoil 4 (A), Airfoil* (B) and the NACA0012 airfoil (C). $M_\infty=0.85$, $\alpha=1^\circ$, $Re=9\times 10^6$. Left: condition OP1; right: condition OP2.	100
Figure 42: Wall distributions of the pressure coefficient C_p for Airfoil 4, Airfoil*, and NACA0012. $M_\infty=0.85$, $\alpha=1^\circ$, $Re=9\times 10^6$. A) Condition OP1; B) condition OP2.	101
Figure 43: optimal shape for perfect gas flow	104
Figure 44: optimal shape for dense gas flow	104
Figure 45: PFG flow, isoMach lines: a) baseline; b) optimized. c,d) Wall distributions. .	105

Figure 46: DG flow, isoMach lines: a) baseline; b) optimized. c,d) Wall distributions....	106
Figure 47: (a) Optimal geometries for the drag minimization problem for an inviscid perfect gas flow with $M_\infty=0.83$ obtained using different initial populations; (b) corresponding wall distributions of the Mach number.	111
Figure 48: Frequency histogram for DOE data	111
Figure 49: Optimal geometries resulting from four optimization runs with different starting populations.....	112
Figure 50: BZT van der Waals gas flow over a symmetric nonlifting airfoil. Optimal geometries obtained using a fine-grid estimate or a multigrid (Richardson extrapolation) estimate of the fitness function	115
Figure 51: BZT van der Waals gas flow over a symmetric nonlifting airfoil. (a) Pressure coefficient isolines past optimal individuals ($\Delta C_p=0.1$); (b) wall Mach number; (c) Wall pressure coefficient	115

1. Introduction

Organic Rankine cycles (ORCs) is a closed power cycle composed of four basic components. Heat is supplied to a heater where the compressed liquid is converted to a superheated vapor at constant pressure. The vapor is then expanded through a turbine stage to produce a work output. For an impulse turbine stage, the flow is expanded through a stator stage or through nozzles. Vapor leaving the turbine then enters the condenser where heat is removed until the vapor is condensed into the liquid state. Saturated liquid is then delivered to a pump, which raises the pressure of the liquid and is then delivered back to the heater where the cycle then repeats. Then, ORCs are similar to the large steam Rankine cycle but the main difference is that ORCs utilize heavy working fluids, i.e., organic compounds, which result in superior efficiency over steam Rankine cycle engines for heat source temperatures below around 900 K. ORCs typically require only a single-stage expander which consists of a single rotating component for the entire system in the turbine stage, making them much simpler than multi-stage expanders typical of the steam Rankine cycle. Typically, the working fluids are of retrograde type. Therefore it is not necessary a reheat which greatly simplifies the cycle structure. Moreover the risk of blade erosion is avoided due to the absence of moisture in the vapor nozzle. ORCs are an appealing option for remote, low power applications because of its mechanical simplicity. Such simplicity also gives ORCs obvious advantages in manufacturing cost and reliability over other types of small engines that are more mechanically complex, e.g., typical two or four-stroke engine generators, multistage gas turbine engines, and reciprocating Stirling engines. Indeed, the main characteristics of an ORCs are a very high turbine efficiency, a long life, and minimum maintenance requirements.

For the past several decades, thousands of ORCs have been developed and used for remote terrestrial applications with power outputs ranging from 1 to 1000 kW. A few examples of remote applications that have used efficient, reliable, unattended ORCs power sources include communication stations, data gathering buoys, satellite communication power supplies, as well as irrigation pumps, air conditioners, and turbogenerators. The most recent developments in ORCs technology have focused on using the following three renewable energies as heat sources: solar, geothermal, waste heat.

To increase the ORCs efficiency, a possible approach is to use dense gases as working fluids. Dense gases are defined as single-phase vapors operating at temperatures and pressures of the order of magnitude of those of their thermodynamic critical point. At these conditions, real gas effects play a crucial role in the gasdynamic behavior of the fluid. The dynamic behavior of dense gases is governed by the fundamental derivative of gasdynamics:

$$\Gamma = 1 + \frac{\rho}{a} \left(\frac{\partial a}{\partial \rho} \right)_s, \quad (\text{Eq. 1})$$

with ρ the fluid density, a the sound speed, and s the entropy. It can be also rewritten as:

$$\Gamma = \frac{v^3}{2a^2} \left(\frac{\partial^2 p}{\partial v^2} \right) \quad (\text{Eq. 2})$$

where $v=1/\rho$ is the fluid specific volume and p the pressure. Γ represents a measure of the rate of change of the sound speed, $a = \left(-v^2 (\partial p / \partial v)_s \right)^{1/2}$. If $\Gamma < 1$, from (Eq. 1) the following relations is derived:

$$\Gamma < 1 \Rightarrow \left(\frac{\partial a}{\partial \rho} \right)_s < 0. \quad (\text{Eq. 3})$$

Then the flow exhibits an uncommon sound speed variation in isentropic perturbations: a grows in isentropic expansions and drops in isentropic compressions, contrarily to what happens in “common” fluids. For heavy gases, composed by sufficiently complex molecules and characterized by high c_v/R ratios (with c_v the constant volume specific heat and R the gas constant), Γ is smaller than 1, or even than 0, for extended ranges of densities and pressures, and recovers its “perfect gas” value in the low density limit. The sign of Γ is univocally determined by the sign of the second derivative $\left(\frac{\partial^2 p}{\partial v^2} \right)_s$, i.e. the

concavity of the isentrope-lines in the $p-v$ plane. It is possible to show [8] that the entropy change across a weak shock can be written as:

$$\Delta s = -\frac{a^2 \Gamma (\Delta v)^3}{v^3 6T} + O((\Delta v)^4) \quad (\text{Eq. 4})$$

where Δ represents a change in a given fluid property through the shock. As a result, in order to satisfy the second law of thermodynamics, a negative change in the specific volume, i.e. a compression, is required if $\Gamma > 0$, whereas a positive change, i.e. an expansion, is the only physically admissible solution when $\Gamma < 0$. Then, for these fluids, known as the Bethe-Zel'dovich-Thompson fluids [4], that exhibit a value of $\Gamma < 0$ in a range of thermodynamic conditions above the liquid/vapor coexistence curve, the well-known compression shocks of the perfect gas theory violate the entropy inequality and are therefore inadmissible [4][8][15]. The thermodynamic region characterized by negative values of Γ is usually called the inversion zone, and the $\Gamma = 0$ contour is said the transition line. BZT properties are generally encountered in fluids possessing large heat capacities and formed by complex, heavy molecules, such as some commercially available heat transfer fluids. An important property of BZT fluids is that the shock strength is reduced up to one order of magnitude from that predicted by equation (Eq. 4) for thermodynamic conditions where $\Gamma \approx 0$. Cramer and Kluwick [8] showed in fact that $\Gamma = O(\Delta v)$ for small volume changes in the vicinity of the transition line. Thus, shock waves having jump conditions in the thermodynamic region near the $\Gamma=0$ contour are expected to be much weaker than normal.

Then, summarizing the different thermodynamic behaviors related to the dense gas flows, the following considerations can be underlined:

- 1) for such conditions of pressure and density that $\Gamma < 1$, and $\Gamma = O(\Delta v)$, compression shocks are weaker than normal, and the sound speed and the density are related by the (Eq. 3), that is in contrast with the PFG equation.
- 2) for such conditions of pressure and density that $\Gamma < 0$, the compression shocks are also completely forbidden (BZT fluids).

The unusual properties of dense gases could find application in technology. One of the more obvious applications is the use of dense gases in turbomachinery and in the ORCs. Because of the use of a few, highly loaded, expansion stages, ORC turbines typically work in the transonic/low supersonic regime and their major loss mechanism is related to the generation of shock waves and their interactions with the blade boundary layers. Therefore, on the one hand a detailed study of turbomachinery flows of dense gases is necessary to

correctly predict the system behavior; on the other hand, non-classical dense gas phenomena could be exploited to improve efficiency: namely, shock formation and subsequent losses could be ideally avoided, if the turbine expansion could happen entirely within or in the immediate neighborhood of the inversion zone. In fact properly operating the turbine in the very neighborhood of the curve, the flow field evolves almost entirely within the inversion zone, and is shock-free: as a result, except for viscous drag, the flow remains isentropic through the entire cascade. Unfortunately, the inversion zone has a quite limited extent: therefore, a reduction in the temperature jump between the heater and condenser stages is generally required in order to completely operate the turbine within the inversion zone. Now, it is well-known from thermodynamic theory that a too small temperature jump implies low thermal cycle efficiency. Moreover, a small temperature (i.e. enthalpy) jump also means low cycle power output. This important drawback has been the stumbling block to the development of real-world BZT Organic Rankine Cycles. In practice, BZT gas effects can find application in ORC turbomachinery only finding a reasonable trade-off between the above opposite requirements.

Then, two ways are possible to reduce the losses in the ORC: the use of particular fluids for which the compression shock are forbidden or anyway very reduced; the optimization of the geometry in order to maximize the efficiency.

In the present work, these two aspects are analyzed in deep. Dense gas flows over an isolated airfoil and over a turbine blade are analyzed in order to understand the effects of freestream conditions of pressure and temperature on the aerodynamic performances, and the role played by BZT effects. The second aspect is related to shape optimizations, performed to maximize some aerodynamic properties on the optimal geometries. The state of art for the dense gases numerical simulation will be presented in the next paragraph, followed by the brief description of the Chapters.

1.1. State of Art

In this paragraph the state of art on the numerical simulation of dense gas flow is described, including the contribution made by the author, and the brief description of all the results achieved. The most important among them will be presented widely in the Chapter 4. This section is divided in three paragraphs. The first two concern the fluid-

dynamics of dense gas flow and the shape optimization for dense gas flow. In the following, the state of art concerning the study of GA-Hardness is presented.

1.1.1. Fluid-Dynamic of Dense Gas Flow

The possibility of having expansion shock for particular equation of state was first discussed by Bethe [1] and Zel'dovich [2] in two pioneer papers in 1942 and in 1946. But, it was Thompson [4], who first link the monotonic behavior of the Fundamental Derivative of Gasdynamics to the possibility to have expansion shocks. In this paper he discussed about the potential property of a fluid which could exhibit $\Gamma < 0$, even if there was no evidence that such a fluid could exist. In [5] it was seen that particular complex fluids can present BZT properties based on published thermodynamic data. In [6] Thompson analyzed the formation and evolution of a rarefaction shock wave. Such shock satisfy stability conditions and have a positive small entropy jump.

Cramer and Kluwick in [8] studied the one dimensional small amplitude waves in which the local value of the fundamental derivative changes sign. They showed in fact that $\Gamma = O(\Delta v)$ for small volume changes in the vicinity of the transition line. Thus, shock waves having jump conditions in the thermodynamic region near the $\Gamma=0$ contour are expected to be much weaker than normal. Indeed, they introduced the second nonlinearity parameter $\Lambda = \rho \left(\frac{\partial \Gamma}{\partial \rho} \right)_s$. In [10] and [11], Cramer & Sen considered a gas described by the

Van der Waals equation, in which the specific heat is taken to be large enough to generate an embedded region of negative non linearity close to the thermodynamic critical point. In [10] they showed how the shock formation process may differ from that predicted by the perfect gas theory for an isolate pulse and periodic wave trains. In [11] they presented the exact closed-form solution for finite amplitude sonic shocks. The solutions are provided for both single and double sonic shocks. Cramer [14] used the Martin-Hou equation (introduced by Martin and Hou in 1955 in [3]) to compute the fundamental derivative of Gasdynamics for seven commercially available fluorocarbons. Each fluid was found to have a region of negative nonlinearity large enough to include the critical isotherm. The inversion region foreseen by the Martin-Hou equation is reduced with respect to that one computed with the Van der Waals equation. Cramer in [15] showed that inadmissible discontinuities give rise to shock splitting over a finite range of pressure and temperatures

where the fundamental derivative is negative. In [16] Cramer & Best showed that the Mach number may increase, rather than decrease, with density or pressure if the specific heats of the fluid are sufficiently large. Conditions are also reported under which isentropic expansions through converging–diverging nozzles are not possible, regardless of the imposed exit pressure. In such cases, the nozzle must be replaced with one having multiple throats. Applications to external transonic flows are also briefly considered for the first time. Investigations of the viscous structure of one-dimensional non classical shocks have been presented for the first time in [17]. New results included the first computation of the structure of finite-amplitude expansion shocks and examples of shock waves in which the thickness increases, rather than decreases, with strength. Morren in his thesis [18] presented the transonic flow of dense gases for two dimensional, steady-state flow over a NACA0012 airfoil using the Euler equations and the van der Waals equation of state. The results indicated that dense gases with undisturbed thermodynamic states in the negative Γ region show a significant reduction in the extent of the transonic regime as compared to that predicted by the perfect gas theory. Cramer & Tarkenton in [19] examined the steady transonic flow of BZT fluids over two-dimensional thin wings and turbine blades by solving an extended transonic small disturbance equation derived for flows with $\Gamma \approx 0$, $M \approx 1$ (with M the Mach number) and also characterized by small values of the second nonlinearity parameter $\Lambda = \rho \left(\frac{\partial \Gamma}{\partial \rho} \right)_s$ ([8]). The free-stream state is taken to be in the

neighborhood of one of the zeros of Γ . They found a significant increase of the critical Mach number in flows of BZT fluids over profiles. Numerical solutions of the small disturbance equation completed by the Martin-Hou (MAH) gas model revealed substantial reductions in the strength of compression shocks. Emanuel [20] showed that the Martin-Hou equation of state can be considered the reference thermodynamic model for dense gases. Cramer [21] presented a numerical investigation of laminar flows of dense gases over a flat plate. The results indicate a failure of classical scaling laws for compressible boundary layers (Chapman-Rubesin scaling), and a reduction of the boundary layer friction heating in complex gases with large heat capacities. Numerical solutions of the Euler equations for isenthalpic flows through turbine cascades by using the Martin-Hou gas model had been provided by Monaco [22] for incoming flow conditions characterized by small values of Γ . It was found that the natural dynamics of BZT fluids can result in

significant reduction in the adverse pressure gradients associated with the collision of compression waves with neighboring turbine blades. A numerical example of an entirely isentropic supersonic cascade is presented. Transonic flows of a dense gas around the leading edge of a thin airfoil with a parabolic nose had been studied by Rusak [23]. Asymptotic expansion of the velocity potential function were constructed in terms of the airfoil thickness ratio in an outer region around the airfoil and in an inner region near the nose. In [24] Brown & Argrow simulated shock tube flows with compressive wedges and circular areas. Non-classical phenomena, like expansion shocks and composite waves demonstrate significant differences from perfect gas flow fields over similar geometries. Wang & Rusak [26] provided numerical studies of transonic BZT flows past a NACA0012 airfoil at zero angle of attack (non lifting case) using the numerical code of Morren [18], and provided a classification of possible flow patterns for oncoming flow conditions such that $\Gamma_\infty, \Lambda_\infty \approx 0$, guided by the asymptotic theory developed in [23]. Cramer & Park in [27] considered the reflection of oblique compression waves from a two-dimensional, steady, laminar boundary layer on a flat, adiabatic plate at free-stream pressure such that dense gas effects are non-negligible. Numerical results showed a suppression of shock induced separation in supersonic Bethe-Zel'dovich-Thompson flows past sharp compression corners. Results concerning flows through realistic impulse turbine cascades had been presented by Brown [28], who solved the Euler equations closed by the Martin-Hou gas model. Operating under the proper thermodynamic conditions, a BZT working fluid can potentially weaken or eliminate shock waves. This would reduce losses due to both the wave drag from shocks as well as losses from boundary-layer separation due to shock reflections on the turbine blades. Results showed significant improvements in turbine efficiencies for BZT working fluids over conventional ORC working fluids. Kluwick in [31] discussed a new form of marginal boundary layer separation in laminar flows of dense gases using asymptotic methods: the non monotonous Mach-number variation with pressure leads to non conventional distribution of the shear stress and displacement body in boundary layers subjected to adverse pressure gradients, which contributes to delay separation. In [32] and [33] Ferguson & Al., in preparation for a shock tube experiment, presented a theory to demonstrate a single-phase vapor rarefaction shock wave in the incident flow of the shock tube. The analysis predicts just a small region of initial states that may be used to unequivocally demonstrate the existence of a single-phase

vapor rarefaction shock wave. In [34] Colonna & Silva presents the procedure for obtaining nonconventional thermodynamic properties needed by up to date computer flow solvers. Complex equation of state for pure fluids and mixtures are treated. Peng-Robinson thermodynamic model allows reproducing with good accuracy the experimental data. Kluwick [36] investigated shock/boundary layer interaction in dense gases via the triple deck theory. Their results show that it is possible to reduce the size of the separation bubble or even to avoid the occurrence of flow separation by choosing an optimal operation thermodynamic state. In [37] Colonna & Rebay presents the numerical methods and the models implemented in a computer code for simulating inviscid dense gas flows on unstructured grids. In [38] Guardone & Al. studied the accuracy of thermodynamic models in the computation of nonclassical gasdynamic phenomena. The Soave-Redlich-Kwong and the Peng-Robinson models are compared to the Martin-Hou equation. The three models are found to exhibit a comparable accuracy for an extended range of reduced volume, and for predicting the formation of supersonic nonclassical rarefaction wave. In [39] Cinnella & Congedo presented a numerical solver for inviscid flows governed by arbitrary equations of state. In particular, the stress is put on the choice of a suitable space discretisation scheme for dense gas problems. Two different schemes are considered: the first one, uses a third-order centred approximation with addition of scalar artificial viscosity; the second one, is a second-order accurate upwind scheme based on Roe's flux difference splitting. Detailed cross-comparisons of the two schemes are provided for a variety of transonic flow problems past airfoils and turbine blades. In 2004, Cinnella & Congedo [40] have investigated the influence of BZT effects on the system performance of inviscid transonic lifting flows past a NACA0012 airfoil. Numerical simulations were performed by solving the Euler equations discretized by a third-order-accurate numerical scheme on very fine meshes. The gas response was modelled by the van der Waals equation of state for polytropic gases. In contrast with previous studies, the investigation was not restricted to flows with small free-stream Γ . On the contrary, the objective of the research was to explore the possibility of keeping part of the benefits deriving from BZT behavior while enlarging the operation range. At this end, a detailed parametric investigation of the airfoil aerodynamic performance was undertaken, with specific interest in configurations providing the best trade-off between high lift and low drag. The parametric study allowed to identify three flow regimes depending on the value of Γ_∞ . For

small values of Γ_∞ , in the subcritical regime, the lift-to-drag ratio tends to infinity (for inviscid flows) because the flow remains subsonic everywhere, thus avoiding the occurrence of wave drag. When Γ_∞ is in the range 2÷3 a significant growth in both lift and drag is observed: the increase in lift is produced by the formation of an expansion shock close to the leading edge, that strongly enhances the suction peak at the airfoil upper surface; the increase in drag is due to the occurrence of shocks on the airfoil surface. In this regime, the lift-to-drag ratio remains one order of magnitude greater than in the perfect gas case. Finally, when Γ_∞ reaches higher values, transonic BZT regime, the flow becomes qualitatively similar to that of a perfect gas with even poorer aerodynamic performances. In summary, results presented in Cinnella & Congedo [40] suggest that the choice of upstream conditions within or very close to the transition line is not only not mandatory in order to improve airfoil performance, as suggested in previous studies, but also not optimal. Specifically, optimal aerodynamic performance (i.e. the best trade-off between high lift and low drag) is obtained for, more precisely, $\Gamma \approx 3$. This is of great importance, in light of the design of BZT Organic Rankine Cycles, since it suggests the possibility of enlarging the operation range of the expansion stage without losing the benefits of dense gas effects. Results presented in Cinnella & Congedo [40] have been obtained using the van der Waals equation of state, also used in many former studies, as the simplest gas model accounting for BZT effects: it is computationally inexpensive, and allows capturing qualitative features of BZT fluid flows. On the other hand, this model is not very accurate for thermodynamic conditions close to saturation, i.e. the region of interest in the present study, and largely over-predicts the extent of the inversion zone [6]. Another limitation of the study reported in Cinnella & Congedo [40] is related to the fact that thermo-viscous effects are completely neglected, as also done in almost all previous studies. A numerical investigation of two-dimensional inviscid and viscous dense gas flows past an isolated airfoil is presented by Cinnella & Congedo [41]. For the inviscid case similar qualitative conclusions have been drawn as in [40] where the parametric study has been repeated using the more realistic Martin-Hou (MAH) equation of state (EOS). Beneficial effects deriving from the use of a dense working fluid are also observed when the airfoil viscous performance is considered. Namely, the nonclassical variation of the Mach number with density in conjunction with reduced friction heating contribute to reduce friction drag and to avoid boundary layer separation due to large adverse pressure gradients. In addition,

post-shock separations due to shock/boundary layer interaction are also greatly reduced, ensuring satisfactory lift and aerodynamic efficiency at flow conditions where the aerodynamic performance of perfect gas flows suffers from shock stall. The main results of [41] will be widely presented in Chapter 4. In 2005, Cinnella [44] presented an extension of classical Roe's scheme to real gas flows. A simplification to Roe's linearization procedure is proposed, which does not satisfy the U-property exactly, but significantly reduces complexity and computational costs. Guardone & Argrow [45] investigated the nonclassical gasdynamic behavior of different fluorinated substances using different thermodynamic models of increasing complexity. A strong dependence on the acentric factor of the substance is revealed, which makes the fluids made of nonpolar molecules with nearly spheroidal shape as the most favorable to exhibit nonclassical gasdynamic behavior. In [49] the van der Waals polytropic gas model is used to investigate the role of attractive and repulsive intermolecular forces and the influence of molecular complexity on the possible nonclassical gas dynamic behavior of vapors near the liquid-vapor saturation curve. Results of the exact solution to the problem of a finite pressure perturbation traveling in a still fluid are presented for the ideal gas, for the dense gas and for the nonclassical gas behavior. Colonna & Al. [50] presented the development of technical equations of state for any siloxanes, that present BZT properties and have some positive technological characteristics (because of their low toxicity, excellent thermal stability, limited flammability). Available measured properties are critically evaluated and selected for the optimization of the equation of state parameters. The improvement obtained with this equations are significant. In [51] Guardone presented a recently developed experimental technique to generate and visualize spherical compression waves in a BZT gas. Flow simulations were performed to evaluate the potential of using this experimental arrangement to investigate the formation and propagation of nonclassical waves. In [54] Colonna & Al. presented the evaluation of the influence of different equations of state (EoS) on the computed aerodynamic performance and the test case is a 2D nozzle blade of an existing ORC turbine operated with the siloxane MDM as working fluid. Cramer [56] presented Rayleigh flows of single-phase, nonreacting fluids when a BZT fluid is considered. Exact solutions for Van der Waals gases are provided and a complete theory of shocked and unshocked flows subjected to strict heating or strict cooling is developed.

The experiments related to BZT fluids have not been extensively funded by industries because of the uncertainty about a concrete exploitation of BZT fluids, and because of a difficulty to show clearly a concrete advantage with respect to other low power systems in a wide region of working conditions. The first attempt to show experimental evidence of existence of non classical rarefaction shock waves in the vapor phase was made by Borisov [7][12]. A steep rarefaction wave in Freon-13 was observed to propagate with no distortion and it was claimed to be a non classical rarefaction shock. Their results has been challenged by many authors [10][33][35][12] and their measurements are likely to be influenced by critical point and two-phase phenomena. In 2003, a non classical shock-tube facility [35] has been constructed and tested at the University of Colorado at Boulder, but many technological problems, including the imperfect burst of the shock-tube diaphragm and the thermal decomposition of the working fluid, prevented the observation of a rarefaction shock wave in fluid PP10 (Pf - perhydrofluorene, C13F22). In [52] the preliminary design of a Ludwieg tube experiment for the verification of the existence of nonclassical rarefaction shock waves in dense vapors is critically analyzed by means of real gas numerical simulations of the experimental setup.

1.1.2. Shape optimization for dense gas flows

For what concerns the airfoil geometry optimization with dense gas flows, the first study on this topic has been achieved by Rusak [25][29], who consider the construction of low-drag shapes for non-lifting inviscid flows of dense gases through the Transonic Small Disturbance Theory. In [23], similarity solutions of a nonlinear small-disturbance equation, describing a two-dimensional near-sonic potential flow of dense gases, are studied. The solutions are applied to the problem of a near-sonic small-disturbance flow of dense gases in the surrounding of two-dimensional, slender, semi-infinite bodies with x^n generators, where $2/7 < n < 1$ and x is the distance along the body axis. In the case when $n=2/7$, the body constitutes a surface over which the flow is sonic at every point and the pressure distribution is constant. The analysis indicates that such a shape is optimal for near-sonic flows of dense gases, in the sense it offers the minimal pressure drag. In [29], low-drag airfoils are constructed through a nonlinear small-disturbance theory. The modified airfoils are characterized by arcs along which the flow is sonic, connected to a sharp tail. These airfoils exhibit a higher critical Mach number, *i.e.* Mach number for which the flow is nowhere supersonic, with respect to non-optimized shapes. Consequently, they yield

zero wave-drag over a larger range of incoming flow velocities. Specifically, the analytical study presented in [29] derives the geometry of an airfoil with a 12% thickness-to-chord ratio that shows lower wave drag than the NACA0012 airfoil at zero incidence for specific freestream thermodynamic conditions ($\Gamma_\infty=0$). [29] has the merit of facing for the first time optimization problems for dense gas flows past airfoils, even though an optimization procedure in the proper sense is not undertaken. In practice, such an approach is incomplete, as it does not take into account the effect of the optimization on the airfoil lift. Moreover, the small disturbance approximation does not model accurately the important flow variations at the airfoil leading and trailing edges, which have a crucial influence on the airfoil performance, especially for high- Γ incoming flow conditions. In [42], Congedo& Corre& Cinnella present first results on optimal airfoil geometries for transonic dense gas flows by making use of evolutionary optimization strategies, by taking in account just Euler effects. Two optimization problems are considered: the first one, as in Rusak and Wang's work [29], aims at finding a minimal drag airfoil shape for a non-lifting flow in the BZT regime. This symmetric problem is relatively simple to treat since the flow symmetry reduces the computational expense, while a single objective function to minimize, namely the drag, implies lower optimization complexity. It is shown that, if the optimal airfoil shape derived in [29] does exhibit lower drag than a reference airfoil with the same thickness-to-chord ratio, viz. the NACA0012 airfoil, the approach presented allows to obtain even higher performances by combining an efficient Euler solver to a genetic algorithm. The second application deals with the optimization of a lifting airfoil. The following optimization strategy is adopted: find an airfoil shape that allows on the one hand allows to obtain high lift at BZT subcritical conditions, where the wave drag is in any way expected to be zero and, on the other hand, to minimize wave drag while maximizing lift for supercritical BZT flow conditions. These results will be widely presented in Chapter 4. Cinnella& Congedo presents in [46] dense-gas flow optimization problems considered in [42] by taking fully into account viscous effects. Optimal airfoil shapes for viscous transonic flows of dense gases have been generated by using a multi-objective genetic algorithm coupled with a dense gas flow solver. Computational costs related to the great number of evaluations of the objective function by means of the Navier-Stokes solver have been substantially reduced by using a properly calibrated artificial neural network to interpolate the response surface. When solved both for inviscid and viscous flow, the drag

minimization problem of a symmetric airfoil with fixed thickness-to-chord ratio yields indeed shock-free shapes for an extended range of the freestream Mach number; however, the optimal airfoils generated by neglecting viscous effects display a thick trailing edge that is bound to induce premature flow separation hence an increase in form drag when taking into account the viscous effects in the flow analysis. Moreover, they are also characterized by a thick leading edge, which produces a deep suction peak followed by an extended region characterized by strong adverse pressure gradient. As a consequence, at subcritical speeds these airfoils display a slightly higher drag coefficient than the baseline configuration. These difficulties are overcome by including viscous effects into the optimization process, which provides an airfoil shape whose performance is far superior to the baseline over the whole range of Mach numbers considered for the study. The multi-point performance optimization for a lifting airfoil in subcritical and supercritical flow conditions has allowed determining an airfoil shape that provides an overall improvement of the lift coefficient while preserving the high lift-to-drag ratio typical from BZT flows. This result will be widely presented in Chapter 4. Finally, in [47], Congedo & Cinnella & Corre present a study about optimal blade shapes for BZT ORC turbines, providing high efficiency over a large range of operating conditions and working with high cascade pressure ratios. But, for the high cascade pressure ratio considered in this study, BZT effects play a minor role in efficiency improvement. The use of properly designed turbine cascades working with somewhat lower pressure ratios could allow higher efficiency improvements due to BZT effects, opening the door to the development of BZT turbines for Organic Rankine Cycles. The results in [47] are widely presented in Chapter 4.

1.1.3. GA-Hardness of Dense gas Flow optimization problems

In spite of the increasing success of GAs for aerodynamics applications, no systematic studies of their convergence properties for aerodynamic problems of interest exist. Specifically, information lacks about how the flow-physics of a given problem affects the objective function, and hence, GA convergence. An objective function is informally defined to be GA-hard when a GA cannot detect an optimum within a reasonable number of iterations. One of the major causes of GA-hardness is the strong coupling in the objective function among different components of the high-dimensional search space. This phenomenon is termed *epistasis*. Epistasis variance, introduced by Davidor [58] in 1991, is a measure for the GA-hardness of a function and has been used to predict the performances

of GA using binary encoding. An extension of the epistasis concept to real encoding has been proposed by Rochet in [59], but it has not found application in practice. An alternative measure of GA-hardness well suited for real encoding, is *fitness distance correlation* (FDC), introduced by Jones in [60]. FDC is a statistical correlation between the fitness of strings encoding a given shape and the distance of these strings to the nearest global optimum. In spite of these attempts, developing a general theory that explains the behavior of a GA and that is able to predict how it will perform on different problems remains extremely difficult. In [61] Naudts introduced a measure, called the site-wise optimization measure, which suffers less from a number of problems encountered with the two known measures (epistasis variance and fitness distance correlation). The measure is based on an algorithmically defined property of the fitness landscape. This effort does not lead to a successful GA-hardness measure, however. A second possible cause of GA-hardness is the fact that a GA sometimes has to traverse a large part of the search space before it can reach the optimum of a function. For this aspect in [62] and in [61] an approach based on the construction of so-called “long path” is proposed. One necessary component is the ability to create what it is called a controlled path: a fitness function which leads a GA through successive areas of the search space.

For BZT-flow optimization problems, a marked sensitivity of GA convergence to the starting population and solution parameters such as flow Mach number and thermodynamic operating conditions has been observed [48][57]. In order to better understand this phenomenon, a systematic study of GA convergence for both perfect and dense gas flows at different operating conditions has been made by Cinnella&Congedo in [48] and in [57]. This study shows that the greatest convergence difficulties are encountered for optimization problems such that airfoil shapes close to the optimum generate flow-fields characterized by extremely weak shocks. This is particularly true for flows of BZT gases, whose peculiar property is to give rise to flow discontinuities much weaker than those characterizing perfect-gas flows. To reduce this difficulty to converge, a very efficient objective-function evaluation procedure based on Richardson extrapolation is proposed by Cinnella&Congedo in [57]. This procedure is explained in 3.3.2, and the main results will be presented in 4.5.

1.2. Overview of the following chapters

In Chapter 2 the formulation for the Navier-Stokes Equations and the thermodynamic models, necessary to simulate dense gas effects, are presented. Then, the numerical solvers (on structured and unstructured grids) are briefly described.

Chapter 3 describes the optimization techniques used in this work. Main features of Genetic Algorithms and Gradient Based Methods are presented. An innovative way to improve the convergence velocity will be introduced.

Chapter 4 presents a detailed description of the most important results achieved. The results of a transonic flow past the classical airfoil NACA0012 will be presented. Then, a flow past a blade turbine is considered. Then, the results obtained for three numerical optimizations will be described. The first one is the shape optimization of an isolated airfoil in the inviscid case. The purpose is the minimization of the drag coefficient for a symmetric airfoil. Then a multi-objective optimization is considered in order to increase the lift-to-drag ratio in different operating conditions. The second result consists in the extension of previous findings to the viscous case. The third one is the shape optimization of a turbine blade. The maximization of the efficiency is pursued by fixing the pressure jump in the turbine. Finally, a numerical study concerning the genetic algorithm convergence for dense gas flow is presented. A new approach will be introduced in order to speed up the Genetic Algorithm convergence.

Chapter 5 deals with the conclusions of this work. Finally suggestions for future work are proposed.

2. Governing equations and flow solvers

2.1. The Euler and Navier-Stokes equations for single-phase non reacting flows

The integral conservation laws for mass, momentum, and energy may be written for a control volume fixed in space as follows (by neglecting the body force):

$$\frac{d}{dt} \iiint_{\Omega} w d\Omega + \iint_{\partial\Omega} (f - f_v) \cdot \vec{n} dS = 0 \quad (\text{Eq. 5})$$

where $w = (\rho \quad \rho\vec{v} \quad \rho E)$ is the conservative variable vector, \vec{n} is the outer normal to $d\Omega$, $f = (\rho\vec{v} \quad p\bar{I} + \rho\vec{v}\vec{v} \quad \rho\vec{v}H)^T$ and $f_v = (0 \quad \bar{\tau} \quad \bar{\tau} \cdot \vec{v} - \vec{q})^T$ are respectively the inviscid and the viscous part of the flux density, \bar{I} is the unit tensor, \vec{v} is the velocity vector, E is the specific total energy, H is the specific total enthalpy, $\bar{\tau} = 2\mu(\nabla\vec{V} + \nabla\vec{V}^T) - \frac{2}{3}\mu(\nabla\vec{V})\bar{I}$ is the viscous stress tensor, and $\vec{q} = -k\nabla T$ the heat flux vector T being the absolute temperature.

The viscosity μ can not be computed through the well-known Sutherland Law. For the computation of viscosity and of the thermal conductivity, the approach widely described in 2.2.2 is used.

This system of equation is completed by the thermal and caloric equation of state (respectively of the form $p = p(\rho, T)$, and $e = e(\rho, T)$). There will be a detailed description of the equations of state in 2.2.1

2.1.1. Rans Equations

Since the full resolution of the NS equation requires the consideration of a big range of length and time scales, the compressible Reynolds-averaged Navier–Stokes equations RANS equation are used to limit the computer costs (For a detailed description of these equations see [63]). The investigation of turbulent dense gas flows past an airfoil is undertaken, based on the following working hypotheses: (a) flow conditions are supposed

to be sufficiently far from the thermodynamic critical point, so that dense gas effects such as dramatic variations of the fluid specific heat and compressibility can be neglected; in these conditions, density fluctuations will not be as huge as in near-critical conditions and subsequently the turbulence structure will not be affected significantly; (b) at least for equilibrium boundary layers, the mean flow behavior can be predicted adequately using RANS completed by an eddy viscosity turbulence model; similarly, the turbulent heat transfer can be modelled through a "turbulent Fourier law", as usual for PFG flows, where the turbulent thermal conductivity is computed in a classical way by introducing a turbulent Prandtl number, assumed to be roughly constant and $O(1)$ throughout the flow. Hypothesis (a) is justified by the fact that the flows of interest for this study actually do not evolve in the immediate neighborhood of the critical point; and in fact, if inviscid analyses and computations show an uncommon variation of the fluid speed of sound (and hence compressibility) with pressure perturbations, nevertheless the magnitude of these variations is approximately of the order of those occurring in perfect gases. Moreover, peculiar dense gas phenomena related to flow heating or cooling are excluded from considerations, since the airfoil wall is supposed to be adiabatic. On the contrary, Hypothesis (b) should be considered with some caution. On the one hand, if Hypothesis (a) is verified, it seems quite reasonable to apply to compressible dense gas flows turbulence models initially developed for incompressible flows of perfect gases and currently extended in the common practice to compressible PFG flows; on the other hand, more or less strong pressure gradients and shock waves characterizing the outer inviscid flow are likely to affect the boundary layer, which can no longer be considered an "equilibrium" one; this is also true for the reference PFG flows considered in the study, characterized by strong shock waves and shock/boundary layer interactions. Thus, aerodynamic performance predictions will necessarily be affected by deficiencies inherent with the chosen turbulence model. Nevertheless, since investigations are intended to provide trends of behavior more than accurate values of the computed aerodynamic coefficients, use of hypothesis (b) represents a means of obtaining preliminary information about realistic dense gas flows with a reasonable computational expense. Specifically, present results have been obtained using the simple algebraic model of (Baldwin & Lomax 1978), whose deficiencies in nonequilibrium boundary layer are well known (see for example [63], for a wider discussion): for example, flow features such as the location of shock waves and the length

of separation bubbles will not be predicted accurately. Nevertheless, it is expected that the model will roughly be able to predict the main trends and qualitative features of the flow field.

2.2. Thermodynamic models

2.2.1. Equations of state

The perfect gas equation of state is not valid at temperatures and pressures of the order of magnitude of those of thermodynamic critical point. Then other more complex equations of state should be used.

The van der Waals equation of state is the earliest attempt to correct the perfect gas law in order to take into account co-volume effects and attractive intermolecular forces. It only satisfies two thermodynamic constraints: the horizontal slope and inflection of the critical isotherm at the critical point. However, these are sufficient conditions that make the van der Waals equation capable to model BZT fluid behavior. It has the following general form:

$$p = \frac{RT}{V - \beta_{vdW}} - \frac{\alpha_{vdW}}{V^2} \quad (\text{Eq. 6})$$

where α_{vdW} , β_{vdW} , are some coefficients obtained by imposing that $\frac{\partial^2 p}{\partial v^2} = 0$ at the critical point.

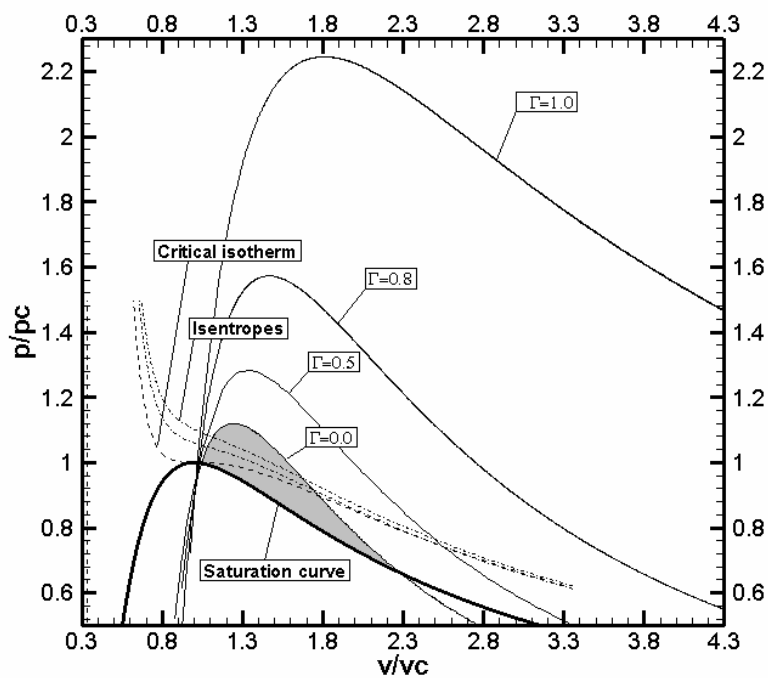
In the limit $c_v / R \rightarrow \infty$, the isentropes and isotherms coincide. Therefore, a van der Waals gas with sufficiently high $c_v / R \rightarrow \infty$ ratio is expected to exhibit reversed isentrope concavity above the upper saturation curve: hence it possesses BZT properties. It is possible to show that, taking the specific heat ratio γ in the range $1 < \gamma < 1.06$, a region of negative values of the Fundamental Derivative appears. The van der Waals thermodynamic model is computationally inexpensive (because it's possible to write an explicit relation between pressure and internal energy), and has been often utilized to provide a qualitative description of BZT fluid flows. On the other hand, this model is not very accurate for thermodynamic conditions close to saturation, i.e. the region of interest in the present study, and largely over-predicts the extent of the inversion zone [6]. The Amagat (p-v) diagrams reported in Figure 1a give an idea of the behavior of a van der Waals gas with $\gamma =$

1.0125, representative of a generic heavy fluorocarbon. The van der Waals gas exhibits a very large inversion zone. Outside this zone, the fundamental derivative quickly increases, reaching values close to 3 already at a short distance from the transition line, and tends to the perfect gas value when the specific volume tends to infinity.

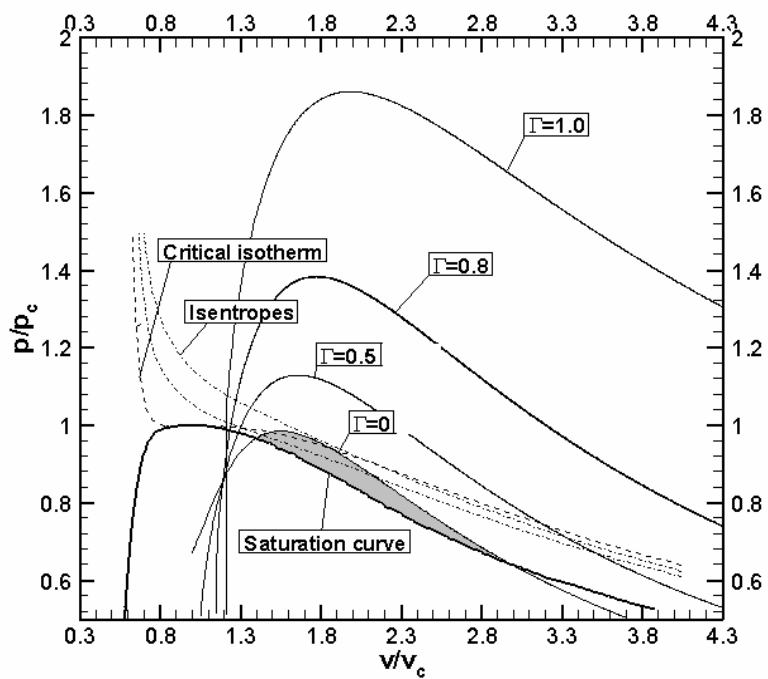
A more accurate model is the the Martin-Hou equation of state [3], which provides a realistic description of the gas behavior and of the inversion zone size:

$$p = \frac{RT}{(V-b)} + \frac{A_2 + B_2T + C_2e^{-5.475\frac{T}{T_c}}}{(V-b)^2} + \frac{A_3 + B_3T + C_3e^{-5.475\frac{T}{T_c}}}{(V-b)^3} + \frac{A_4}{(V-b)^4} + \frac{B_5T}{(V-b)^5} \quad (\text{Eq. 7})$$

where the coefficient A_i , B_i , C_i , are functions of the particular gas considered, T_c is the critical temperature, and b is the co-volume. Such equation, involving five virial terms and satisfying ten thermodynamic constraints, ensures high accuracy with a minimum amount of experimental information. A power law is used to model variations the low-density specific heat with temperature. It is not possible to explicitly relate the pressure with the internal energy, that requires often an iterative method to compute thermodynamic properties. In the Figure 1b, the Amagat (p-v) diagram of a real gas modelled through the Martin-Hou equation of state, namely, heavy fluorocarbon pf-perhydrouorene (commercial name PP10) is reported. On the contrary with respect to the vdW equation (see Figure 1a), the inversion zone for PP10 is much more reduced. Nevertheless, the increase of Γ outside the inversion zone for increasing pressure is much slower. For further details concerning the evaluation of the coefficients A_i , B_i , C_i see [43].



(a)



(b)

Figure 1: Amagat diagrams for a van der Waals BZT gas with $\gamma=1.0125$ (a) and for the heavy fluorocarbon PP10 modeled through the Martin-Hou equation of state (b). The shaded region represents the inversion zone.

2.2.2. Laws for viscosity and thermal conductivity

Viscous effects in flows of dense gases have remained largely unexplored. One of the most important differences between dense gases and perfect gases is the downward curvature and nearly horizontal character of the isotherms in the neighborhood of the critical point and upper saturation curve in the p-v plane: the region of downward curvature of the isotherms is associated with the aforementioned reversed behavior of the sound speed in isentropic perturbations. In the same region, the specific heat at constant pressure, c_p , can become quite large: this strongly influences the development of the thermal boundary layer and its coupling with the viscous boundary layer in high-speed flows. In the dense gas regime the dynamic viscosity μ and the thermal conductivity κ cannot be longer considered independent of the temperature and pressure, even in flows with relatively small temperature variations. On the other hand, the well-known Sutherland law, commonly used to represent viscosity variation with temperature, becomes invalid, as it is based on the hypothesis that the gas molecules act as non-interacting rigid spheres, and intermolecular forces are neglected. The complexity of the behavior of μ in the dense regime can be anticipated by recalling that the viscosity of liquids tends to decrease with increasing temperature, whereas that of gases tends to increase: the dense gas regime is a transition between these two qualitatively different behaviors. Similarly, the classical approximation of nearly constant Prandtl number ($Pr = \mu c_p / k \approx const$) cannot be used any more. As the thermal conductivity has roughly the same variation as viscosity with temperature and pressure, the behavior of Pr tends to be controlled by variations of c_p . In regions where c_p becomes large, strong variations of Pr can be observed, contrarily to what happens in perfect gases. Nevertheless, if the immediate vicinity of the thermodynamic critical point is excluded from considerations, the Prandtl number remains of order one, similar to perfect gases. In contrast, the Eckert number ($Ec = U_0^2 / (c_p T_0)$, where U_0 and T_0 refer to a suitable reference state) decreases significantly. Small flow Eckert number implies reduced sensitivity of the boundary layer to friction heating that remains negligible even at moderately large supersonic Mach numbers. Moreover, for flows past adiabatic walls the temperature, and thus also the density, is almost constant across the boundary layer.

The fluid viscosity and thermal conductivity are evaluated using the method proposed in [9][13]. The viscosity (measured in μPoise) is related to the absolute temperature through the formula:

$$\mu = 40.785 \frac{F_c M_w^{1/2} T^{1/2}}{V^{2/3} \Omega_v} \quad (\text{Eq. 8})$$

where M_w is the molecular weight in g/mol and V_c is the critical volume in cm^3/mol . The coefficient F_c is given by

$$F_c = 1 - 0.2756\omega + 0.059035\delta_r^4 + \xi \quad (\text{Eq. 9})$$

where ω is the acentric factor, δ_r is a dimensionless dipole moment,

$$\delta_r = 131.3 \frac{\delta}{(V_c T_c)^{1/2}} \quad (\text{Eq. 10})$$

with δ measured in Debyes, and ξ is a special correction for highly polar substances. The viscosity collision integral Ω_v is provided by

$$\Omega_v = \left[A(T^*)^{-B} \right] + \left[C \exp(-DT^*) \right] + \left[E \exp(-FT^*) \right] \quad (\text{Eq. 11})$$

where $T^* = 1.2593(T/T_c)$, $A=1.16145$, $C=0.52487$, $D=0.77320$, $E=2.16178$ and $F=2.43787$

The thermal conductivity κ is provided by:

$$\frac{\kappa M_w}{\mu C_v} = \frac{3.75\Psi}{C_v / R} \quad (\text{Eq. 12})$$

where M_w is the molecular weight in Kg/mol, c_v is the constant volume specific heat in J/(mol K), R is the universal gas constant in J/(mol K), and the coefficient Ψ is:

$$\Psi = 1 + \alpha_1 \frac{0.215 + 0.28288\alpha_1 - 1.061\beta + 0.26665\Xi}{0.6366 + \beta\Xi + 1.061\alpha_1\beta} \quad (\text{Eq. 13})$$

with

$$\alpha_1 = (C_v / R) - 3/2; \quad \beta = 0.7862 - 0.7109\omega + 1.3168\omega^2; \quad \Xi = 2.0 + 10.5(T/T_c)^2.$$

2.3. Flow solvers

2.3.1. Structured solver

A CFD structured code (property of the Fluid Dynamic Lab of Department of Engineering for Innovation, University of Salento) has been modified to compute dense gases

(indicated in the following by SGS). The governing equations are discretized using a cell-centered finite volume scheme for structured multi-block meshes of third-order accuracy, which allows computing flows governed by an arbitrary equation of state [39]. The scheme is constructed by correcting the dispersive error term of the second-order-accurate Jameson's scheme [66]. The use of a scalar dissipation term simplifies the scheme implementation with highly complex equations of state and greatly reduces computational costs. In order to preserve the high accuracy of the scheme on non-Cartesian grids, the numerical fluxes are evaluated using weighted discretization formulas, which take into account the stretching and the skewness of the mesh: this ensures truly third-order accuracy on moderately deformed meshes and at least second-order accuracy on highly distorted meshes (see [67] for details). The equations are then integrated in time using a four-stage Runge-Kutta scheme [66]. Local time stepping, implicit residual smoothing and multigrid are used to efficiently drive the solution to the steady state. For external flows, non-reflecting boundary conditions based on a multidimensional method of characteristic are applied at the far-field boundaries; an adiabatic wall condition is imposed at solid boundaries. The accuracy properties of the numerical solver just described have been demonstrated in previous works [39][40], and will not be discussed further. The numerical method is extended to the Navier-Stokes Equations using a classical second-order discretization of the viscous term.

2.3.2. Unstructured solver

An unstructured CFD solver (developed in the Sinumef Lab at the Ensam in Paris) has been modified to simulate Dense Gases (see [43])(indicated in the following by UGS). This allows a cross validation concerning the numerical results by comparing the solution to those obtained with the structured code. This unstructured solver (UGS) is also based on a cell-centered finite-volume discretization of (Eq. 5) but formulated on a general unstructured grid dividing the spatial domain into a finite number of triangles or quadrangles; the time rate of change of the cell-averaged state vector w is balanced with the area-averaged (inviscid) fluxes across the cell faces. The fluxes are computed across each cell face using the HLL scheme [68]; second-order spatial accuracy is ensured thanks to a MUSCL-type reconstruction process on the conserved variables [69], where the gradient estimates required at each cell center are obtained through a least-square formula. Since the solver will be applied to the computation of flows containing discontinuities, the

reconstruction formula includes a limitation step based on the now standard approach proposed in [70] and revisited in [71] which ensures oscillation-free shock-capturing. Fast convergence to steady state is provided by making the scheme implicit following a procedure inspired from [72]: a simple first-order Rusanov-type implicit stage allows the use of large CFL numbers and is solved by an inexpensive point-relaxation technique. The numerical flux through the boundary edges is computed using an inflow / outflow characteristic-based condition to define the ghost-cell states at the far-field boundary and a mirror boundary condition to define the ghost-cell states at the wall.

2.3.3. How a more complex equation of state affects a NS code

Using a perfect gas equation of state is straightforward because of the direct relation between the pressure and the internal energy. The van der Waals equation is more complicated of the PGF equation of state, but it's always possible to write a direct relation between pressure and internal energy (for details see [43]). But, as seen in 2.2.1, VDW equation overestimate the inversion region, and it's not accurate for describing the variation of Γ . Then the Martin-Hou equation has to be used, but in this case it's not possible to derive an explicit relation between pressure and internal energy. Generally, an iterative method is necessary to compute thermodynamic properties (for example to compute the primitive variables by starting from the conservative variables). Newton-Raphson Method is used because of its good accuracy and convergence velocity (For details in the implementation see [43]). Generally, if a different equation of state is used, it's necessary to change all the formulations that adopt implicitly a PFG equation of state. Obviously it's taken for granted that the computation of thermodynamic properties changes starting from different thermodynamic relations (typically sound of speed and internal energy). For a very detailed description of the main thermodynamic properties with the different equation of state see [43].

For what concerns the solvers used in this work, the numerical schemes formulations used in SGS (2.3.1) and in UGS (2.3.2) are independent from the equation of state. A different formulation for the non-reflecting boundary conditions based on method of characteristic has been used (typically the computation of Riemann invariants changes, because it is usually written by considering a PFG equation of state).

3. Optimization tool

3.1. Genetic Algorithms

Genetic algorithms have been successfully applied for some time now to shape optimization in aeronautics [73][74][75][76]; in spite of their cost, they have proved their interest with respect to gradient-based methods because of their high flexibility (stemming from the fact they only require values of the objective function(s) to efficiently explore the parameters space in search of an optimum), and also because of their ability to find global optima of multi-modal problems. Moreover, so-called Pareto-type genetic algorithms are of particular interest for multi-objective optimization since they provide, after only a few generations, a set of non-dominated solutions. On the contrary, a conventional gradient-based method needs several independent runs to achieve similar results [76][77]. The MOGA (Multi-objective Genetic Algorithm) is also well suited to the solution of multi-objective problems, such as multi-point performance improvement for a lifting airfoil. The MOGA applied in this study is the Non-Dominated Sorting Algorithm (NSGA) proposed by Srinivas and Deb [78]. At a given generation number, all individuals in the population are ranked according to non-domination criteria that allow to take into account in a simultaneous way a set of objective functions. The set of individuals that dominate all the other members of the population without dominating each other is designated as front of rank 1; the set of dominant individuals in the population deprived from the members of rank 1 form the front of rank 2, and so forth until the whole population is classified into a series of dominance fronts. The individuals scattered along the front of rank 1 are assigned the same pseudo-fitness function, arbitrarily fixed to unity, since they are equally well-adapted and therefore should be given the same potential of reproduction. However, in order to favor the population diversity along the front, the pseudo-fitness value is decreased for individuals located in crowded areas of the front: practically, the initial uniform value of the pseudo-fitness function is divided by a number strictly larger than unity for individuals with neighbors within a prescribed distance. Next, the smallest value of the modified pseudo-fitness function obtained for individuals belonging to the front of rank 1 is decreased from a small number ϵ and assigned to all members of the front of rank 2; next this uniform value is then itself modified as previously explained in order to

promote the selection of isolated individuals along the front and thus to ensure a maximum of diversity. Once each individual has been given a pseudo-fitness value, it is selected for reproduction using a proportional selection operator; finally, the individuals retained in the mating pool are submitted to crossover and mutation in order to explore the research space and yield a front of rank 1 closer and closer to the global Pareto front of the problem. The main tuning parameters of the algorithm are the population size, the number of generations, the crossover and mutation probabilities p_c , p_m and the so-called sharing parameter σ used to take into account the relative isolation of an individual along a dominance front. Typical values for p_c , p_m are respectively 0.9 and 0.1; values of σ are retained following a formula given in [78] which takes into account the population size and the number of objectives. Theoretically, the population size and the number of generations should be chosen according to the number of parameters and objectives of the optimization problem under study; in practice however, the population size and number of generations are fixed by the global amount of CPU time devoted to the computation : taking too small a population may rapidly lead to a local optimum and make useless the iteration process on the generation number; reversely, a large population will impose a limited number of generations which could not allow the population to evolve sufficiently towards the optimum.

3.2. Gradient Based Methods

For computing the BFGS algorithm, the multi-objective design environment (mode)FRONTIER software (produced by ESTECO s.r.l.) has been used. The classical Broyden-Fletcher-Goldfar-Shanno (BFGS) optimization algorithm is a variable metric method, i.e., a so-called quasi-Newton method. The function is locally approximated with a quadratic form, function of the gradient and of a suitable approximation of the Hessian. For a quadratic function the Newton Method gives the solution for a minimum. The Hessian matrix is not used, but instead an approximation of it is built up iteratively, making use of the information about the function and the gradient values in the successive iterated points: so the “quasi” in the name of the method. Once the Newton step is computed, the BFGS algorithm performs a linear search along that direction, starting from the full step, and then if the decrease in the objective function is not satisfactory, trying iteratively a shorter and shorter step until a satisfactory point is found. In this way, if the

current quadratic approximation is good, we can achieve fast convergence to the minimum; otherwise, if the approximation is bad, we are at least guaranteed that initially f decreases along the Newton direction. Further details can be found in [79].

3.3. Metamodels

Metamodel is a low cost (and thus approximate) surrogate evaluation model, built using existing information, which can be used instead of the computationally expensive, exact evaluation tool. The cost of training a metamodel depends on its type and the training set size. Compared to the cost of an exact evaluation, that of training and using the metamodel is relatively low. Among the frequently used metamodels there are polynomial interpolation, artificial neural networks, gaussian processes, support vector machines. There are two ways of using the metamodels, the first called “off-line”, in which it is decoupled from the optimization loop, and the other called “on-line” in which the metamodels are trained during the optimization using updated information. In the following paragraphs the Artificial Neural Network, and a Method based on the Richardson Extrapolation will be described.

3.3.1. Artificial Neural Network

GAs require evaluations of the fitness function for each individual in a generation, and this during several generations, until an optimal individual is selected: this is the major cause of their high computational cost. However, this drawback can be overcome if the fitness function is related to the design variables through an analytical expression. In order to reduce computational costs for viscous dense-gas flow optimization problems, the flow solver (actually viscous computations have been just done with SGS) and GA are coupled with an artificial neural network (ANN). ANN are non-linear statistical data-modeling tools, based on a biologic analogy. They can be used to model complex relationships between inputs and outputs or to find patterns in data. A very important feature of these networks is their adaptive nature, i.e. their capability of “learning”. This feature makes such computational models very appealing in application domains where one has little or incomplete understanding of the problem to be solved but where training data is readily available. ANN involve a network of simple processing elements (nodes or artificial neurons) which can exhibit complex global behavior, determined by the connections between the processing elements and element parameters. According to the choice of the

node functions and to their architecture, several ANN can be constructed. In the present work, a neural network based on radial basis functions is adopted [80]. The network is formed by an input layer, and intermediate layer, and an output layer. Values of the design variables are introduced in the input layer, whereas a single value, *i.e.* the fitness of the individual, is obtained as a linear combination of the intermediate layer values and returned as the network output. The weights of the linear combination are determined through a training procedure, and the number of neurons involved is taken equal to the number m of individuals of the training set. The approximation function associated to the j th neuron of the intermediate layer is of the form:

$$h_j(x) = \exp\left[-\left(\frac{E_j}{r}\right)^2\right] \quad (\text{Eq. 14})$$

Where \mathbf{x} is the input design variable vector, $E_j = \|\mathbf{x} - \mathbf{x}_j\|$, is the distance of the individual represented by \mathbf{x} from the j th individual of the training set, and r is an attenuation coefficient. The fitness of \mathbf{x} is then computed through the linear relation:

$$f(x) = \sum_{j=1}^m \omega_j h_j(x) \quad (\text{Eq. 15})$$

The weights ω_j are determined by requiring that the approximation function f satisfies the interpolation conditions:

$$y_k = f(x_k) \quad \forall k = 1, \dots, m \quad (\text{Eq. 16})$$

where the $\{y_k\}$ represent the (known) values of the fitness functions associated to individuals of the training set. With this requirement, the training problem reduces to the solution of a linear system of m equations in m unknowns ω_j .

3.3.2. Richardson Extrapolation

In order to evaluate the difficulty for a Genetic Algorithm to converge, the fitness distance correlation method of [81] is considered. Let us consider a fitness function f :

$$f : s \in S \subseteq \mathfrak{R}^n \rightarrow f(s) \in \mathfrak{R} \quad (\text{Eq. 17})$$

(with S the search space and \mathbf{s} an ordered N -ple of input variables defining a given individual) characterized, without loss of generality, by a unique global optimum \mathbf{s}^* . The *fitness distance correlation* (FDC) of f with respect to the fitness information in a discrete sample of the search space $P \subset S$ is defined as:

$$fdc_P(f) = \frac{\sum_{s \in P} [(f(s) - \bar{f}_P)(d(s, s^*) - \bar{d}_P)]}{\left(\sum_{s \in P} (f(s) - \bar{f}_P)^2 \right)^{\frac{1}{2}} \left(\sum_{s \in P} (d(s, s^*) - \bar{d}_P)^2 \right)^{\frac{1}{2}}} \quad (\text{Eq. 18})$$

with $\bar{f}_P = \frac{1}{|P|} \sum_{s \in P} f(s)$ and $\bar{d}_P = \frac{1}{|P|} \sum_{s \in P} d(s, s^*)$ the mean fitness and the mean distance of the sample individuals from the global optimum, respectively. The following distance definition is used:

$$d(s, s^*) = \sqrt{\sum_{i=1}^N \frac{(s_i - s_i^*)^2}{\Delta_i}} \quad (\text{Eq. 19})$$

with s_i the i -th input variable of the N-ple and Δ_i its range of variation. If a maximization (respectively, minimization) problem is considered, the FDC returns a value of -1 for a fitness function of the form

$$f = C_1 - C_2 d(s, s^*) \quad (\text{resp., } f = C_1 + C_2 d(s, s^*)), \quad (\text{Eq. 20})$$

with $C_1, C_2 \in \mathfrak{R}$, $C_2 > 0$. FDC measures the deviation of a fitness function from the class of strictly concave (resp., strictly convex) functions of the form of ((Eq. 20)): if the FDC of a given fitness function is close to -1 (resp., +1), this one can be easily optimized by a GA, whereas if $FDC \approx 0$ (no correlation with function (Eq. 20)), the function is GA-hard.

The use of a more accurate scheme and of finer meshes allows reducing the GA-Hardness of an optimization problem. Unfortunately, the use of very fine meshes considerably increases computational costs. In order to alleviate this problem, a simple and effective method based on Richardson extrapolation is proposed (see [57]).

Let us note f_{2h} and f_h two estimates of the fitness function f , respectively computed on a ‘‘coarse’’ mesh $2h$ and on a finer mesh h . The approximation error in the two cases is:

$$\varepsilon_h = f_{exact} - f_h = Ch^p + T.O.S.; \quad \varepsilon_{2h} = f_{exact} - f_{2h} = C(2h)^p + H.O.T. \quad (\text{Eq. 21})$$

where p is the scheme’s convergence order, and C its error constant. Neglecting Higher Order Terms and combining the two equations above the following estimate of the exact solution is obtained:

$$f_{exact} \approx f_{Richardson} = f_h + \frac{f_h - f_{2h}}{2^p - 1} \quad (\text{Eq. 22})$$

This value represents a better estimate of the fitness function than the previous ones. We decide to use this extrapolated value as an approximation of the fitness of a given individual in the GA. Precisely, the algorithm is as follows:

- 1) For each individual, a coarse and a fine mesh are generated, the coarser mesh being obtained from the finer one by halving the number of points in each direction;
- 2) a coarse-grid estimate of the fitness function is computed;
- 3) the coarse grid solution is used to initialize a fine-grid computation; a fine-grid estimate of the fitness function is obtained;
- 4) the values obtained at steps (2) and (3) are used to compute a more accurate estimate of the fitness function via formula (10);
- 5) this value is compared with fitness values obtained for the other individuals in the population in order to perform standard operations of selection, crossover and elitism in the GA.

4. Results

This Chapter is constituted by five sections. The first two are devoted to a better understanding of dense gas flows fluid-dynamics. Dense gas flows past an isolated airfoil and transonic dense gas flows through a turbine cascade are considered. The section third and fourth concern the results obtained by means of shape optimization related to an isolated airfoil and a turbine blade. In the last section the analysis of the GA-Hardness for dense gas flow optimization problems is presented.

4.1. Dense gas flow past an airfoil

A flow over a NACA0012 is considered. The working fluid in the following computations is PP10. The objective is to explore the influence of dense-gas effects on the airfoil aerodynamic performance, also in comparison with reference results for a perfect gas (PFG) flowing at the same free-stream conditions. Always a flow at $M_\infty = 0.85$, $\alpha = 1^\circ$ is considered. The accurate MAH equation of state is used as state law.

4.1.1. Choice of the operating conditions

For a dense gas, the parameters governing the flow are, in addition to the free-stream Mach number and angle of attack, the free stream thermodynamic conditions, i.e. the thermodynamic operation point. Just high subsonic freestream conditions are considered here. (A detailed study also about sonic, and low-supersonic freestream conditions over a NACA0012 airfoil are presented in [41]). For BZT inviscid steady flows, the flow adiabatic in the p - v plane is roughly superposed to the isentrope corresponding to free-stream conditions. In the p - v diagram, the locus of possible thermodynamic states of a flow field is then approximately superposed with the arch of the isentrope included between the minimum and maximum pressures in the flow. If the locus crosses the inversion zone, the flow field exhibits a region of BZT effects. The operation points chosen for the present study are picked on five different isentropes of the p - v plane. Figure 2 shows the five isentropes, the operation points, the inversion zone, and the dense gas region ($\Gamma < 1$) for PP10. Moving right to left along an isentrope the free-stream fundamental derivative Γ_∞ , initially positive, decreases, changes its sign where the isentrope crosses the inversion zone, reaches a minimum, then increases again (see Figure

3). For high-pressure operation points, Γ_∞ is greater than one. Isentropes S1 to S3 cross the inversion zone.

Isentrope S4 is approximately tangent to the transition line and represents a limiting case. Finally, isentrope S5 lies completely outside the inversion zone, but crosses the extended thermodynamic region where $\Gamma < 1$. For flows with free-stream entropy S5, BZT effects cannot appear, but significant DG effects related to reverse sound speed behavior are expected.

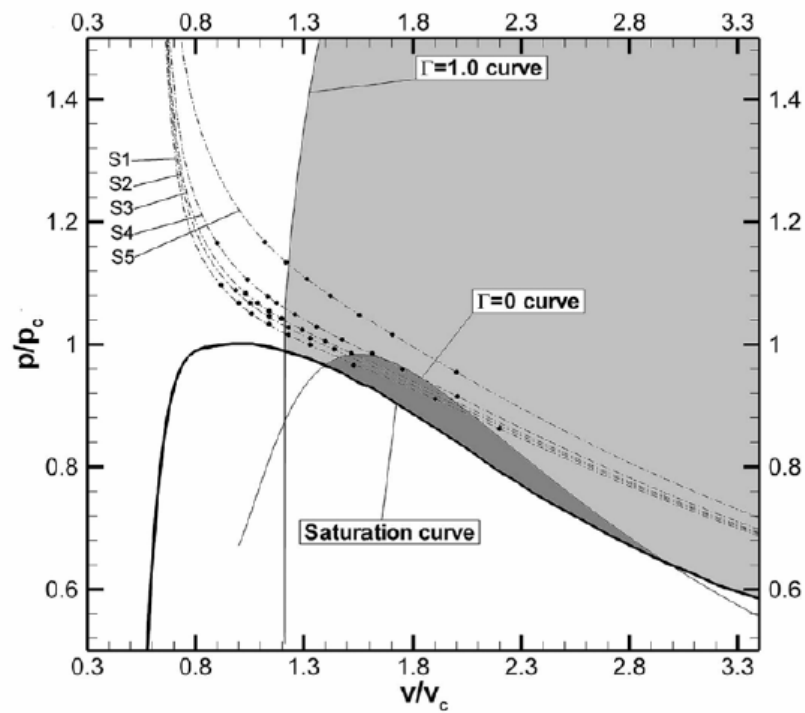


Figure 2: Location of the operation points in the $p - v$ diagram.

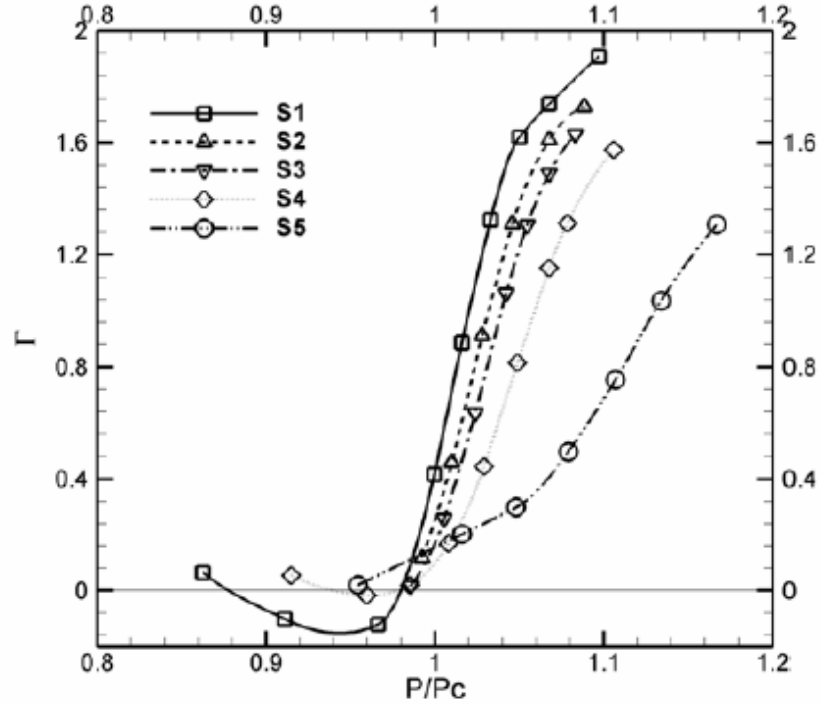


Figure 3: Fundamental derivative versus pressure along selected isentropes.

4.1.2. Inviscid Flow behavior

Inviscid flow computations are performed using three C-grids, formed by 136×20 , 272×40 and 544×80 cells, respectively. The outer boundary is about 20 chords away from the airfoil and the mean height of the first cell closest to the wall is about 5×10^{-2} chords on the medium grid. For most of the computations presented in the following, grid convergence for the wall pressure and Mach number has been obtained on the medium grid.

The reference solution for a perfect diatomic gas (specific heat ratio $\gamma = 1.4$) flowing at $M_\infty = 0.85$, $\alpha = 1^\circ$ is first considered (see for details [39]). The flow is characterized by two shocks at about 85% of the chord at the suction side, and 63% at the pressure side. The lift coefficient, drag coefficient, and lift-to-drag ratio computed with the present numerical method on the finest grid are:

$$C_L = 0.373; \quad C_D = 5.74 \times 10^{-2}; \quad C_L/C_D = 6.51.$$

Then, flows of the dense gas PP10 past the same airfoil are computed. Results obtained for lift, drag, and lift-to-drag ratio for different choices of the free-stream fundamental derivative and free-stream entropy are summarized in Figure 4. For the lowest values of

Γ_∞ , the drag is almost equal to zero (order 10^{-4}), then increases monotonically. The lift coefficient initially grows, reaches a maximum, and then drops dramatically. The lift-to-drag ratio is very poor for high Γ_∞ flows, but tends to infinity as the free-stream value of the fundamental derivative approaches unity. The best aerodynamic performance, offering a satisfactory trade-off between high lift and low drag is obtained for Γ_∞ approximately in the range $1 \div 1.3$: in such conditions, the flow displays higher lift and significantly reduced wave drag compared to PFG results. Note that the curves exhibit quite sudden changes in slope, which are related to corresponding changes in the flow patterns. In order to explain the computed behavior of the aerodynamic performance, a detailed analysis of the flow fields obtained for each operating condition is undertaken, which allows identifying three typical flow regimes, described in the following. For flows characterized by relatively low free-stream pressures and small values of the free-stream fundamental derivative (Γ_∞ less than about 1), the computed lift-to-drag ratio is extremely high, due to the very low values taken by the drag coefficient, although the lift coefficient is lower than in the perfect gas case. Inspection of the Mach number field shows that such flows remain entirely subsonic. Since the free-stream is uniform and steady and no viscous effects are taken into account, the flow should also be isentropic, with drag coefficient exactly equal to zero. In practice, small entropy gradients are generated close to the wall, because of numerical errors introduced by the numerical scheme and boundary conditions, which lead to small nonzero values, $O(10^{-4})$, for the computed drag. As a consequence, the computed lift-to-drag ratio is not unbounded, but $O(10^3)$. A typical pressure contour plot for this flow case is displayed in Figure 5 along with $\Gamma = 0$ contours. Typical distributions of the Mach number, pressure coefficient, fundamental derivative, and sound speed at the wall are presented in Figure 6. When a fluid particle from the free-stream approaches the airfoil along the wall streamline, it undergoes a compression and the local fundamental derivative grows, reaching a maximum at the stagnation point where $\Gamma_{\max} \approx 1.5 \div 2$. Then, Γ suddenly drops when the flow begins to expand accelerating over the top of the airfoil. Both pressure coefficient and Γ variations in the neighborhood of the stagnation point are very large, $O(1)$. If Γ_∞ is sufficiently small, roughly $\Gamma_\infty < 1$, the local fundamental derivative becomes smaller than 1, or even negative, less than 0.01 chords downstream the leading edge: consequently, the speed of sound grows sharply enough to counterbalance the increase of velocity and the flow remains subsonic. The smaller Γ , the steeper is sound speed growth.

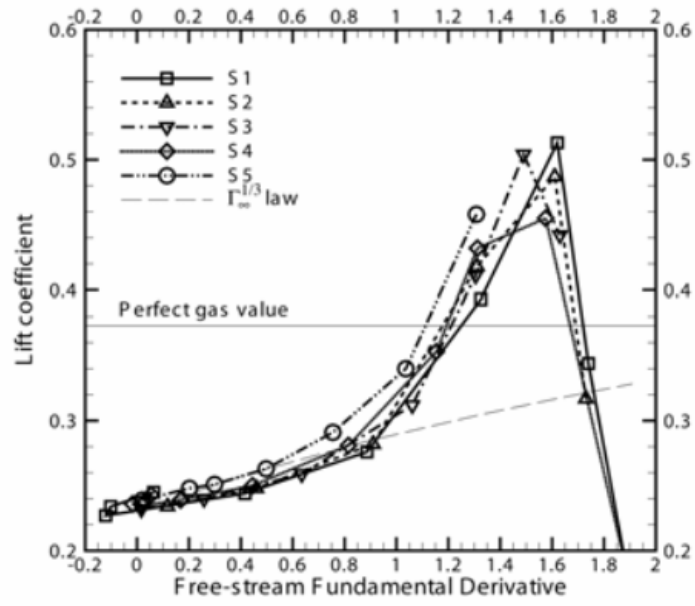
As high values of the sound speed are associated to low values of the compressibility parameter, flows with low Γ_∞ conserve a behavior closer to the incompressible one. In summary, for "sufficiently low" $\Gamma_\infty (< 1)$:

- (a) the flow past the airfoil is subsonic;
- (b) the drag coefficient vanishes;
- (c) lift is lower than in the perfect gas case, because of the reduced flow compressibility;
- (d) lift tends to increase with Γ_∞ .

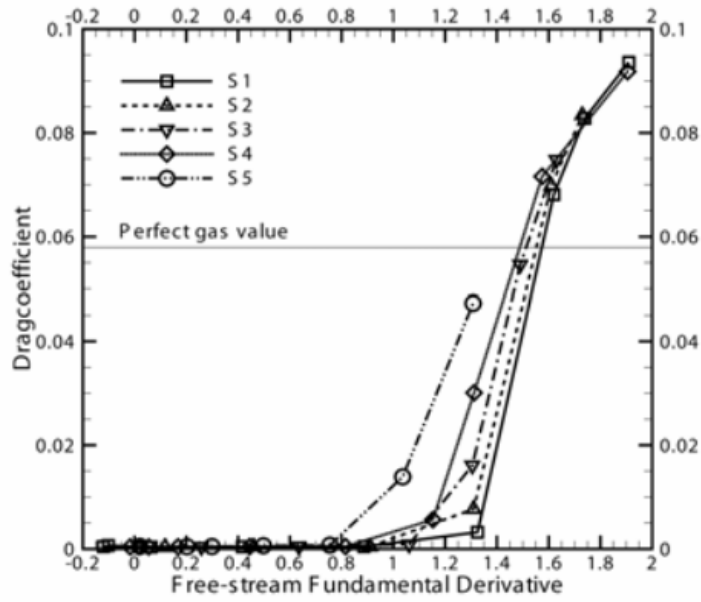
When Γ_∞ is approximately in the range $1 \div 1.5$ the flow patterns change dramatically. In this range, a significant growth in both lift and drag is observed with respect to the previous case (see Figure 4 a). Nevertheless, the lift-to-drag ratio is still about one order of magnitude greater than in the perfect gas case due, on the one hand, to high values obtained for the lift and, on the other, to very low wave drag. In this regime, the flow becomes supercritical. For operation points lying on S1 to S4, the flow-field displays significant BZT effects, which are responsible for the high aerodynamic performance. On the other hand, no BZT effects appear for operating conditions S5: however, since the fundamental derivative takes very small albeit positive values, the overall flow behavior does not differ very much from the other two cases: the flow patterns are similar to those obtained at operating conditions S1-S4 at slightly higher pressures. A typical view of the pressure contours for this flow regime is presented in Figure 7, whereas Figure 8 shows the wall distributions of the Mach number, pressure coefficient, fundamental derivative, and sound speed. For this kind of flows, characterized by higher free-stream Γ , the reversed behavior of the sound speed associated to flow regions with $\Gamma < 1$ is delayed, and the flow expands to supersonic conditions downstream the leading edge. Along the upper surface, if the free-stream values of Γ and of the entropy are sufficiently low, Γ may become negative just downstream the stagnation point, where the pressure is still steeply falling, so that an expansion shock is generated. Downstream of this shock, the pressure coefficient drops to values much lower than in the perfect gas case. The expansion shock is followed firstly by a continuous expansion and then by a gradual compression, which terminates in a compression shock as soon as the flow exits the inversion zone. Increasing Γ_∞ and/or the free-stream entropy, the change of sign of the fundamental derivative is delayed, or never happens (this is the case of conditions S5), and no expansion shock appears, the flow being

always recompressed through a classical shock at the rear part of the upper surface. Along the lower surface, only a weak compression shock forms. Both expansion and compression shocks have jump conditions in the vicinity of the transition line: the entropy jump across such shocks (normalized with the free-stream entropy) is $O(10^{-5})$, whereas it is $O(10^{-2})$ for perfect gas flow. Accordingly, the wave drag is approximately one order of magnitude lower with respect to the PFG value. In summary, flows in the second regime (called hereafter the low pressure transonic BZT regime) are supercritical and characterized by high lift and very low wave drag, due to the fact that shock waves occurring in the vicinity of the transition line are much weaker than usual. For operation points characterized by sufficiently low values of Γ_∞ and s_∞ , the aerodynamic performance is even further improved by the formation of an expansion shock close to the leading edge, which strongly enhances the suction peak, and consequently the lift, at the airfoil upper surface. This mechanism is similar to that observed in [40] for BZT flows of a van der Waals gas.

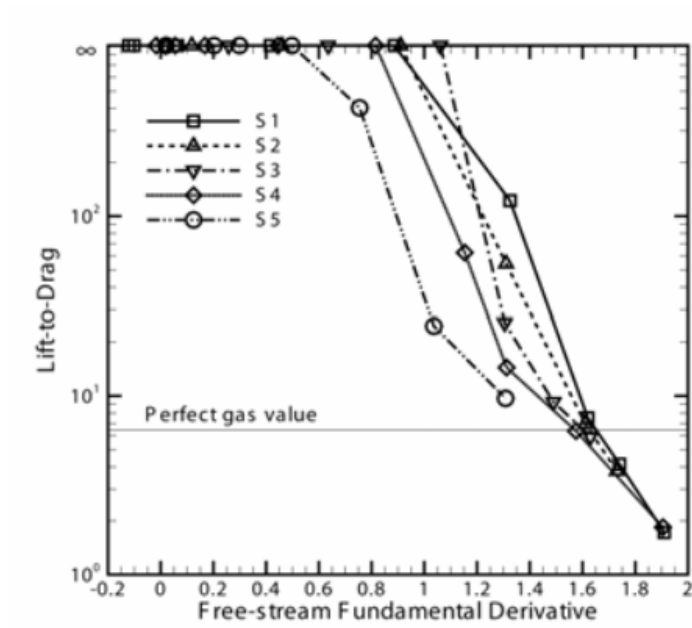
When Γ_∞ and/or s_∞ are even higher, the flow becomes qualitatively similar to that of a perfect gas. The flow accelerates from the stagnation point to supersonic velocities and then recompresses at the rear part of the airfoil by means of compression shocks. As the free-stream fundamental derivative is increased, the region of flow characterized by $\Gamma < 0$ becomes smaller and finally disappears. At the same time, the lift coefficient decreases, and the drag increases, due to the stronger entropy gradients generated across the shocks. This progressively reduces the airfoil aerodynamic performance, which finally becomes very poor. Figure 9 shows typical pressure contours for this kind of flow. Figure 10 illustrate the wall Mach number, pressure coefficient, fundamental derivative and sound speed at operating conditions $p_\infty/p_c = 1.17$, $\rho_\infty/\rho_c = 1.11$ on isentrope S4 ($\Gamma_\infty = 1.91$). At these extreme conditions, the fundamental derivative remains positive everywhere, and no BZT effects appear.



(a)



(b)



(c)

Figure 4: Aerodynamic coefficients versus free-stream fundamental derivative for flow at $M_\infty = 0.85$, $\alpha = 1^\circ$ past a NACA0012.

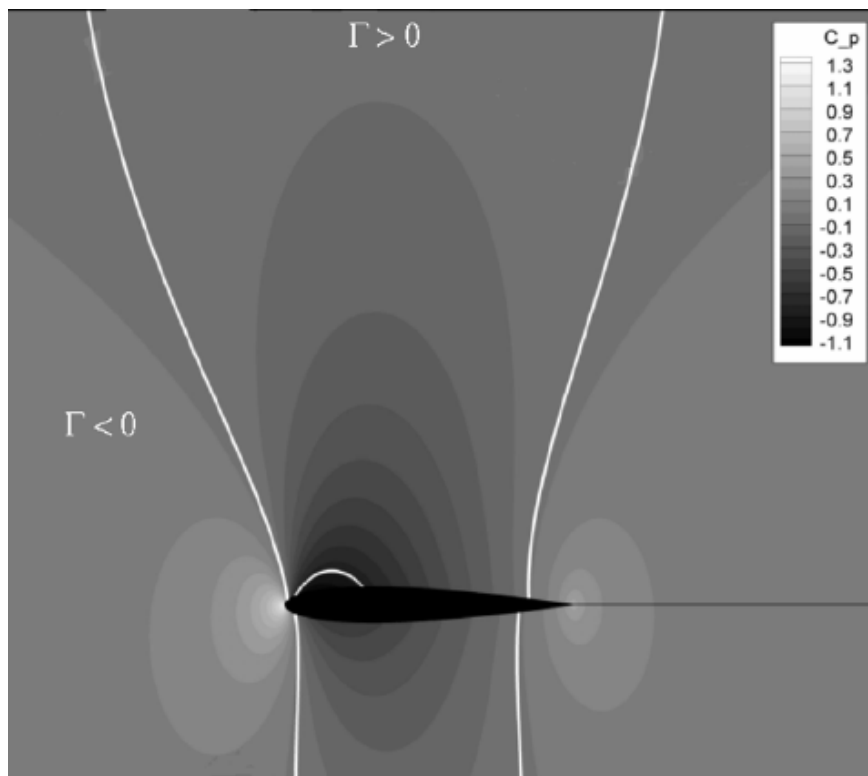


Figure 5: Pressure coefficient contours and $\Gamma = 0$ contours for operating conditions $p_\infty/p_c = 0.986$, $\rho_\infty/\rho_c = 0.658$, $\Gamma_\infty = 0.017$ (BZT subcritical regime).

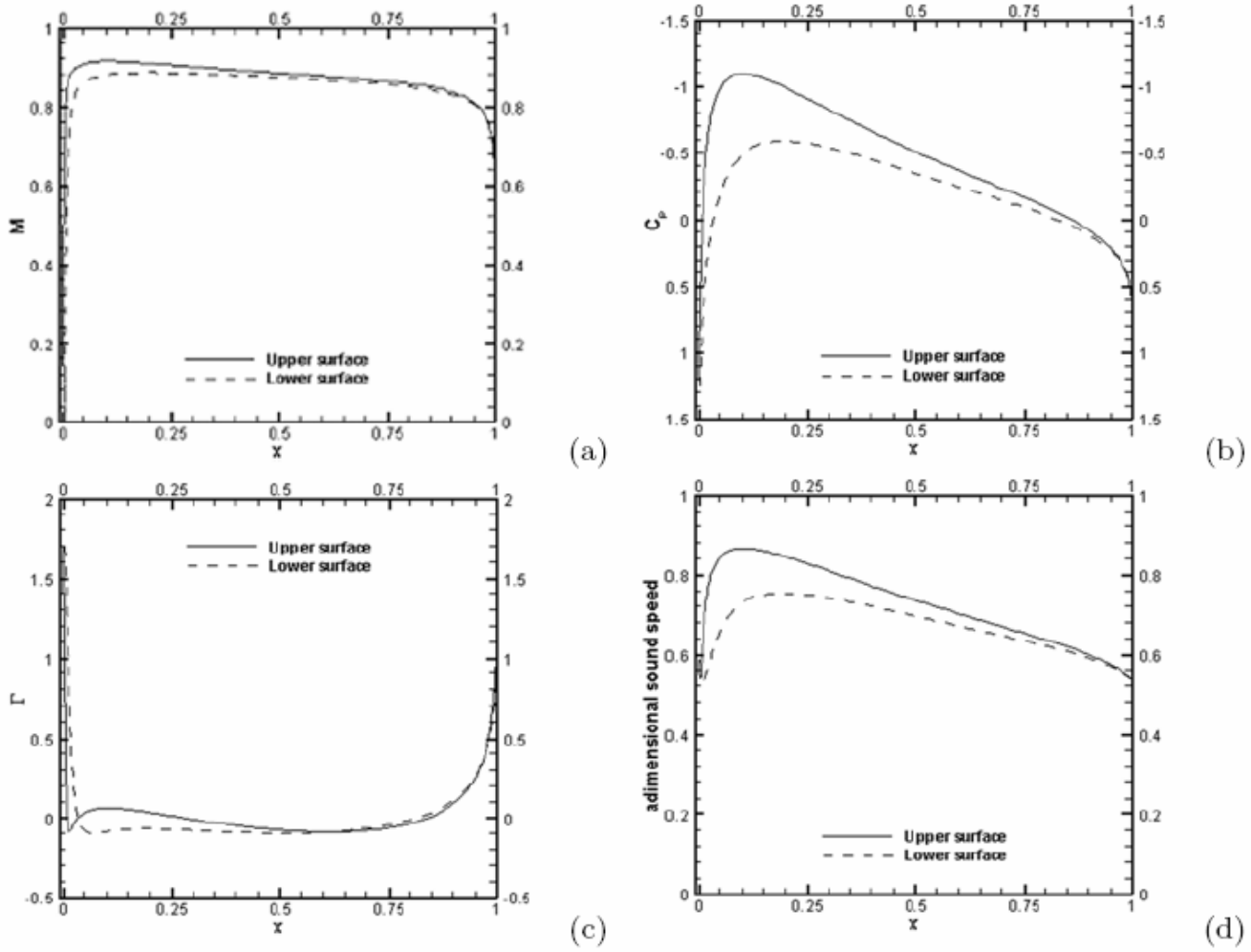


Figure 6: Wall distributions of the Mach number, pressure coefficient, fundamental derivative and sound speed for operating conditions $p_\infty/p_c = 0.986$, $\rho_\infty/\rho_c = 0.658$, $\Gamma_\infty = 0.017$ (BZT subcritical regime).

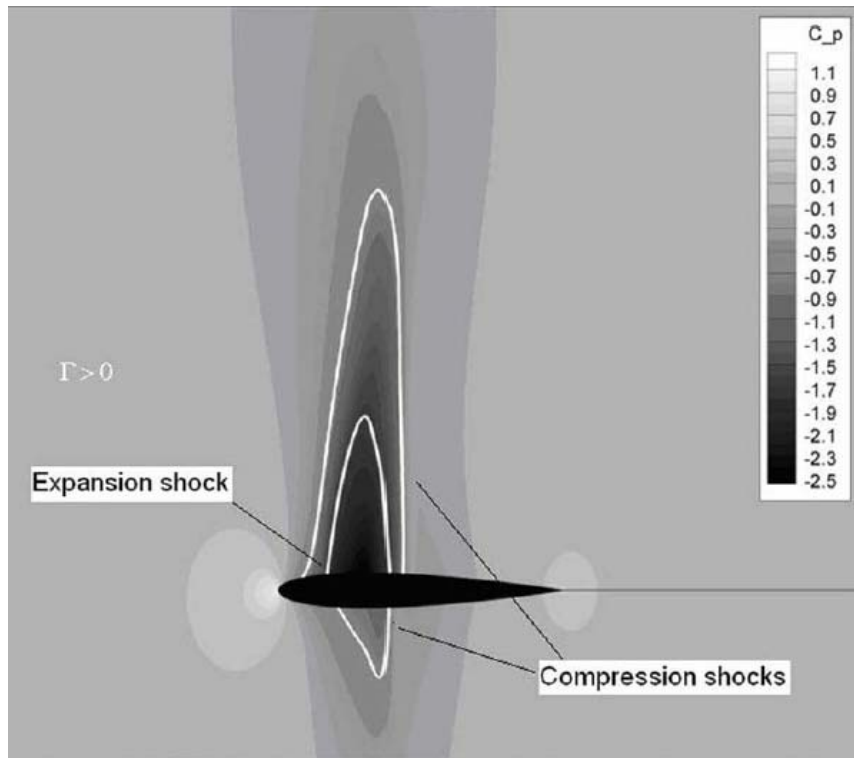


Figure 7: Pressure coefficient contours and $\Gamma = 0$ contours for operating conditions $p_\infty/p_c = 1.03$, $\rho_\infty/\rho_c = 0.877$, $\Gamma_\infty = 1.33$ (low-pressure transonic BZT regime).

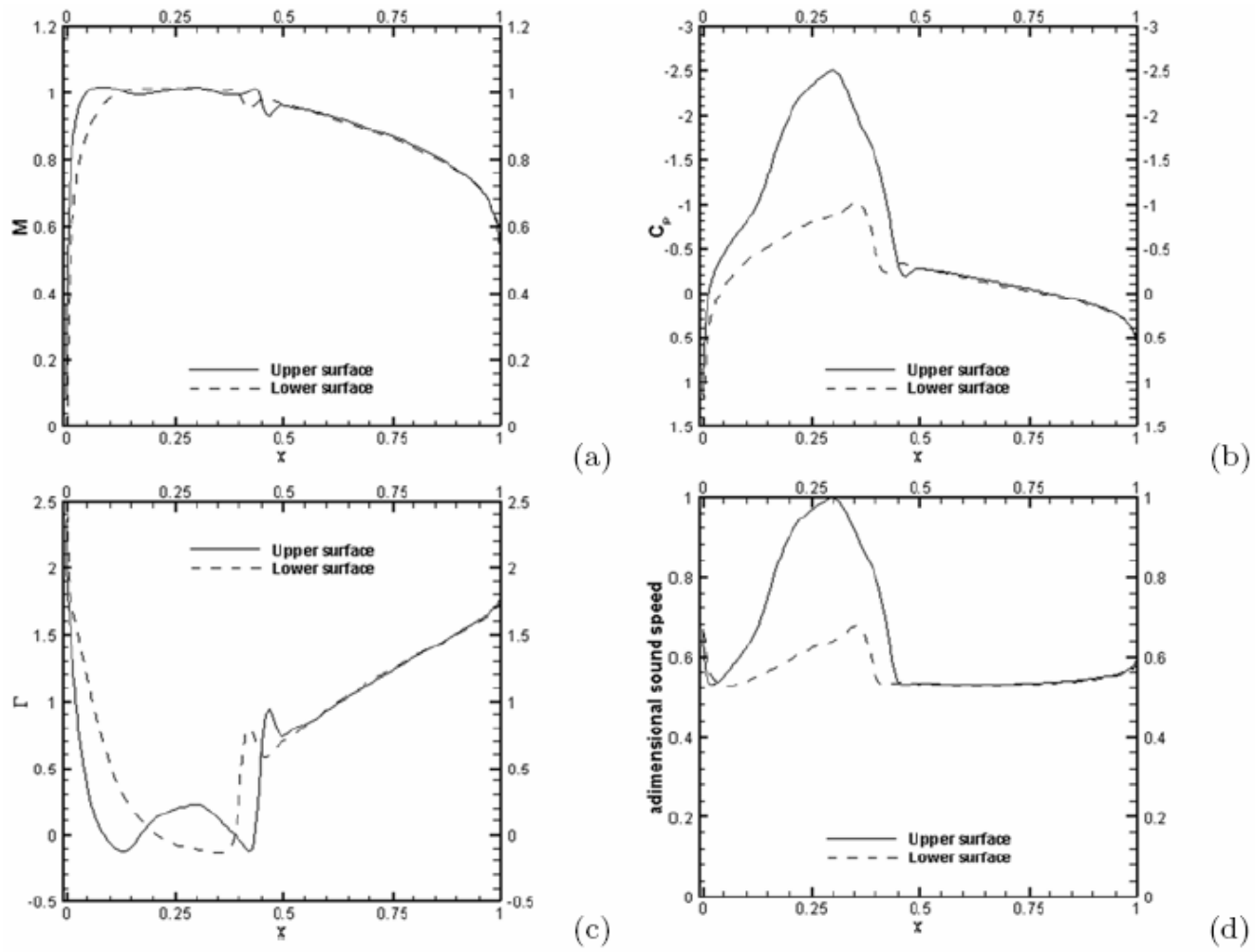


Figure 8: Wall distributions of the Mach number, pressure coefficient, fundamental derivative and sound speed for operating conditions $p_\infty/p_c = 1.03$, $\rho_\infty/\rho_c = 0.877$, $\Gamma_\infty = 1.33$ (low-pressure transonic BZT regime).

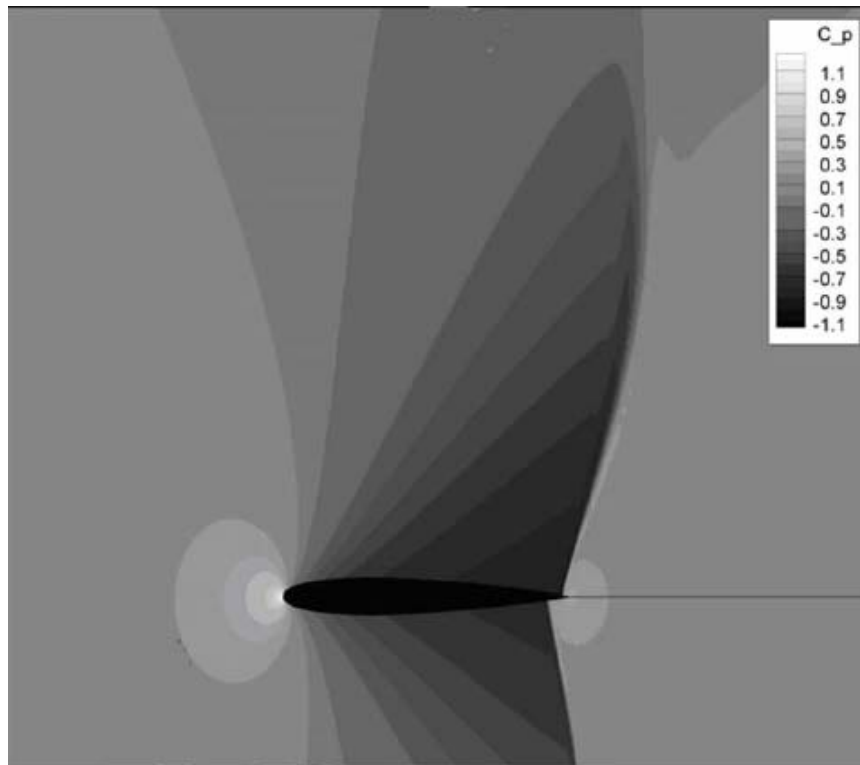


Figure 9: Pressure coefficient contours and $\Gamma = 0$ contours for operating conditions $p_\infty/p_c = 1.17$, $\rho_\infty/\rho_c = 1.11$, $\Gamma_\infty = 1.91$ (high-pressure transonic BZT regime).

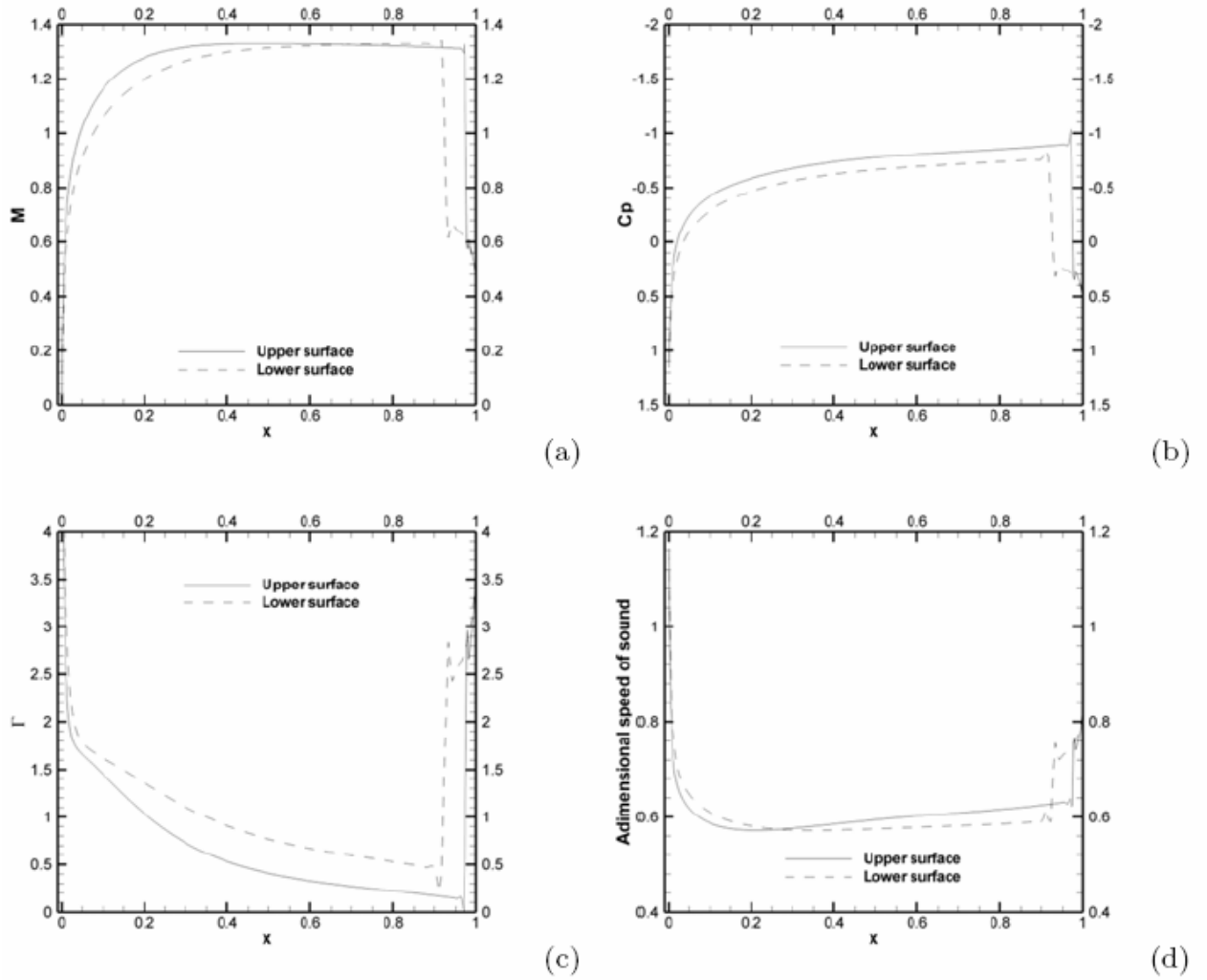


Figure 10: Wall distributions of the Mach number, pressure coefficient, fundamental derivative and sound speed for operating conditions $p_\infty/p_c = 1.17$, $\rho_\infty/\rho_c = 1.11$, $\Gamma_\infty = 1.91$ (high-pressure transonic BZT regime).

4.1.3. Viscous flow behavior

As in previous inviscid flow computations, the working fluid is PP10, flowing at $M_\infty=0.85$, $\alpha = 1^\circ$ and $Re = 9 \times 10^6$. RANS equations are used (see 2.1.1). A parametric study is performed for a series of operation points lying on isentrope S4 (see Figure 2). Solutions are computed using C-grids of 256×64 and 256×128 cells, respectively, with mean $y^+ \approx 5$ on the coarser grid, and $y^+ \approx 1$ on the finer one. In both cases the outer boundary is located about 20 chords away from the airfoil. The reference solution for a diatomic perfect gas flowing at the same conditions is represented in Figure 11 (a). The flow is characterized by strong shock waves at both airfoil surfaces, which interact with the turbulent boundary layer. At the upper surface, an extended post-shock separation bubble

appears. The aerodynamic coefficients are $C_D = 5.28e^{-2}$ and $C_L = -0.012$, the negative sign being due to significant upstream displacement of the upper shock due to flow separation (shock stall). Also note that the drag coefficient is very close (actually, slightly lower) than the value given in 4.1.2 for an inviscid computation. In practice, reduced strength of shock waves due to their interactions with the boundary layer leads to lower wave drag with respect to the inviscid case, and this counterbalances the effect of viscous drag. Wall distributions of the pressure coefficient for viscous and inviscid flow are displayed in Figure 11 (b). The computed values of the aerodynamic coefficients for PP10 at various operating conditions are reported in Figure 12. If the free-stream state is taken close enough to the inversion zone, the flow remains subsonic: no shock waves are formed and flow separation is suppressed. In this regime (subcritical BZT regime), the drag coefficient drops from its PFG value as wave drag disappears, whereas the lift coefficient is considerably higher. For operation points at higher free-stream Γ , in the regime previously christened as "low-pressure transonic BZT", a supersonic region forms. This enhances lift, whereas wave drag remains quite low with respect to the perfect gas case. Two mechanisms contribute to this effect: the first one is of inviscid nature, and is related to the fact that shock waves have jump conditions in the neighbourhood of the transition line, and are therefore less dissipative than normal; on the other hand, such weak shock waves do not cause flow separation, so that pressure drag is further reduced. Further increasing the free-stream pressure (high-pressure transonic BZT regime) leads to increase the strength of shock waves: thus, wave drag grows and the flow finally separates because of shock/boundary layer interactions. As a consequence, both the lift coefficient and the lift-to-drag ratio drop. Figure 11 (c,e,g) shows typical pressure coefficient contours and flow streamlines in the three regimes; wall distributions of the pressure coefficient for inviscid and viscous flow are shown in Figure 11 (d,f,h). Figure 13 compares skin friction distributions for a perfect gas and for PP10 at different operating conditions. Note that the extended separated regions characterizing the perfect gas flow at both airfoil surfaces are absent in dense gas flows insofar as the operating conditions are chosen sufficiently close to the inversion zone. In the subcritical case, for flows at high Reynolds number, the pressure distribution remains essentially similar to the inviscid one, with just only some smoothing of the suction peaks at both surfaces downstream the leading edge. The lift coefficient is slightly below the inviscid value, whereas the lift-to-drag ratio now takes of

course finite, although high values. In the low-pressure transonic BZT regime the differences become more significant. Namely, the suction peak at the airfoil upper surface is dramatically smoothed out because of viscous effects, and the location of the upper shock wave moves upstream because of interactions with the boundary layer: nevertheless, the flow remains attached. Also note that in this regime the skin friction (see Figure 13) significantly grows with chordwise distance up to $x/c \approx 0.25$, due to the very strong favorable pressure gradient acting on the boundary layer. Finally, in the third regime strong shock/boundary layer interactions lead to flow separation at both airfoil surfaces: nonetheless, separation is delayed and separated regions are smaller than in perfect gas flow. In summary, the preceding results suggest that DG effects mainly affect the inviscid flow behavior, whereas the viscous behavior is influenced indirectly according to the distributions of the external pressure and Mach number characterizing flows at different operating conditions. Concerning system efficiency, the use of dense gases working at proper operating conditions has a definitely beneficial effect on system efficiency, not only because of significant reductions in wave drag, but also because losses due to shock/boundary layer interaction are completely suppressed or strongly attenuated.

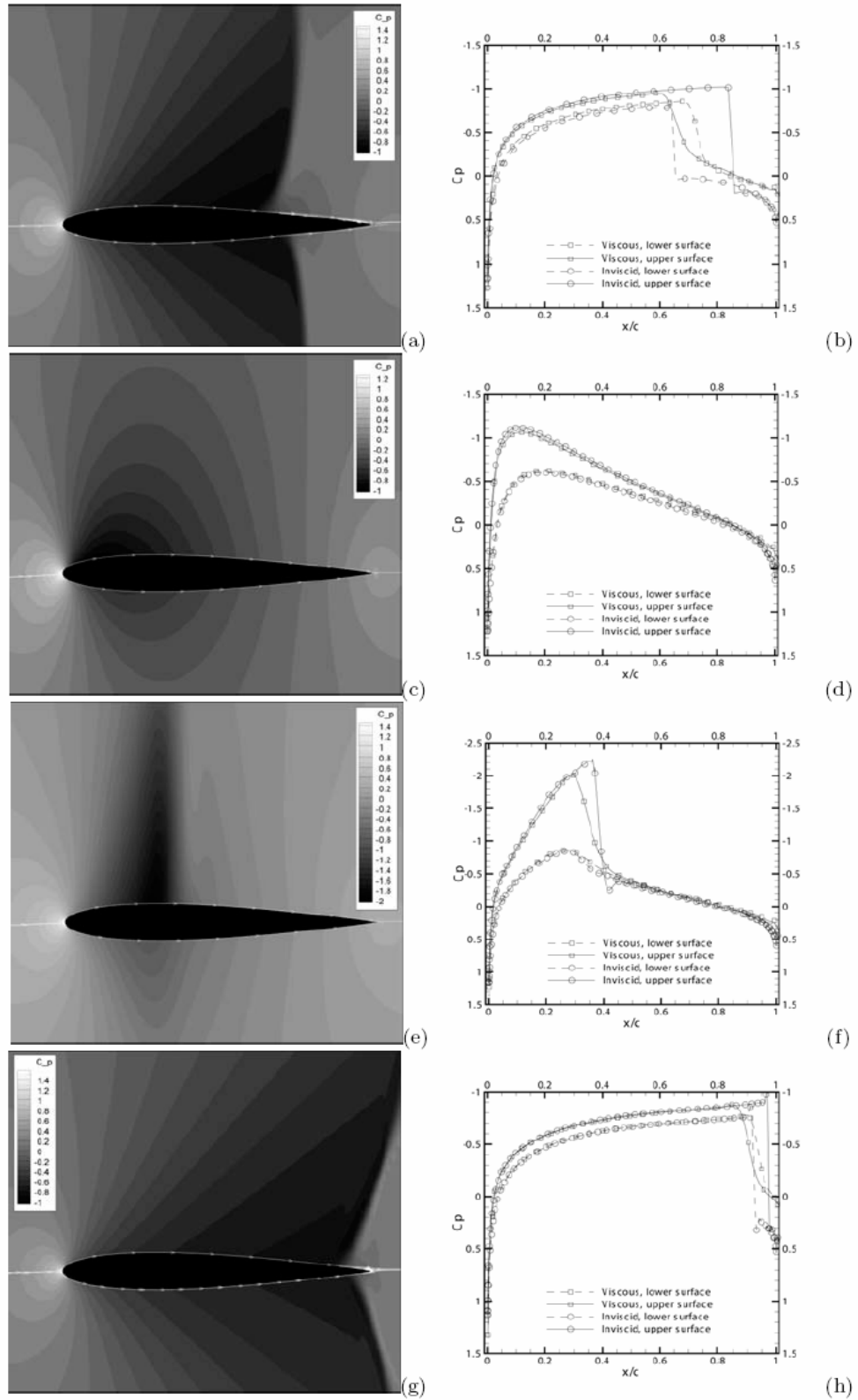
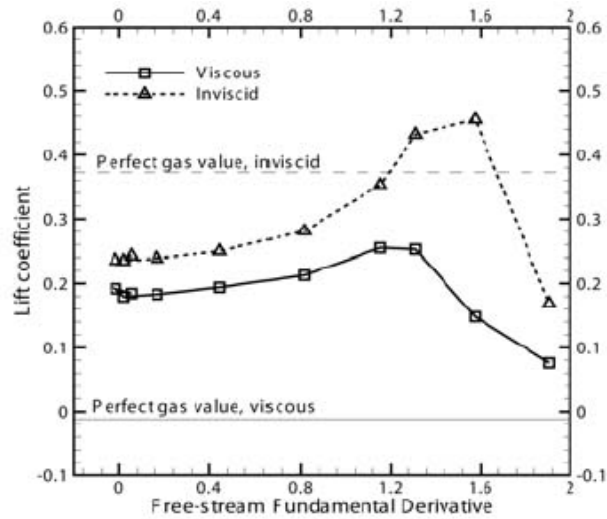
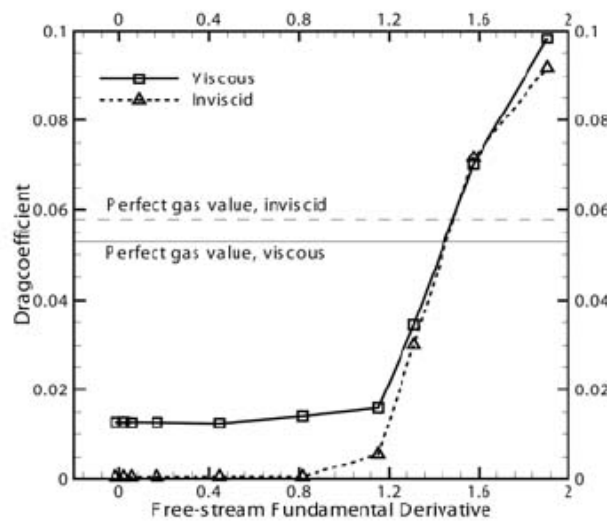


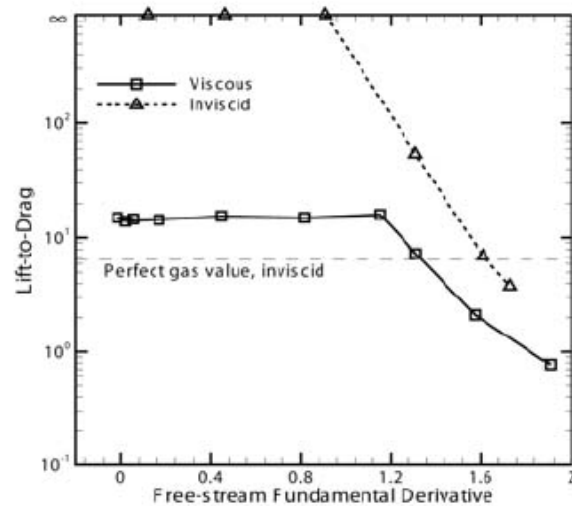
Figure 11: Turbulent flow over the NACA0012 airfoil, $M_\infty = 0.85$, $\alpha = 1^\circ$, $Re = 9 \times 10^6$. Pressure coefficient contours and streamlines (left) and wall pressure coefficient (right) for a perfect gas flow (a,b) and for PP10 at operating conditions $p_\infty/p_c = 1.01$, $\rho_\infty/\rho_c = 0.676$ (c,d), $p_\infty/p_c = 1.08$, $\rho_\infty/\rho_c = 0.850$ (e,f), $p_\infty/p_c = 1.17$, $\rho_\infty/\rho_c = 1.11$ (g,h).



(a)

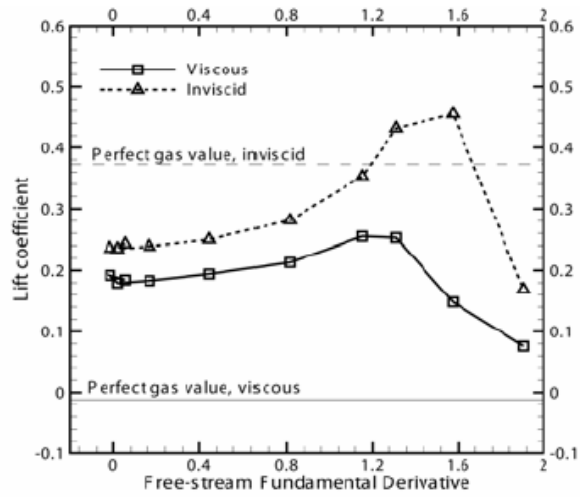


(b)

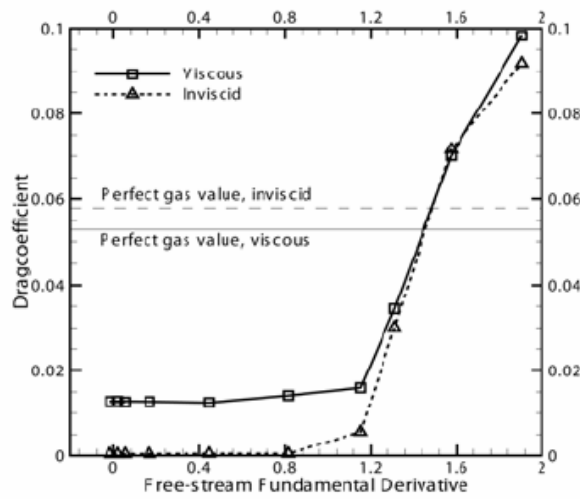


(c)

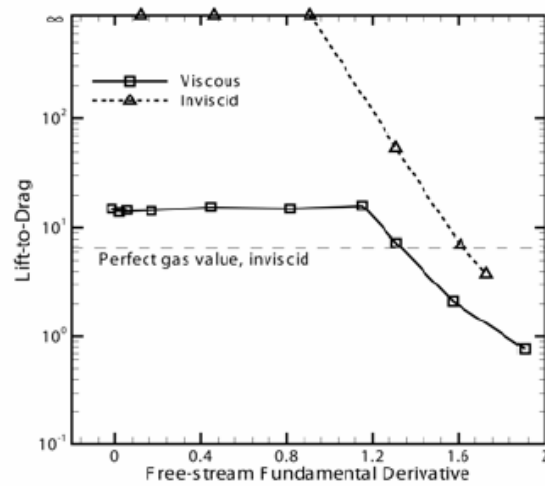
Figure 12: Aerodynamic coefficients versus free-stream fundamental derivative for turbulent flows at $M_\infty = 0.85$, $\alpha = 1^\circ$ and $Re = 9 \times 10^6$ past a NACA0012.



(a)



(b)



(c)

Figure 13: Skin friction for a perfect gas flow and dense gas flows at different operating conditions.

4.2. *Transonic dense gas flow through turbine cascade*

One of the major loss mechanisms in transonic and supersonic turbomachinery is related to the generation of shock waves. The use of a BZT fluid could avoid shock formation and, ideally, allow isentropic turbine expansion. However, simply utilizing a BZT working fluid is not sufficient to maximize the reduction in losses: it is also necessary to operate the turbine cascade at a pressure and temperature near the inversion zone. The inversion zone has a quite limited extent. Therefore, a reduction in the temperature jump between the heater and condenser stages is generally needed in order to operate the turbine cascade in the BZT regime. However, if the temperature jump is taken too small, the overall cycle efficiency and global power output tend to decrease. Then it's necessary to find a trade-off between these two different needs. For this reason a parametric investigation of transonic BZT flows through linear transonic turbine cascades is computed. The von-Karman Institute LS-59 rotor blade cascade (VKI LS-59) is considered. Geometry and experimental data (for air flow) are available in [83]. The cascade has inlet angle equal 30° , and pressure ratio 1.82. The corresponding exit Mach number (for air) is about 1. All computations, concerning both perfect and real gas flows, have been performed at fixed inlet angle and pressure ratio. The computations are performed using C-grids of increasing density, composed by 86×8 , 192×16 and 384×32 cells. The computed convergence order of the numerical solver, based on cascade efficiency, is in the range 2.2–2.5 for all the computed cases; grid convergence index (GCI) on the medium grid is less than 1%. Firstly, perfect diatomic gas flows have been computed. The perfect gas flow is characterized by a weak shock at mid-chord and a trailing edge shock (see Figure 14a). The computed efficiencies (real-to-ideal static enthalpy drop, η) is about 93.8%. Water vapor flows, with reduced inlet thermodynamic conditions $p_1/p_c = 0.9$, $\rho_1/\rho_c = 0.6$, $\Gamma_1 = 1.26$, are characterized by lower efficiency: η equals 87.7% for LS-59. Efficiency losses are related to the formation of strong shocks (upstream Mach number about 1.8) close to the trailing edge (Figure 14b). Then, computations are performed using the BZT fluorocarbon PP10 (pentafluoropropane) as the working fluid. Several computations, corresponding to different thermodynamic inlet conditions are carried out. Figure 15 represents cascade efficiencies for different values of the inlet Fundamental Derivative. This one is changed at constant inlet entropy, and three different entropy values are considered. The first value corresponds to an isentropic line crossing the inversion zone, the second to a line almost tangent to the

transition line, and the last one to a line outside the inversion zone, but within the $\Gamma = 1$ contour. The efficiency tends initially to increase with Γ_1 , reaching an optimum. This roughly corresponds to the lower mean Γ value at the blade wall. In such conditions, average Γ is less than 1 at the wall, and the sound speed increases with dropping pressure. This limits the growth of the Mach number during the flow expansion and reduces shock strength. For higher values of Γ_1 , expansion shock waves appear for the two lower entropy values, and efficiency decreases. This does not happen for the higher entropy value, the flow evolving entirely outside the inversion zone. On the other hand, for such conditions, the average Fundamental Derivative at the wall is below 1, which contributes to weaken or even remove shock waves. Γ quickly drops outside the inversion zone during the flow expansion, and it is necessary to start from higher inlet Γ values in order to have Γ in the right range close to the shock region. Figure 14c present pressure contours for PP10 corresponding to maximum cascade efficiency. Mach number, pressure, and Γ distributions at the wall for the three working fluids are depicted respectively in Figure 16, Figure 17 and Figure 18.

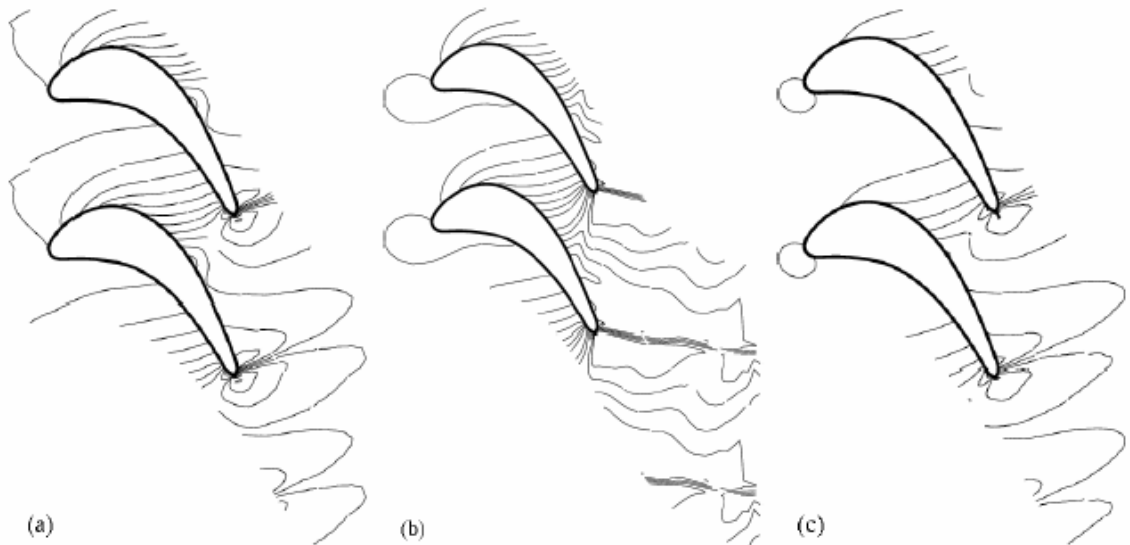


Figure 14: Isobares for a perfect gas (a), steam (b), and PP10 (c). V KI LS-59 cascade.

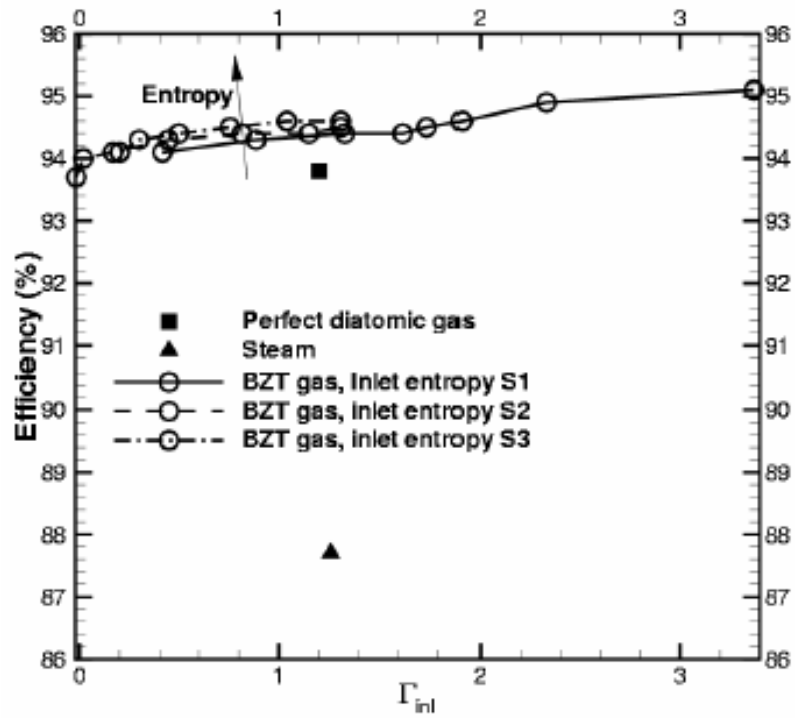


Figure 15: Cascade efficiency versus inlet Fundamental Derivative. Left: SC11 cascade; right: VKI LS-59 cascade.

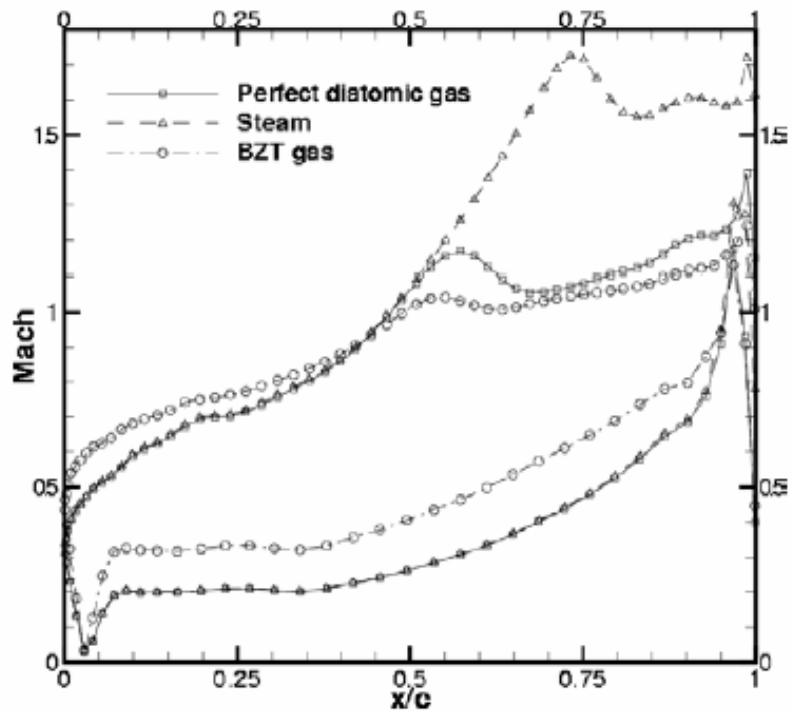


Figure 16: Mach distributions at the wall. VKI LS-59 cascade.

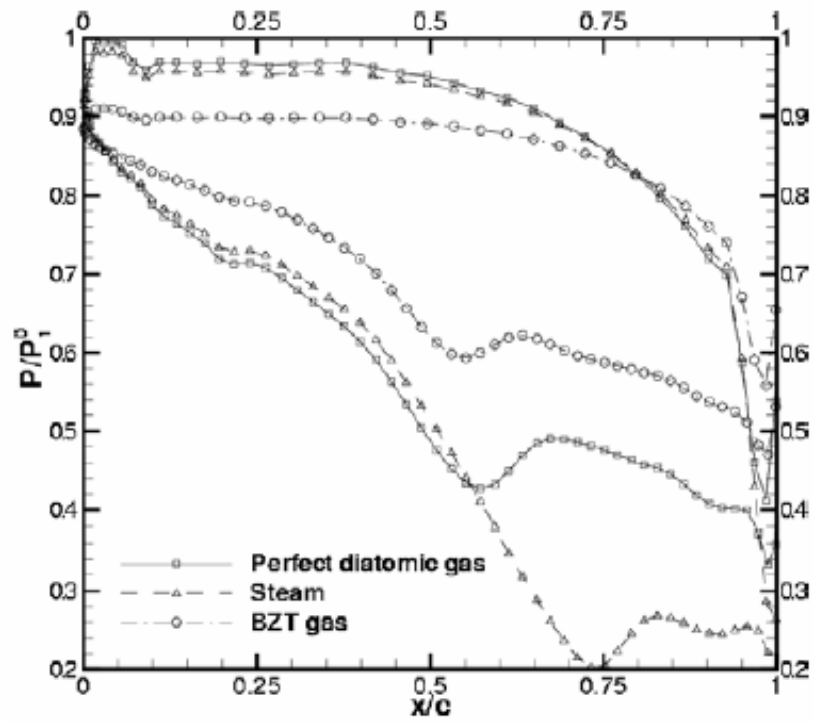


Figure 17: Pressure distributions at the wall. VKI LS-59 cascade.

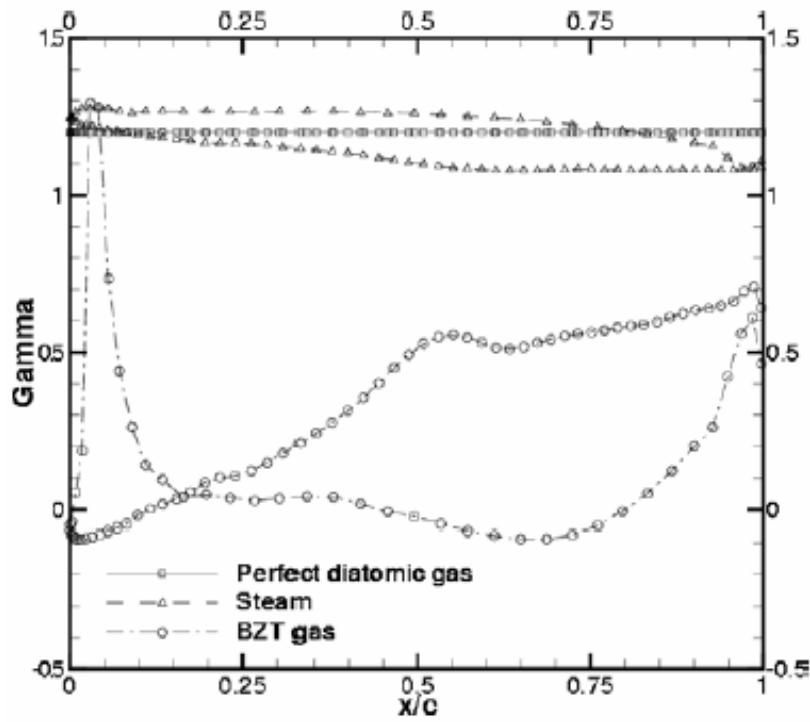


Figure 18: Γ distributions at the wall. VKI LS-59 cascade.

4.3. Shape Optimization of an isolated Airfoil

4.3.1. Inviscid Case

4.3.1.1. Drag Minimization for a symmetric airfoil

The problem is to find the minimal value of the drag coefficient $C_D(\Sigma)$ where Σ denotes an airfoil symmetric shape. In the present case, this shape is constrained to satisfy the following conditions: i) the coordinates of the leading edge and trailing edge normalized by the airfoil chord are respectively $(0, 0)$ and $(1, 0)$, ii) the thickness-to-chord ratio is 12%. The upper airfoil surface is represented by a Bezier curve which is determined in the present study by the coordinates of 8 Bezier points: the fixed leading edge P_0 and trailing edge P_7 , 5 control points $P_{k=2,6}(x_k, y_k)$, regularly spaced along the chord, with the x_k coordinates varying in distinct sub-intervals of $]0,1[$ and a control point $P_1(0, y_1)$, which ensures the upper surface of the profile is tangent to the y-axis at leading edge. A fixed 12% thickness-to-chord ratio is obtained by ad-hoc normalization of the airfoil maximum thickness. The family of airfoil shapes considered in the present study is therefore entirely described by 11 parameters, which vary continuously between prescribed limiting values; the shape representation is such that it allows recovering the NACA0012 airfoil as well as the low-drag airfoil proposed in [25].

The minimization of $C_D(\Sigma)$ is first performed for three different values of the freestream Mach number, successively taken equal to $M_\infty = 0.94, 0.95, 0.98$. In each case, the flow over a population of evolving (half)-airfoil shapes is computed using the UGS on the grid made of 6400 quadrilateral cells with a grid size of $5 \times 10^{-3} c$ at the wall, where c denotes the airfoil chord, 120 points along the airfoil surface and an outer boundary about 10 chords away from the airfoil. VDW equation of state is used with $\gamma = 1.02$ and the freestream thermodynamic conditions normalized by their critical values are taken equal to $p_\infty / p_c = 1.0696$, $\rho_\infty / \rho_c = 0.73502$ in order to allow a comparison with the results obtained in [25]. For each run, the GA-driven population appears to have reached a stabilized optimal (minimal) value of the drag coefficient after the prescribed number of generations, as can be deduced from Figure 19: since the maximum and mean value of the drag coefficient in the final population of airfoil shapes are almost the same in each case,

this means the algorithm has converged to a population of almost identical geometries. The optimized airfoil shape for each freestream Mach number is plotted in Figure 20 along with the NACA0012 airfoil, the low-drag airfoil and the sonic arc taken from [25]. It is noteworthy to observe the optimal shape for $M_\infty = 0.94$ (indicated in the following as OA094) turns out to be almost superimposed with Rusak and Wang's low-drag airfoil; consequently, this latter shape will be retained in the following analysis as the one producing minimal drag at $M_\infty = 0.94$. Reducing the drag for higher values of the freestream Mach number leads to airfoil shapes that are getting closer to the limiting case of the sonic arc, as far as allowed by the airfoil shape representation retained in this study. Since, ideally, a consistent drag reduction is expected for the whole range of freestream Mach numbers, the wave drag produced by these modified shapes, which are optimized for a specific value of M_∞ , are next checked for different values of M_∞ , taken in the interval $[0.9, 0.995]$; this *a posteriori* analysis is performed using both the SGS and the UGS for cross-validation purpose. The computed evolutions of the drag coefficient with increasing values of the freestream Mach number are plotted in Figure 21: the optimal shape at $M_\infty = 0.95$ (OA095) allows to obtain lower drag levels than the OA094 airfoil for the whole range of freestream Mach number, both shapes being far superior to the original NACA0012 airfoil; on the contrary, the optimal shape at $M_\infty = 0.98$ (OA098) displays a very poor performance for lower values of the freestream Mach number. All of the drag curves fall within the envelope corresponding to the sonic arc performance. The MOGA strategy offers the possibility of looking for an airfoil that would simultaneously minimize the drag coefficient at $M_\infty = 0.95$ and $M_\infty = 0.98$. Such an airfoil should hopefully provide a good drag performance over a larger range of free-stream Mach numbers. To obtain such an airfoil, a bi-objective optimization run is computed, using the same GA parameters as in the previous mono-objective runs; among the set of optimal shapes provided by the MOGA, a typical trade-off solution has been retained (OAB), which is plotted in Figure 20. The associated drag evolution is also displayed in Figure 21: the OAB airfoil turns to yield lower drag levels than the previous single operation point optima for the whole range of freestream Mach number, because its geometry is actually closer to that of the sonic arc. The wall pressure and Mach number distributions at $M_\infty = 0.95$ and $M_\infty = 0.98$ are plotted in Figure 22 for the various geometries under study. At

$M_\infty = 0.95$, all of the airfoils except the sonic arc are beyond their respective critical Mach number; in fact, the NACA0012, Rusak-Wang and OA098 airfoils are also beyond the drag divergence Mach number, whereas the OA095 and OAB airfoils still yield isentropic flows. Note the OA098 airfoil displays a shock in the leading edge region down to $M_\infty = 0.90$. At $M_\infty = 0.98$, all of the airfoils, including the sonic arc, are subjected to the transonic drag rise: the OA095 and OAB wall distributions are similar to the ones associated with the sonic arc up to 70% of chord, where the shapes of the three airfoils start to strongly differ (see Figure 20).

A similar optimization process has been carried out for a flow of perfect gas with $\gamma = 1.4$ as well as a dense gas flow with $p_\infty / p_c = 1.0696$, $\rho_\infty / \rho_c = 0.73502$ modeled using the more realistic MAH equation of state. While the VDW equation of state was retained up to now in order to allow a comparison with the results obtained in [25], the analysis performed with MAH and PFG indicates the improvement in terms of drag reduction that can be expected (for inviscid flows) when switching from air to PP10 with airfoil shapes optimized according to the nature of the fluid. Various optimization strategies were applied to the PFG case: single-point drag minimization for different free-stream Mach numbers in the transonic drag rise region, simultaneous minimization of drag for two values of M_∞ above the drag divergence Mach number of the baseline NACA0012 airfoil. The overall best performance, for the shape representation described at the start of this section, is plotted in Figure 23 : the optimal airfoil, denoted OA083, is specifically targeted to achieve minimal (zero) drag at $M_\infty = 0.83$ so that it suffers from a slight increase in wave drag at $M_\infty = 0.82$ due to the appearance of a weak shockwave. For the MAH case, the best performance was obtained with an airfoil (OAB) designed to minimize drag at $M_\infty = 0.925$ and $M_\infty = 0.95$. As shown in Figure 23, the optimal airfoil increases the drag divergence number from $M_\infty = 0.91$ for the NACA0012 airfoil up to almost $M_\infty = 0.93$. Figure 24 displays the strong discontinuities produced by the baseline NACA0012 airfoil in the drag divergence region associated with each gas model (PFG, VDW and MAH) and presents the pressure contours of the corresponding shock-free airfoils (just before the drag divergence Mach number is attained).

As shown in the above, the optimization procedure leads to minimal drag airfoils with increasingly better performance when their shape tends to become closer to the sonic arc, the better is the airfoil performance. Unfortunately, the sonic arc shape is not optimal if the flow of a viscous fluid is considered, because of its blunt trailing edge that can lead to flow separation. For this reason, Rusak's low-drag airfoil [25] is essentially obtained by modifying the trailing edge of the optimal sonic arc shape, replaced by a sharp tail similar to that of the NACA0012 airfoil. In order to check the viscous performance of the optimal shapes derived from the present MOGA optimization procedure, a numerical investigation of viscous turbulent flows past such optimal airfoils is undertaken. In particular viscous flows past the OA095 and OAB airfoils, which have been found to provide the best inviscid performance in the previous study of Rusak's optimization problem, are computed and compared with results obtained for the reference NACA0012 and Rusak-Wang airfoils in the same conditions. The computations are performed using half-O grids of 100x64 cells, with a mean first cell height of about 6×10^{-5} , representing a reasonable tradeoff between accuracy and computational cost. The gas thermodynamic response is modeled using MAH equation of state. The thermodynamic freestream conditions are taken equal to $p_\infty / p_c = 0.985$, $\rho_\infty / \rho_c = 0.622$, the Mach number is varied in the interval $[0.85, 0.99]$ and the flow Reynolds number based on free-stream conditions and the airfoil chord is 10^7 . The flow past the NACA0012 and Rusak-Wang airfoils is attached for freestream values of the Mach number less than about 0.97. In both cases, at $M_\infty = 0.98$ the flow becomes separated close to the trailing edge; the flow at $M_\infty = 0.99$ is massively separated. Conversely, the flow field around the OAB airfoil already exhibits a recirculation region close to the trailing edge for the lowest values of M_∞ . In fact, this airfoil shape is the closest to the sonic arc, which greatly enhances its inviscid performance, but represents a serious drawback for viscous flows. An intermediate behavior is found for OA095 since the flow becomes separated at about $M_\infty = 0.95$ for that shape. Figure 25 shows the flow fields (Mach number contours and streamlines) for the four airfoils, at $M_\infty = 0.96$: flow past OAB is characterized by significant separation at the trailing edge, whereas flow past OA095 is just slightly separated and flows past the NACA0012 and Rusak-Wang airfoils are completely attached. Figure 26 shows the drag coefficient versus the Mach number for the four airfoils analyzed. For the lowest values of M_∞ , the thicker trailing edges of

OA095 and OAB lead to poorer performances in comparison with the more slender NACA0012 and Rusak-Wang airfoils. On the other hand, for higher values of M_∞ , the flow becomes supercritical and wave drag appears: in these conditions, the adapted design of the OA095 and OAB airfoils becomes advantageous, and both airfoils represent a true improvement over the two reference shapes. Globally, the best overall performance over the explored range of Mach numbers is offered by the OA095 airfoil.

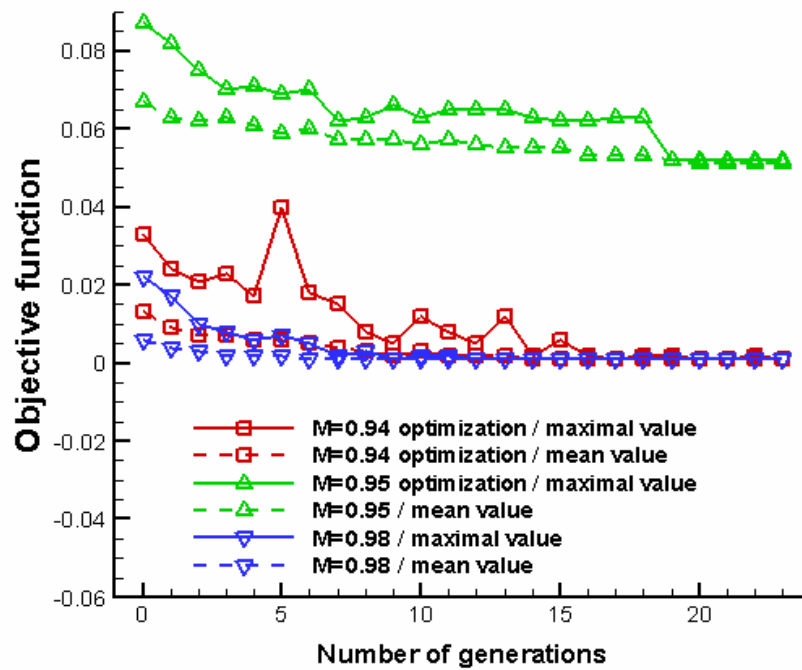


Figure 19: Evolution of the maximal and mean value of the drag coefficient for the computed population as function of the number of generations. Mono-objective (single operation point) optimization runs for different values of the freestream Mach number.

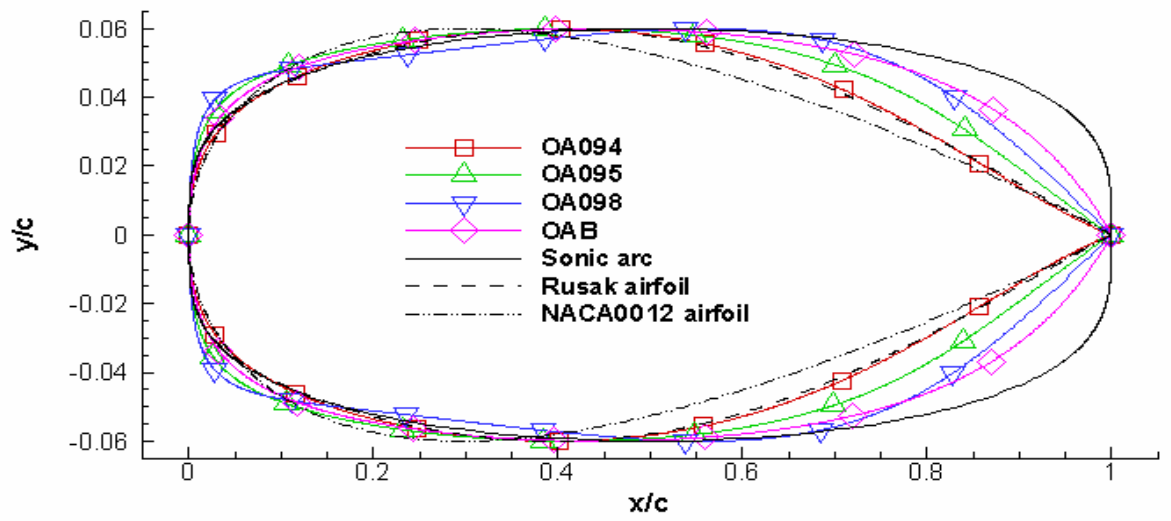
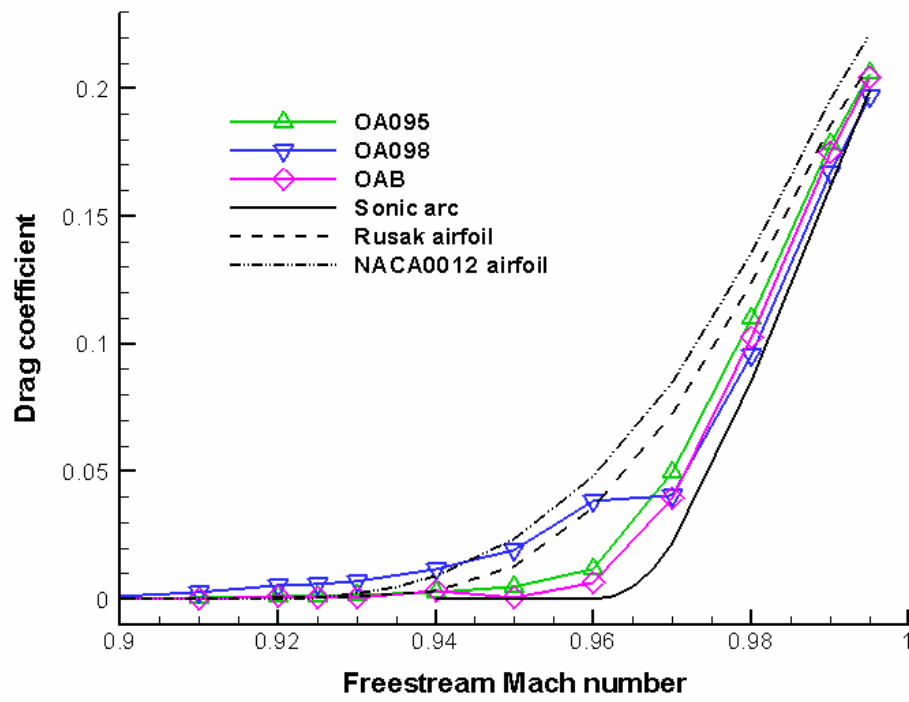
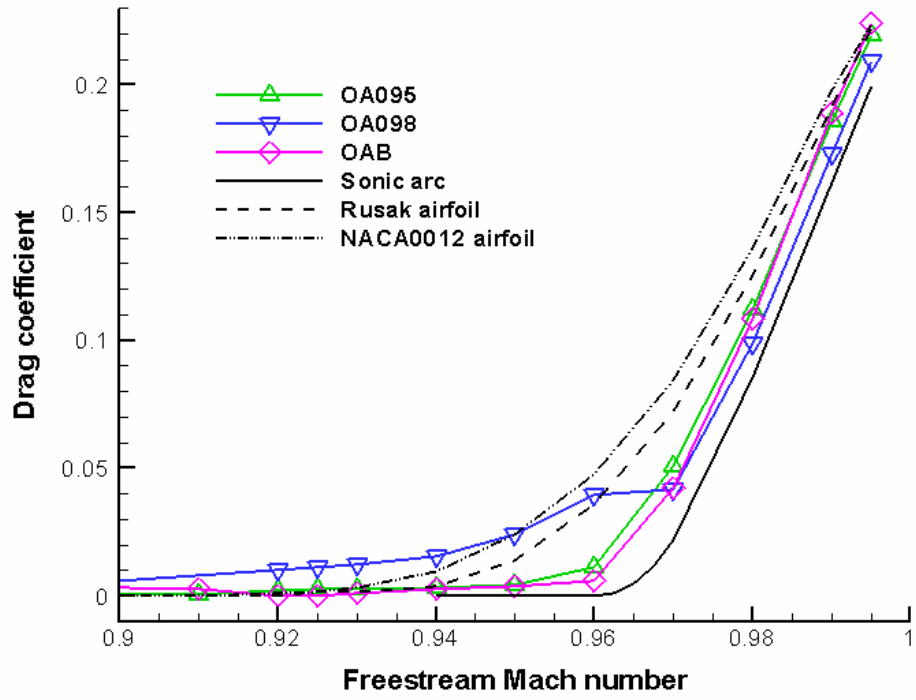


Figure 20: Geometry of optimized airfoils, sonic arc, Rusak low-drag airfoil and NACA0012 airfoil.

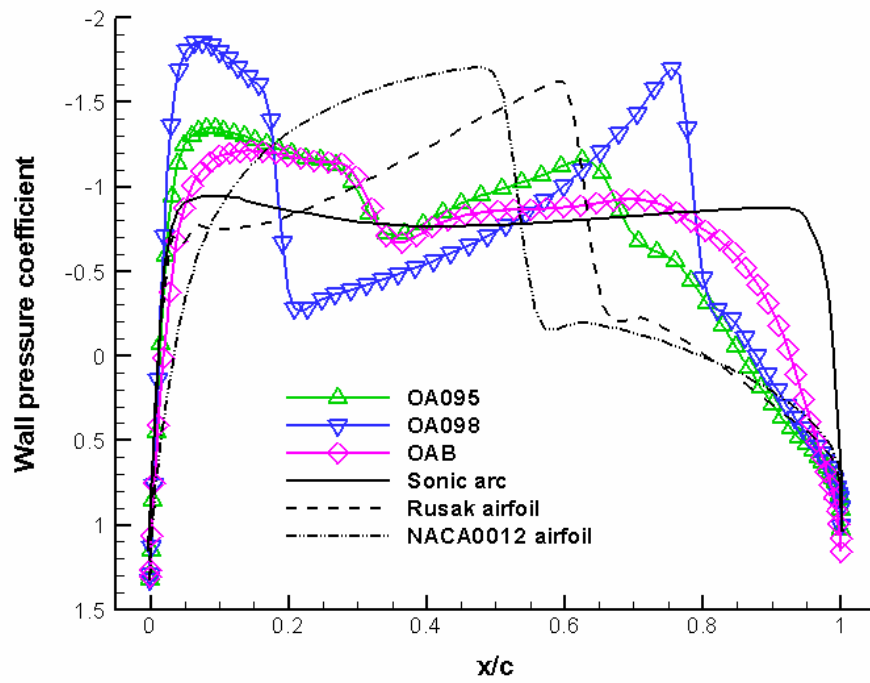


(a)

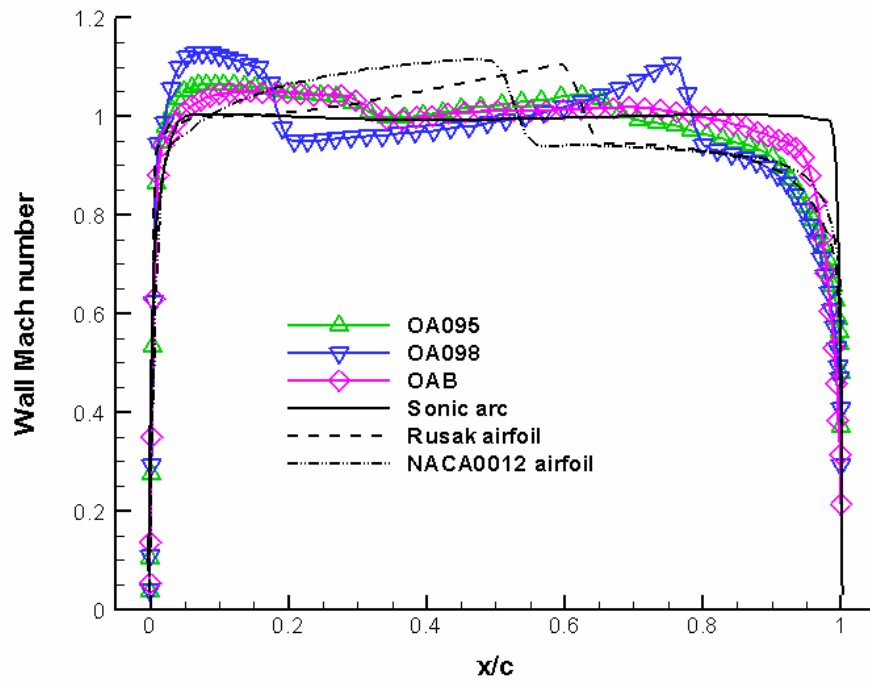


(b)

Figure 21: Pressure drag versus free-stream Mach number for different airfoil shapes. Results obtained using UGS (a) and SGS (b).

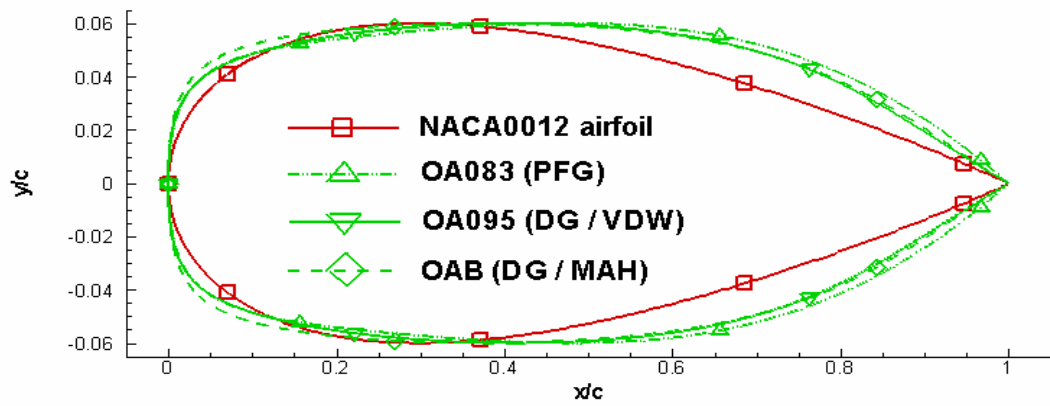


(a)

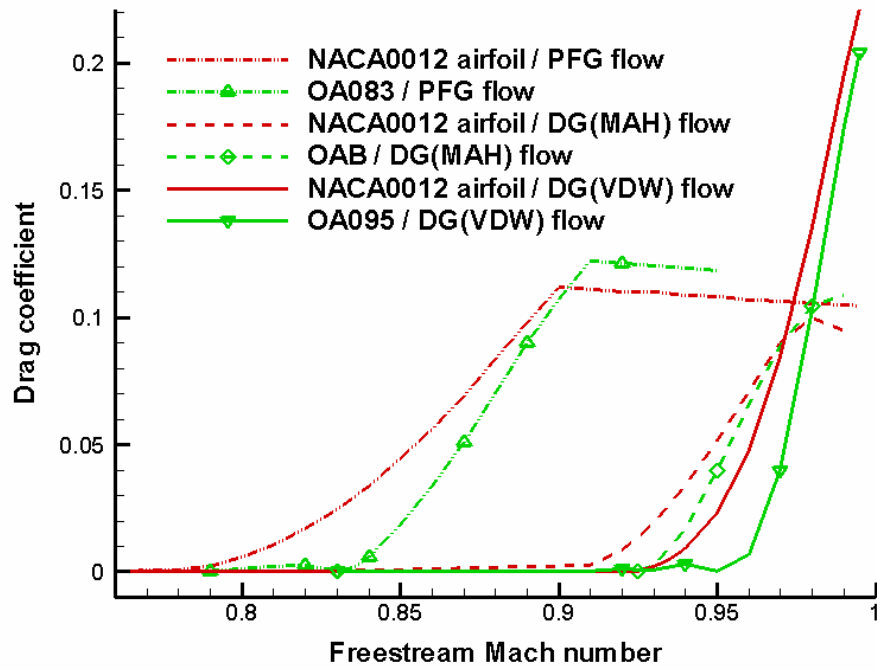


(b)

Figure 22: Wall pressure (a) and Mach number (b) distributions for optimized airfoils, sonic arc, Rusak airfoil and NACA0012 airfoil at $M=0.95$. SGS results.

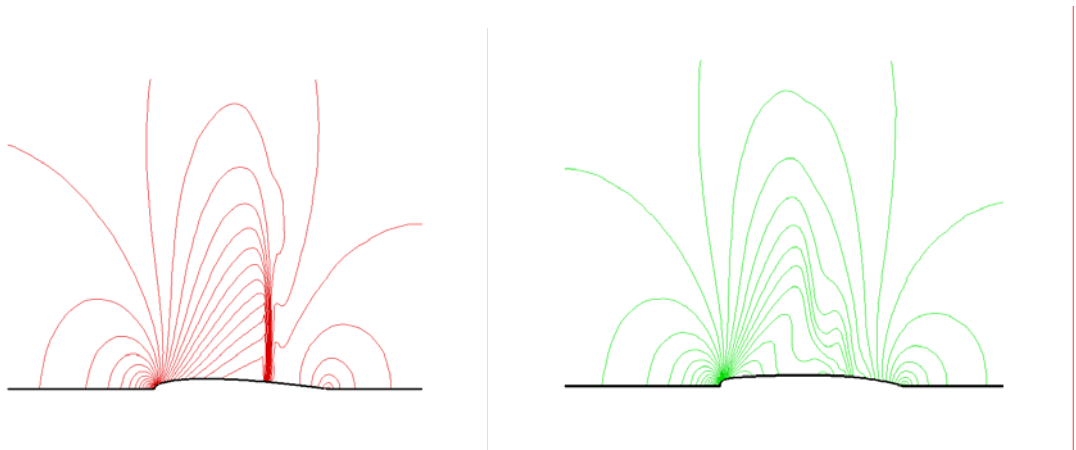


(a)

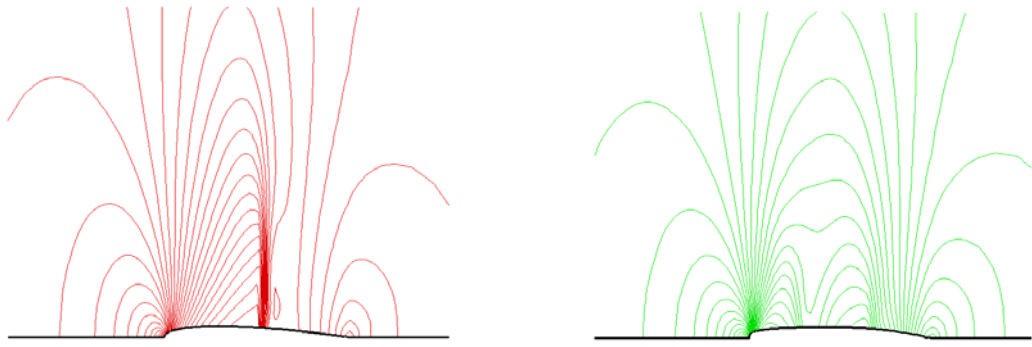


(b)

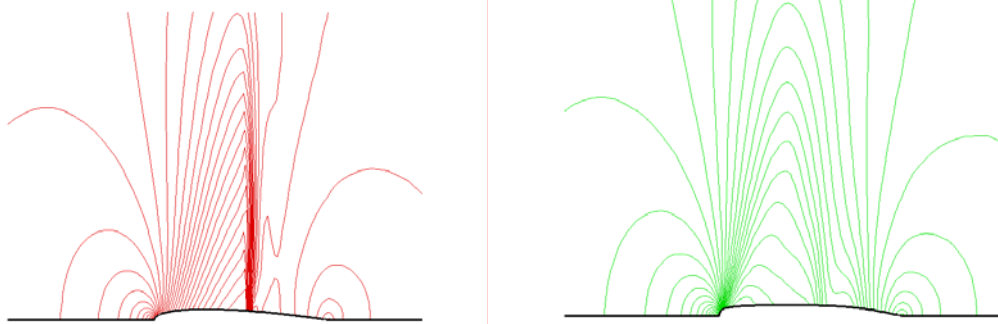
Figure 23: (a) optimal geometries for the drag minimization problem solved in the case of a PFG flow and a DG flow with VDW or MAH EOS. (b) Associated pressure drag as a function of the freestream Mach number.



(a) Perfect gas flow. $M_\infty = 0.83$.



(b) Dense gas flow, VDW equation of state. $M_\infty = 0.95$.



(c) Dense gas flow, MAH equation of state. $M_\infty = 0.925$.

Figure 24: Pressure contours around the baseline NACA0012 airfoil and optimal airfoils for perfect and dense gas flows with freestream conditions leading to an equivalent amount of wave drag for the baseline airfoil.

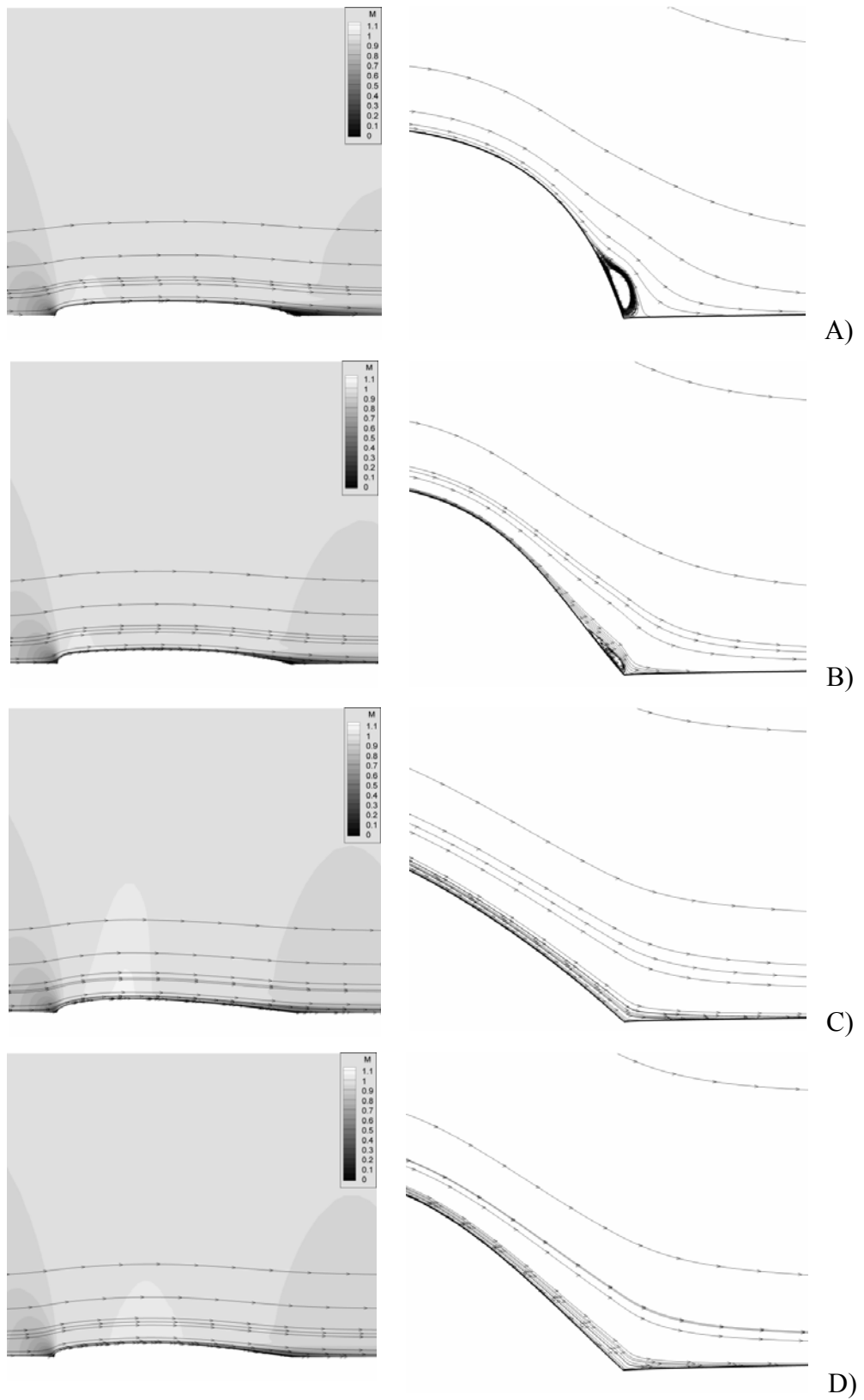


Figure 25: Mach number contours and streamlines for turbulent flows past four airfoils (right); left: close-up of the streamlines at the trailing edge (grid aspect ratio not preserved). A) OAB; B) OA095; C) NACA0012; D) Rusak-Wang. $M_\infty = 0.96$, $Re \cong 10^7$.

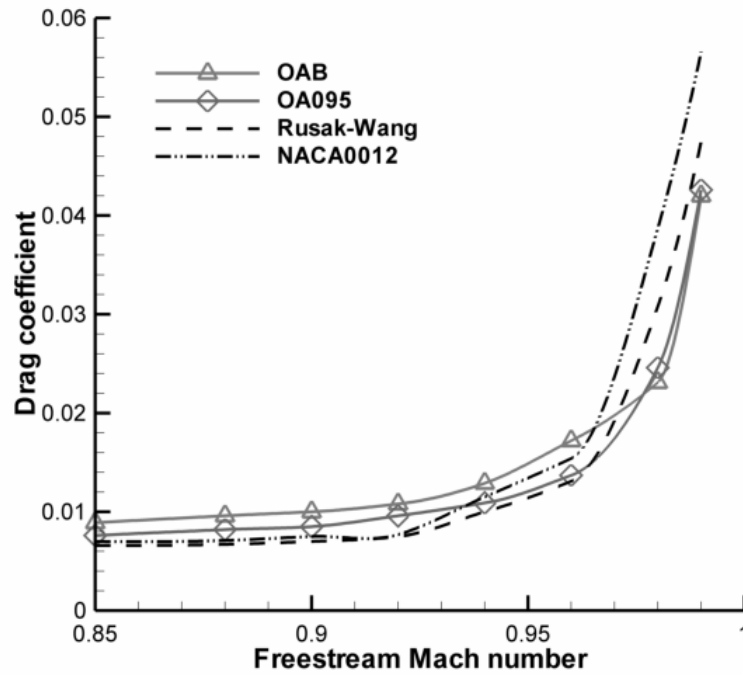


Figure 26: Viscous performance of minimal-drag airfoils stemming from inviscid optimization.

4.3.1.2. Performance Optimization for a Lifting Airfoil

The shape representation retained for the complete airfoil derives from that adopted in the study of a half profile. The upper part of the airfoil is represented as described in the previous subsection; the lower part is described in a similar way using a Bezier curve based on 8 control points, including the fixed leading and trailing edges, as well as a point on the negative part of the y-axis in order to ensure the airfoil leading edge is tangent to the y-axis. Once the whole airfoil is generated, the thickness distribution is normalized to yield a 12% thickness-to-chord ratio.

The computation of the dense gas flow at $M_\infty = 0.85$ and $\alpha = 1^\circ$ is considered. The dense gas is modeled using MAH equation of state with coefficients corresponding to PP10. The UGS is used to simulated. Two operation points of interest are selected : the freestream thermodynamic conditions ($p_\infty / p_c = 1.008$, $\rho_\infty / \rho_c = 0.676$, $\Gamma_\infty = 0.168$) denoted OP#1, yield significant BZT effects, whereas the choice ($p_\infty / p_c = 1.079$, $\rho_\infty / \rho_c = 0.882$, $\Gamma_\infty = 1.312$), denoted OP#2, leads to higher values of the fundamental derivative throughout the flow, and thus to much reduced BZT effects. By considering a flow past a

NACA0012 airfoil the dense gas flow for OP#1 remains subcritical with a computed lift coefficient $C_L = 0.2265$ for the SGS and a drag coefficient very close to zero. For OP#2, the dense gas flow becomes supercritical with $C_L = 0.4467$, $C_D = 0.0510$. Note the perfect gas flow is such that $C_L = 0.373$, $C_D = 0.0574$; thus, though the dense gas allows to achieve extremely high lift-to-drag ratio in the subcritical OP#1 conditions, the corresponding lift level remains below that of the perfect gas flow whereas the dense gas aerodynamic performance in the supercritical OP#2 conditions tends to come close to that of the perfect gas. The possibility to simultaneously achieve higher lift values for operating conditions where BZT effects are important and to improve the lift-to-drag ratio when these effects become less significant is considered. Then, the lift coefficient in the OP#1 conditions, $C_L(\Sigma; OP\#1)$, and the lift-to-drag ratio in the OP#2 conditions, $C_L / C_D(\Sigma; OP\#2)$, are simultaneously maximized by applying the MOGA with a population of 36 individuals during 24 generations. A partial view of the computed individuals is shown in Figure 27 along with the set of non-dominated solutions eventually obtained: it clearly illustrates that the initial NACA0012 airfoil aerodynamic performances in dense gas flow have been substantially improved through the optimization process. In particular, almost all of the Pareto-optimal individuals have now a lift coefficient at OP#1 and a lift-to-drag ratio at OP#2 greater than the lift coefficient and the lift-to-drag ratio generated by the NACA0012 airfoil for a perfect gas flow. In order to draw a fair comparison with perfect gas flow, a shape optimization is also performed for the perfect gas ($\gamma=1.4$) flow at $M_\infty = 0.85$ and $\alpha = 1^\circ$ of incidence over an airfoil of 12% thickness-to-chord ratio with a geometry based on the Bezier curves previously described; with unique thermodynamic conditions for this PFG flow, the problem is expressed as the simultaneous maximization of the lift and minimization of the drag. The optimal solutions obtained are plotted in Figure 27 in the lift / lift-to-drag plane: they remain well below the optimal solutions associated with the DG flow. Figure 28 displays one of the optimal solution selected along the final Pareto front: this particular shape, hereafter denoted OAB to recall it results from a bi-objective optimization process, has been retained because, among the set of non-dominated solutions, it displays the thickness distribution in the trailing edge region that is the most likely to preserve good aerodynamic performances in the viscous case. The wall pressure and Mach number distributions computed on the

NACA0012 airfoil and OAB for subcritical (OP#1) and supercritical (OP#2) conditions are plotted in Figure 29 and in Figure 30. For subcritical conditions, both airfoils display zero drag but OAB yields a much higher lift coefficient ($C_L = 0.794$) than the NACA0012 airfoil ($C_L = 0.226$) thanks to a much stronger expansion of the flow around the upper leading edge. For supercritical conditions, the OAB yields more than twice the drag of the NACA0012 airfoil ($C_D = 0.116$ versus $C_D = 0.051$) but also generates almost three times the lift of the NACA0012 airfoil ($C_L = 1.3$ versus $C_L = 0.45$) so that its lift-to-drag ratio of 11.2 is indeed better than the value of 8.8 obtained with the NACA0012 airfoil, as expected from the optimization process. An overview of the optimized airfoil performance is provided in Figure 31 where the lift coefficient and the lift-to-drag ratio are plotted for dense gas flow around both the baseline NACA002 airfoil and the optimized airfoil for different free-stream thermodynamic conditions covering the subcritical as well as the low- and high-pressure transonic BZT flow regimes: as expected from the two-point optimization the modified airfoil systematically ensures a level of lift for dense gas flow in subcritical regime at least equivalent to the highest level achievable with a PFG flow while preserving a high lift-to-drag ratio in the subcritical and low-pressure supercritical regime. The airfoil viscous performance has also been checked for this lifting case, as already seen in the previous subsection. The viscous computations have been performed on an O-grid of 200x64 cells, with a mean first cell height in the direction normal to the wall equal to about $6 \times 10^{-5} c$, and on a finer grid of 200x128 cells, with a mean first cell height equal $5 \times 10^{-6} c$. The outer boundary is located about 12 chords away from the airfoil. The freestream conditions are successively taken equal to OP#1 and OP#2. The corresponding fine-grid values of the lift and drag coefficients, and of the lift-to-drag ratio are reported in Table 1. For comparison, viscous solutions for dense gas flows past the NACA0012 airfoils at the same thermodynamic conditions are also presented. The optimized airfoil conserves a superior aerodynamic performance over the NACA0012 even when viscous effects are relevant. It should be noticed however that the viscous performance of both dense and perfect gas flows significantly differs from inviscid results. At flow conditions OP#1, the flow-field is entirely subsonic, and boundary layer is attached, both for the NACA0012 and for the OAB airfoil. However, because of the high total pressure of the incoming stream, the flow strongly accelerates downstream of the stagnation point, and a deep suction peak appears at the upper surface downstream of the leading edge. In fact, the

strong suction exerted on the upper surface is the main reason of the dramatic improvement of the lift over the perfect gas for an inviscid flow. The other side of the coin is that, when viscous effects are taken into account, the very strong adverse pressure gradient downstream of the suction peak leads to a significant growth of the boundary layer and to enhanced friction in the leading edge region. Consequently, the peak itself is noticeably smoothed out, and the airfoil lift drops below the inviscid value. Figure 32 shows the wall pressure coefficient and skin friction distribution for this case. For flow conditions OP#2, the relevant differences with respect to inviscid flow are due to strong shock/boundary layer interactions, leading to post-shock separation and reattachment, both in the flow over the NACA0012, and over OAB, with subsequent blow up of the subsonic part of the boundary layer (see wall pressure and skin friction distributions on Figure 33). Paradoxically, in this case the shock/boundary layer interaction leads to a reduction both in lift and drag coefficients with respect to inviscid flow, due to considerably decreased strength of shock waves. For completeness, the PFG viscous aerodynamic performance of the NACA0012 is also included in Table 1: in the PFG case, the lift coefficient is negative, because of massive post-shock separation at the upper surface, caused by severe shock/boundary layer interaction.

Case	C_D	C_L	C_L/C_D
Optimized airfoil, condition OP#1	1.416×10^{-2}	0.6077	42.92
Optimized airfoil, condition OP#2	6.648×10^{-2}	0.9693	14.58
NACA0012, condition OP#1	1.275×10^{-2}	0.1833	14.38
NACA0012, condition OP#2	3.448×10^{-2}	0.2529	7.335
NACA0012, perfect gas flow	5.456×10^{-2}	-4.086×10^{-2}	-0.7489

Table 1: Aerodynamic performance of viscous flows over the NACA0012 airfoil and an optimized airfoil stemming from the MOGA strategy.

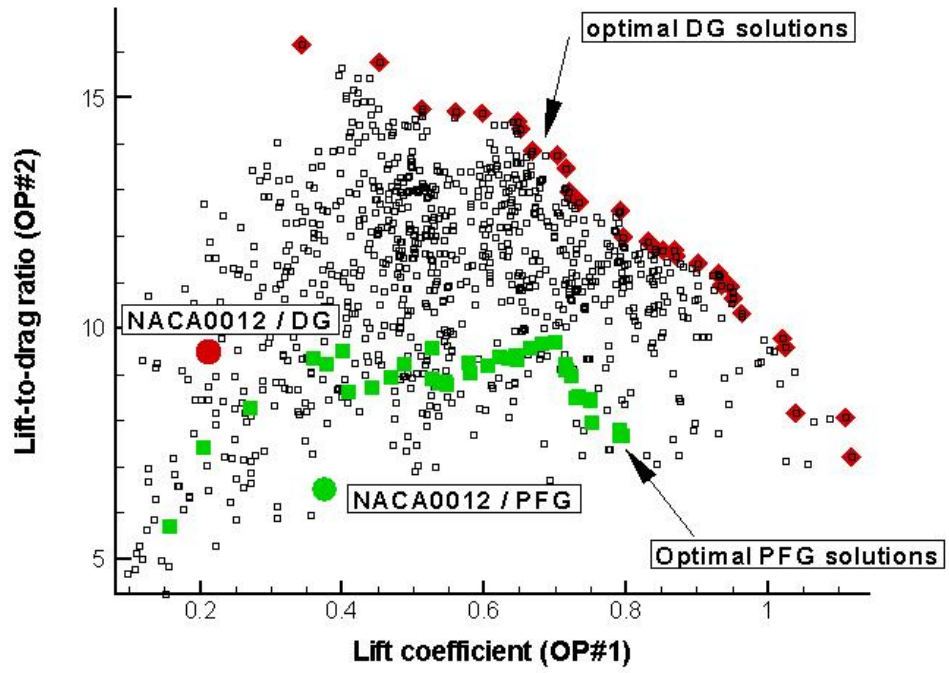


Figure 27: Lifting airfoil 2-point performance optimization. Overview of the computed solutions during the genetic evolution process.

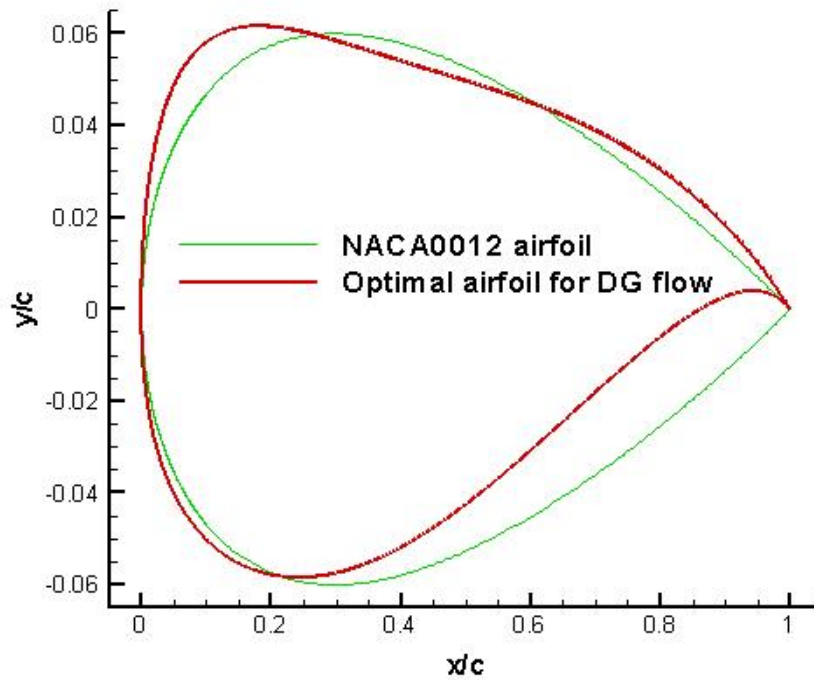
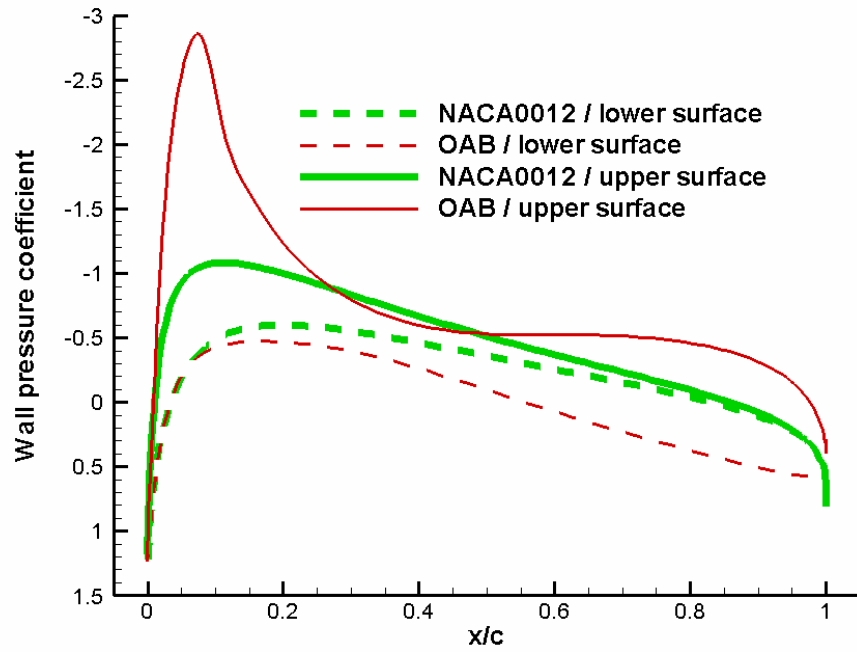
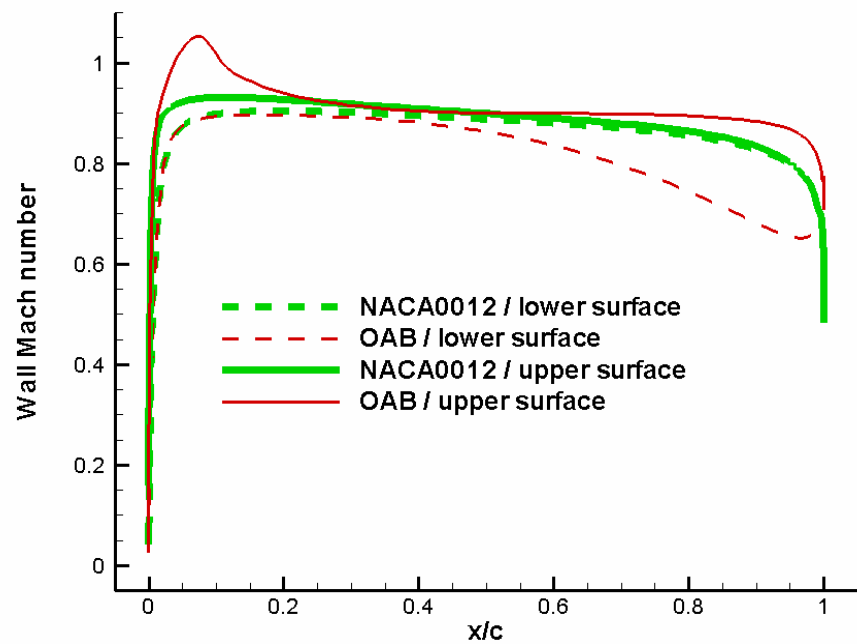


Figure 28: Lifting airfoil 2-point performance optimization. Typical optimal shape.

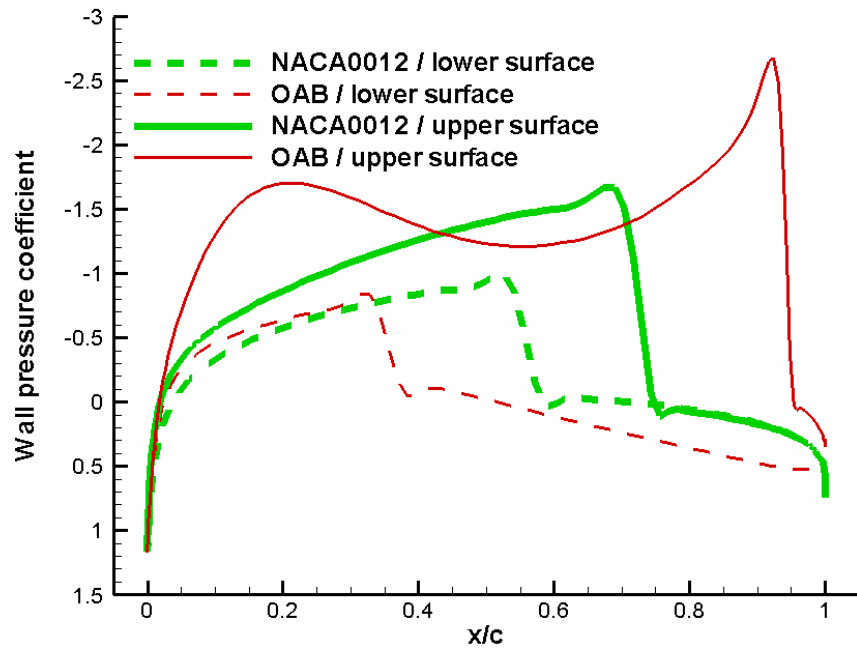


(a)

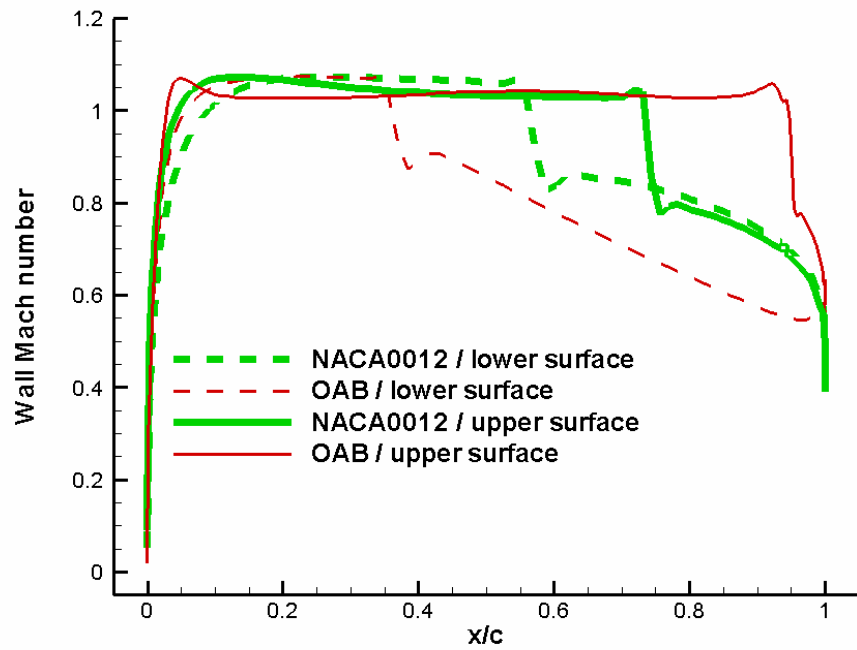


(b)

Figure 29: Lifting airfoil 2-point performance optimization. Wall distributions (a) (b) at OP#1 for the NACA0012 airfoil and an optimal airfoil for DG flow.

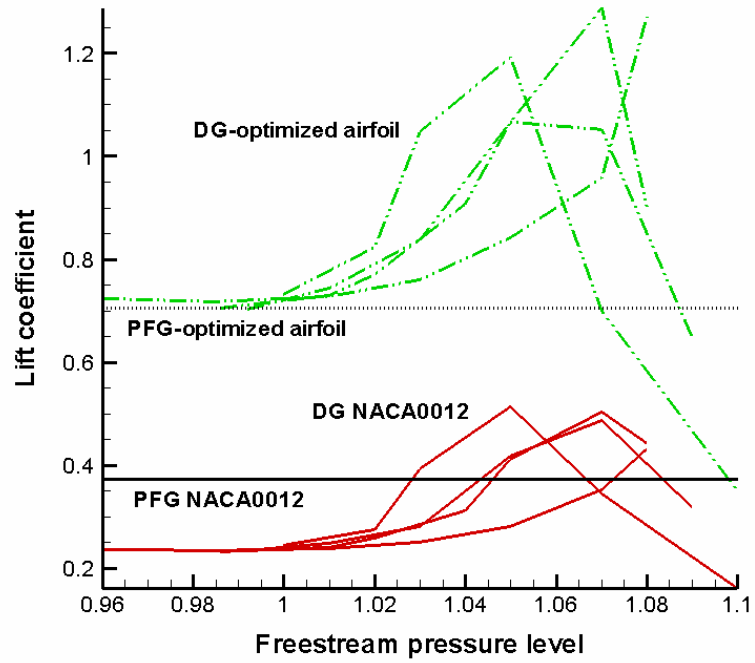


(a)

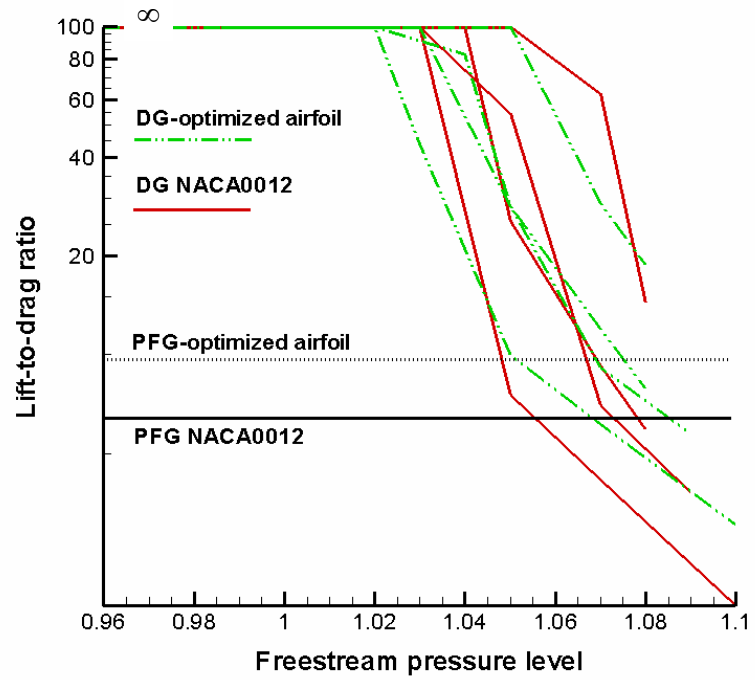


(b)

Figure 30: Lifting airfoil 2-point performance optimization. Wall distributions (a) (b) at OP#2 for the NACA0012 airfoil and an optimal airfoil for DG flow.

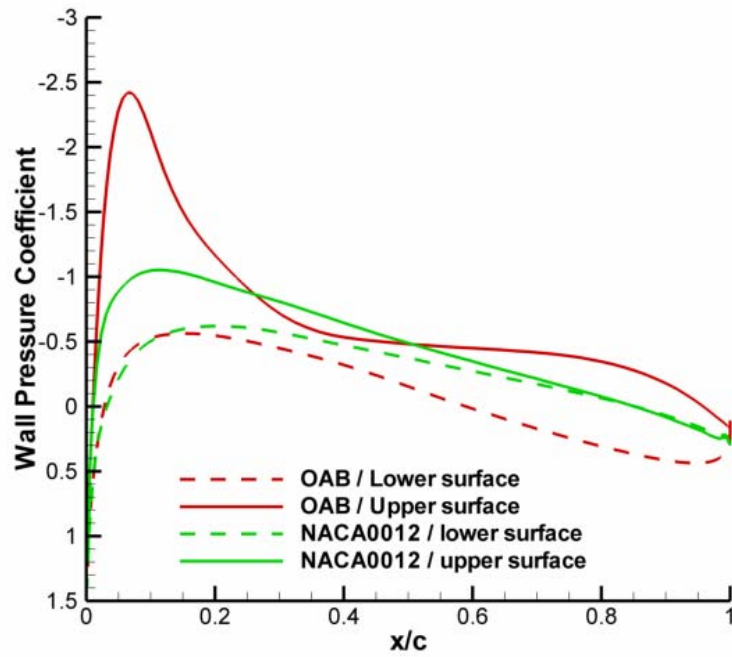


(a)

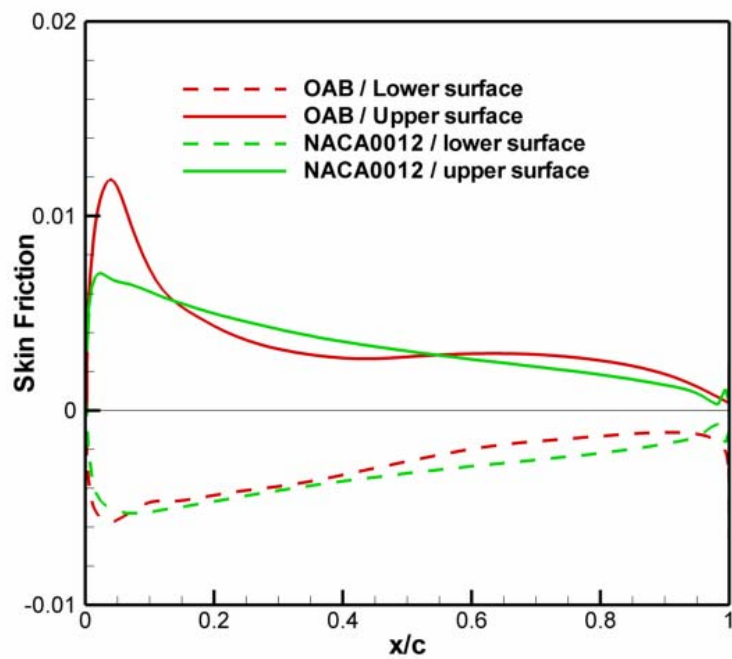


(b)

Figure 31: Evolution of aerodynamic performances (a) (b) at $M_\infty=0.85$ and $\alpha=1^\circ$ for a dense gas flow around the NACA0012 airfoil and a DG-optimized airfoil at different free-stream thermodynamic conditions.

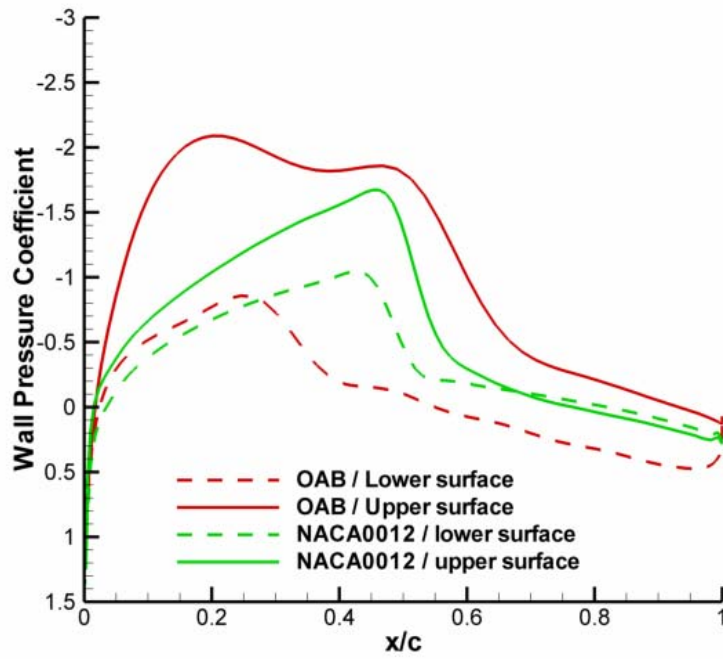


(a)

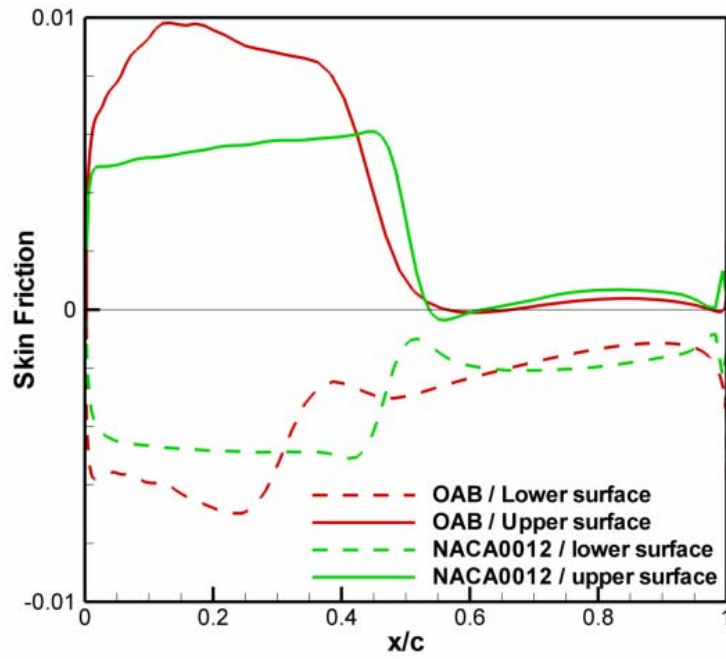


(b)

Figure 32: Lifting airfoil 2-point performance optimization. Wall distributions (a) of the pressure and skin friction (b) coefficients for viscous flow at OP#1 past the NACA0012 airfoil and an optimal airfoil for DG flow.



(a)



(b)

Figure 33: Lifting airfoil 2-point performance optimization. Wall distributions (a) of the pressure and skin friction (b) coefficients for viscous flow at OP#2 past the NACA0012 airfoil and an optimal airfoil for DG flow.

4.3.2. Viscous Case

In the cases widely described in 4.3.1.1 and 4.3.1.2 the optimizer was linked to an Euler solver and after the optimized airfoils were analyzed to check their viscous performances. It seems really interesting to couple the optimizer to a NS code, because it's important to understand if it is necessary a viscous optimization to generate a profile with good viscous performances, or it suffers just to make a faster optimization neglecting viscous effects, followed by an evaluation of viscous effects on the optimized airfoil. Obviously there is a huge difference in the computational cost (order of seven times more expensive for the viscous case). In order to reduce computational costs for viscous dense-gas flow optimization problems, the flow solver (actually viscous computations have been just done with SGS) and GA are coupled with an artificial neural network (ANN). The procedure used to couple the ANN with the flow-solver and the optimizer is the following:

- The fitness function is computed “exactly” by means of the Navier-Stokes solver for all individuals of the first two generations.
- These individuals form an initial training set for the ANN.
- Starting from the third generation, just only 30% of the individuals are computed “exactly”.
- At each generation, new exactly computed individuals are added to the training set, and the ANN is re-trained, in order to improve ANN accuracy while approaching the solution optimum. Because of the growing size of the linear system associated to the training problem, the ANN is not trained using all individuals in the data set. Instead, the ANN is trained “locally” by extracting from the global data set, a small number of individuals close to the one to be evaluated. This means that, for each new individual, a new local ANN is constructed. Based on numerical tests, a subset of 6 individuals was found to provide reasonable accuracy.

In any case, the best individuals retained for elitism are always computed exactly.

4.3.2.1. Drag Minimization for a Symmetric Airfoil

The problem is to find the minimal value of the drag coefficient $C_D(\Sigma)$ where Σ denotes an airfoil symmetric shape. It's the same problem considered in 4.3.1.1. But in this case, NS equations are used also for the evaluation of each profile. The same parameterization

described in 4.3.1.1 is used, then the family of airfoil shapes is entirely described by 11 parameters.

The minimization of $C_D(\Sigma)$ is performed for the following flow conditions: $M_\infty = 0.96$, reduced freestream pressure and density equal to 0.985 and 0.622, respectively ($\Gamma_\infty \approx 0.02$). At the considered free-stream conditions, the flow Reynolds number is about 10^7 . The calculation is performed using a half C-grid of 100x50 cells, selected after a proper mesh study (not reported for brevity) as the best compromise between accuracy and computational cost; the population contains 36 individuals, which are let to evolve during 24 generations. This is enough to reach a stabilized optimum, as shown by Figure 34: when iterating on the generation number, the minimal and the mean value of the fitness function in the population converge to the same asymptotic value, which indicates that the population tends to converge to a set of almost identical (optimal) individuals. The optimal geometry stemming from the optimization run is represented in Figure 35, along with the original NACA0012 profile. The computed drag coefficient for the optimal individual equals 1.010×10^{-2} . The value obtained for the flow past the NACA0012 airfoil at the same free-stream conditions is 1.544×10^{-2} . Perfect gas flow past the NACA0012 and the optimal airfoil obtained yields a drag coefficient equal to 6.320×10^{-2} . Provided that the main reduction in drag is related to the working fluid properties (the drag for PP10 flow past the baseline airfoil is about 5 times lower than for perfect gas flow past the same shape), the subsequent optimization run allows further reducing the drag of about 53%. In order to evaluate how important is taking into account viscous effects during the optimization process, an optimization run at the above operating conditions was also performed by neglecting fluid viscosity. The resulting optimal airfoil shape is also reported in Figure 35. Note that this airfoil is thicker than the optimal shape provided by the viscous optimization run. The performance of this individual is then *a posteriori* checked for a viscous turbulent flow at the previously specified conditions: the resulting drag coefficient is found equal to 1.388×10^{-2} , i.e. about 37% higher than the drag exerted on the “viscous” optimal individual. Figure 36 displays the iso-lines of the Mach number and a close-up of the flow streamlines close to the trailing edge for perfect gas flow past the NACA0012, dense-gas flows past the same airfoil, and dense-gas flow past optimal airfoil shapes obtained by either including or neglecting viscous effects. The maximum Mach number in the flow lowers progressively when passing from perfect gas flow to PP10 flow and from the latter

to PP10 flow past the optimal airfoils. As a consequence, the strength of the shock waves becomes lower and lower, and the flow field past the optimal airfoils is essentially shock-free. Nevertheless, while the airfoil obtained neglecting viscous effects, characterized by a thick nose, still displays a supersonic bubble in the leading edge region that terminates in a weak shock, the thin-nosed airfoil issued from the “viscous” optimization furthers a more gradual expansion, and the flow reaches just slightly supersonic conditions at about midchord. This is confirmed by inspection of Figure 37, showing wall distributions of the pressure coefficients for the four cases. It is interesting to inspect the streamline distributions for the four configurations (Figure 36). Both perfect and dense flows past the NACA0012 remain attached (Figure 36 A, B); the airfoil issued from the inviscid dense gas flow optimization, because of its thick trailing edge, allows reducing losses due to shock waves, but displays an extended separation bubble: this inconvenience is avoided by taking into account viscous effects during the optimization process, which leads to an airfoil ensuring at the same time low wave drag and attached flow in the trailing edge region. Actually, as shown in Figure 36 C, a very small separation bubble appears, but it has a negligible influence on the overall drag coefficient.

Since, ideally, a consistent drag reduction is expected for the whole range of freestream Mach numbers, the wave drag produced by these modified shapes, which are optimized for a specific value of M_∞ , are next checked for different values of M_∞ , taken in the interval [0.85, 0.99]. The computed evolution of the drag coefficient with increasing values of the freestream Mach number is plotted in Figure 38: the present optimal shape at $M_\infty = 0.96$ is far superior to the original NACA0012 airfoil, since its drag coefficient is lower for the whole range of Mach numbers and the transonic drag rise is delayed. Conversely, the airfoil issued from inviscid optimization is decidedly better than the NACA0012 for the highest values of the Mach number, but its drag is somewhat higher at lower velocities.

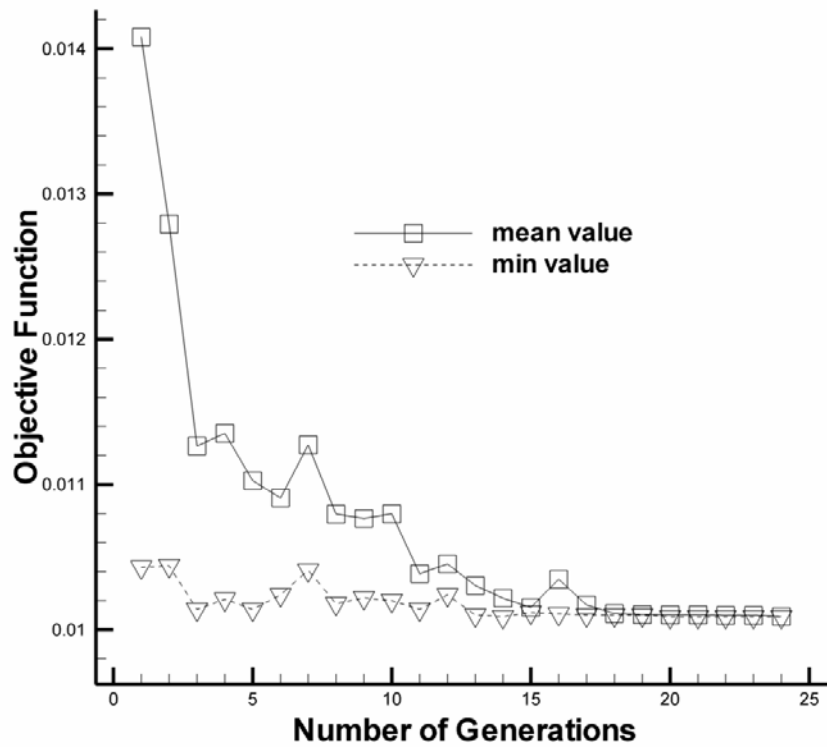


Figure 34: Evolution of the maximal and mean value of the drag coefficient for the computed population as a function of the number of generations.

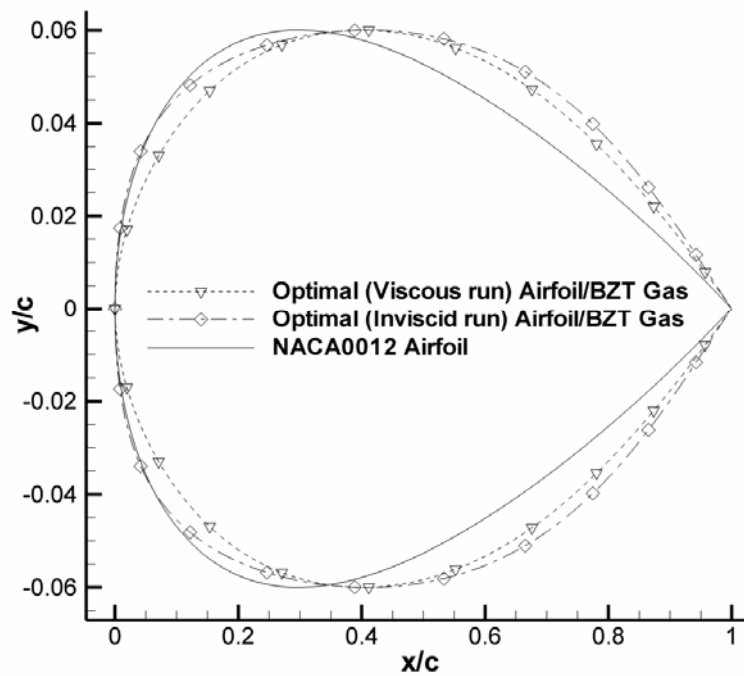


Figure 35: Geometry of minimal drag airfoils obtained by including or neglecting, respectively, viscous effects, and NACA0012 airfoil.

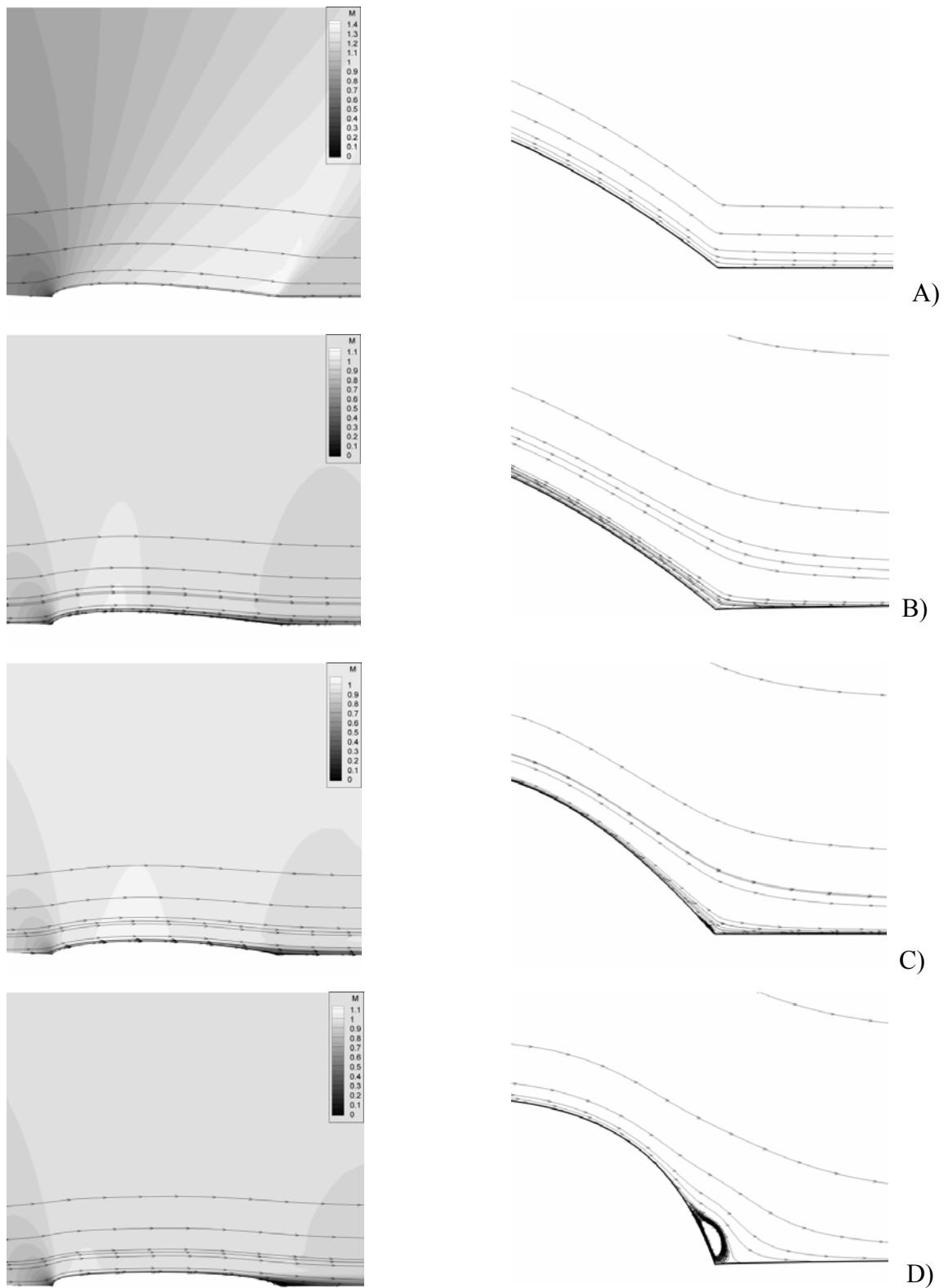


Figure 36: Mach number contours and streamlines for turbulent flows past four airfoils (right); left: close-up of the streamlines at the trailing edge (grid aspect ratio not preserved). A) NACA0012 perfect gas; B) NACA0012 dense gas; C) Shape optimized for viscous dense-gas flow; D) Shape optimized for inviscid dense-gas flow; $M_\infty=0.96$, $Re \approx 10^7$.

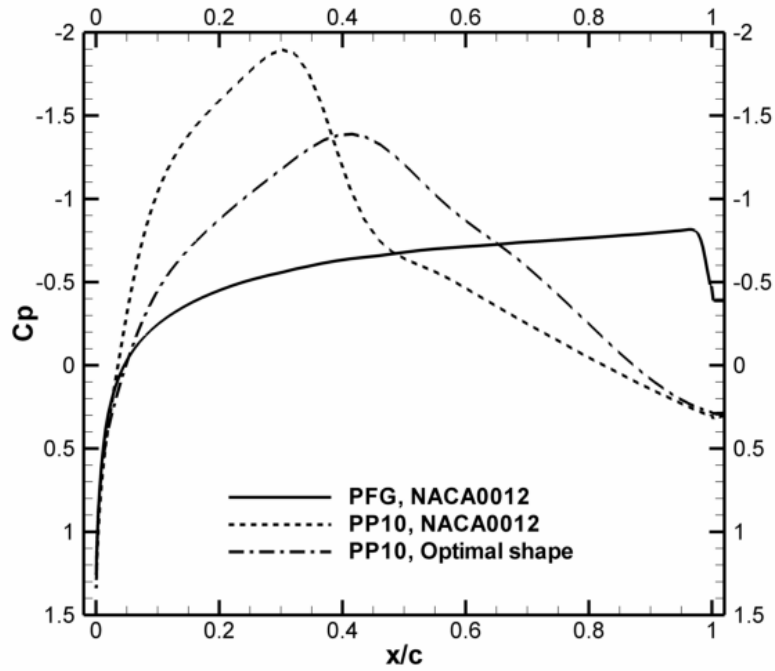


Figure 37: Wall distribution of the pressure coefficient for three cases plotted in Figure 36

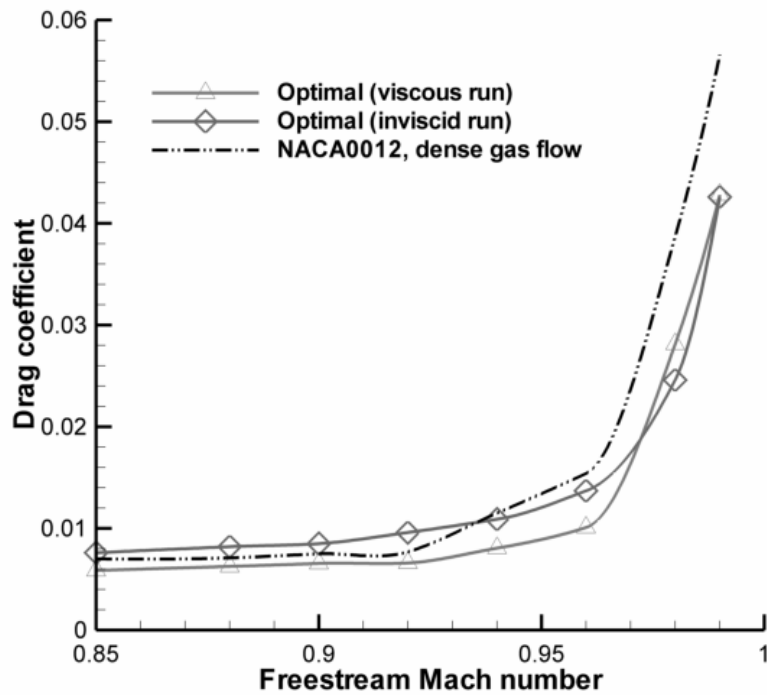


Figure 38: Drag coefficient as a function of the freestream Mach number for dense-gas viscous flow at operating conditions $p_{\infty}/p_c=0.985$, $\rho_{\infty}/\rho_c=0.622$. The figure compares the performance of an airfoil shape optimized for viscous dense gas flow, for an airfoil shape optimized for inviscid dense gas flow, and for the NACA0012 airfoil.

4.3.2.2. Performance optimization for a Lifting Airfoil

The second optimization problem is the design of optimal lifting airfoils. This problem is the same described in 4.3.1.2 for inviscid computations. The shape representation retained for the complete airfoil derives from that adopted in the study of a half profile, and it's the same already introduced in 4.3.1.2. RANS equations are used.

The flow conditions retained for the study are $M_\infty=0.85$, incidence angle 1° , Reynolds number (based on free-stream conditions and the airfoil chord) 9×10^6 . The same optimization strategy already described in 4.3.1.2 is adopted: to simultaneously optimize the lift coefficient $C_L(\Sigma; OP\#1)$ for an operating condition OP1 such that flow past the baseline NACA0012 configuration is subcritical and consequently characterized by no wave drag but relatively poor lift, and the lift-to-drag ratio $C_L / C_D(\Sigma; OP\#2)$, for an operating condition OP2 such that the flow past the baseline airfoil is supercritical, and offers quite high lift, but poor aerodynamic efficiency. Precisely, conditions OP1 and OP2 correspond exactly to those introduced in 4.3.1.2 for the inviscid case. The two objectives are simultaneously maximized by applying the MOGA with a population of 36 individuals during 24 generations. A partial view of the computed individuals is shown in Figure 39 along with the set of non-dominated solutions eventually obtained: it clearly illustrates that the initial NACA0012 airfoil aerodynamic performances in dense gas flow have been substantially improved through the optimization process. Specifically, there are four individuals of the Pareto front that possess higher lift at condition OP1 and higher lift-to-drag ratio at condition OP2 than the NACA0012.

Note that the Pareto front resulting from an inviscid optimization run, also represented in Figure 39, is well above the Pareto front for the viscous run. This of course due to the fact that, for the inviscid computation, there is no viscous drag exerted on the airfoils, and that wave drag is extremely small due to BZT effects, which results in extremely high lift-to-drag ratios. The point representative of perfect gas flow past the NACA0012, characterized by slightly negative lift, is also reported for completeness. In order to draw a fair comparison with perfect gas flow, a shape optimization is also performed for the perfect gas ($\gamma=1.4$) flow at $M_\infty=0.85$ and 1° of incidence over an airfoil of 12% thickness-to-chord ratio with a geometry based on the Bezier curves previously described; with unique thermodynamic conditions for this PFG flow, the problem is expressed as maximization of the lift-to-drag ratio. The optimal solution obtained is plotted in Figure 39 in the lift / lift-

to-drag plane: it remains well below the optimal solutions associated with the DG flow: the optimized airfoil displays good aerodynamic efficiency, but its lift coefficient is considerably lower with respect to optimal individuals for dense gas flow.

In order to select a single individual among the eight ones composing the Pareto front, the aerodynamic performance of the airfoil is also studied at two off-design conditions. The objective is to select an airfoil shape ensuring good aerodynamic performance over the largest range of operating conditions. Results are reported in Table 2 for the 8 airfoils, the baseline NACA0012 airfoil, and an airfoil shape belonging to the inviscid Pareto front, which has been retained because, among the set of non-dominated solutions, it displays the thickness distribution in the trailing edge region that is the most likely to preserve good aerodynamic performances in the viscous case. The thermodynamic conditions retained for the study are OP1, OP2 and two test points TEST1 ($p_\infty / p_c = 1.005$, $\rho_\infty / \rho_c = 0.794$) and TEST2 ($p_\infty / p_c = 1.17$, $\rho_\infty / \rho_c = 1.11$), the first one corresponding to an intermediate state between OP1 and OP2, and the second one being characterized by operating pressure and density much higher than the design ones. Several considerations are in order: at the lowest pressures and densities, all airfoils of the Pareto front offer a much higher lift coefficient than the baseline airfoil, whereas their drag coefficient remains approximately the same (it is actually slightly higher): this results in values of the lift-to-drag ratio that are more than twice with respect to the NACA0012. At OP2 conditions, all airfoils display much higher lift than the NACA0012, whereas the lift-to-drag ratio is roughly similar. Finally, at TEST2 conditions just a few airfoils conserve a superior performance, whereas the others are similar or even worse than the NACA0012. Based on these considerations, the airfoil indicated as Airfoil 4 in Table 2, which is the one offering the best overall performance at all operating conditions, is retained for further investigations. The last line of Table 2 illustrates the viscous aerodynamic performance of an airfoil shape optimized for inviscid dense gas flow (referred-to as Airfoil*). At conditions OP2 and TEST2, where the flow is dominated by shock waves, its performance is in line with airfoils derived from the viscous optimization run. At conditions OP1 and TEST1 one, its performance is still much better than the NACA0012, but it is well below the other airfoils, mainly because of its lower lift coefficient. It would be possible to extract from the inviscid Pareto front airfoils ensuring a much higher lift, but their viscous performance at high-pressure conditions is quite poor because of their thick trailing edges. Figure 40 compares the

geometry of this airfoil to Airfoil 4 and to the NACA0012. As for the previous non-lifting case, the airfoil optimized for viscous flow displays thinner leading and trailing edges with respect to the one optimized for inviscid flow, and a slightly thicker trailing edge when compared to the NACA0012.

The iso-Mach lines and wall pressure distributions computed on the NACA0012 airfoil, Airfoil 4, and Airfoil* for subcritical (OP1) and supercritical (OP2) conditions are plotted in Figure 41 and Figure 42. The flow over Airfoil* and, to a smaller extent, over Airfoil 4, separates at the upper surface, downstream of the compression shock at conditions OP2. Such shock is stronger with respect to that forming at NACA0012's upper surface, and closer to the trailing edge. This produces higher lift, but also higher drag, both related to shocks and to post-shock separation; nevertheless for Airfoil 4, which is specifically shaped for viscous flow, the lift-to-drag ratio remains slightly above that of the NACA0012 (about + 3%), whereas for Airfoil*, which displays a quite extended separated region at the upper surface, this ratio is 12% lower than for the baseline geometry. Then, it's possible to say that the additional cost related to evaluations of the fitness function via a Navier-Stokes solver is completely justified by performance improvements offered by the optimized airfoils.

	OP1 ($p_\infty/p_c=1.01, \rho_\infty/\rho_c=0.676$)			TEST1 ($p_\infty/p_c=1.05, \rho_\infty/\rho_c=0.794$)			OP2 ($p_\infty/p_c=1.08, \rho_\infty/\rho_c=0.882$)			TEST2 ($p_\infty/p_c=1.17, \rho_\infty/\rho_c=1.11$)		
	C_L	C_D	C_L/C_D	C_L	C_D	C_L/C_D	C_L	C_D	C_L/C_D	C_L	C_D	C_L/C_D
Airfoil 1	0.675	0.0167	40.4	0.763	0.0174	44.0	0.346	0.0621	5.58	0.056	0.0897	0.63
Airfoil 2	0.618	0.0160	38.6	0.699	0.0179	39.1	0.499	0.0650	7.67	0.128	0.0990	1.29
Airfoil 3	0.722	0.0169	42.8	0.819	0.0195	42.1	0.326	0.0615	5.29	0.155	0.0981	1.58
Airfoil 4	0.658	0.0159	41.3	0.750	0.0174	43.2	0.549	0.0722	7.60	0.165	0.0999	1.65
Airfoil 5	0.538	0.0161	33.4	0.604	0.0183	33.1	0.496	0.0626	7.92	-0.016	0.1120	-0.14
Airfoil 7	0.725	0.0167	43.3	0.819	0.0196	41.9	0.287	0.0616	4.67	0.138	0.0980	1.41
Airfoil 8	0.663	0.0162	41.0	0.757	0.0179	42.4	0.475	0.0681	6.98	0.057	0.0952	0.60
Airfoil 9	0.585	0.0156	37.5	0.668	0.0175	38.2	0.485	0.0615	7.89	0.022	0.1041	0.22
Airfoil* (inviscid run)	0.537	0.0157	34.2	0.608	0.0171	35.5	0.442	0.0688	6.43	0.017	0.0899	0.18
NACA0012 (DG flow)	0.183	0.0128	14.4	0.213	0.0142	15.0	0.253	0.0345	7.34	0.076	0.0983	0.77

Table 2: Parametric study of the aerodynamic performance of several airfoil shapes.

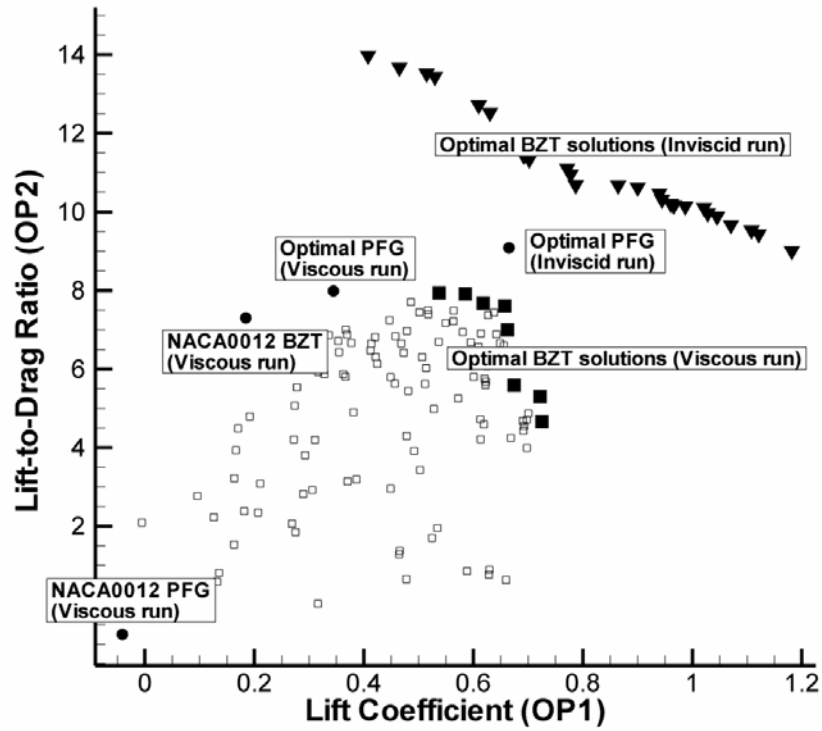


Figure 39: Lifting airfoil 2-point performance optimization. Overview of the computed solutions during the genetic evolution process.

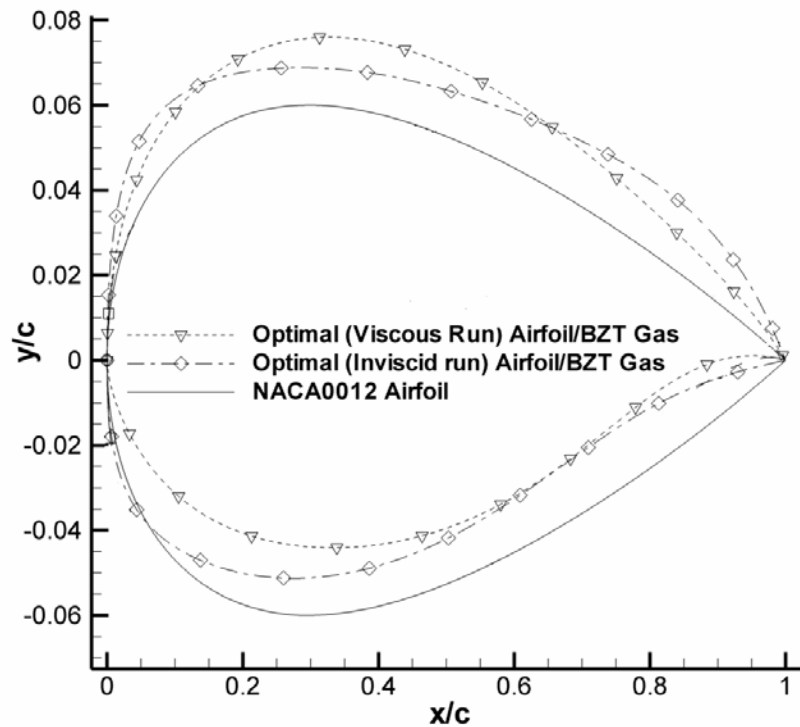
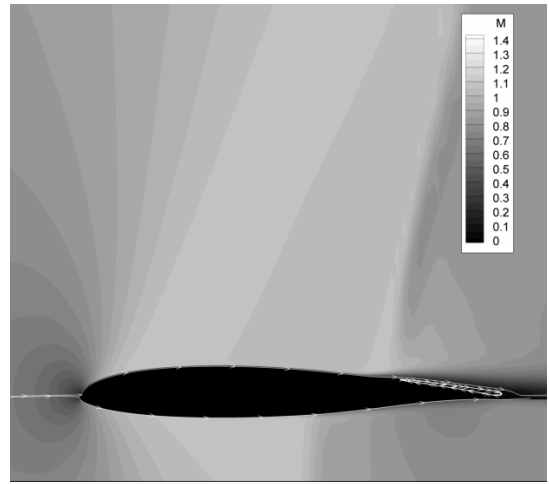
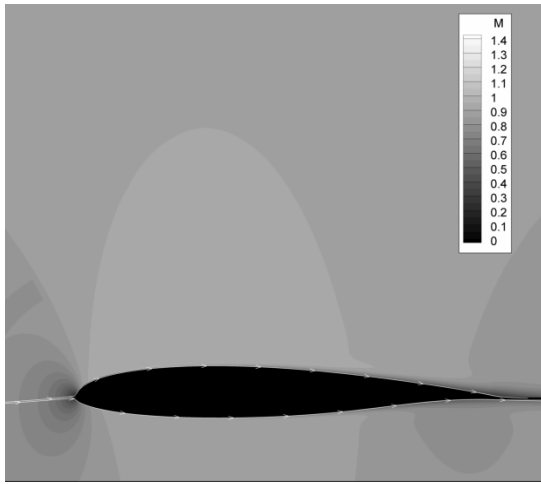
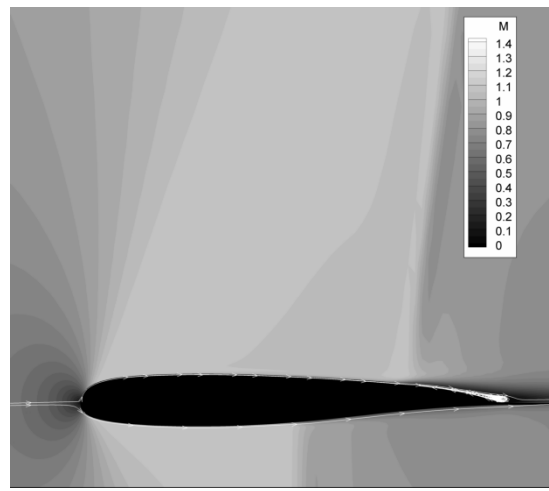
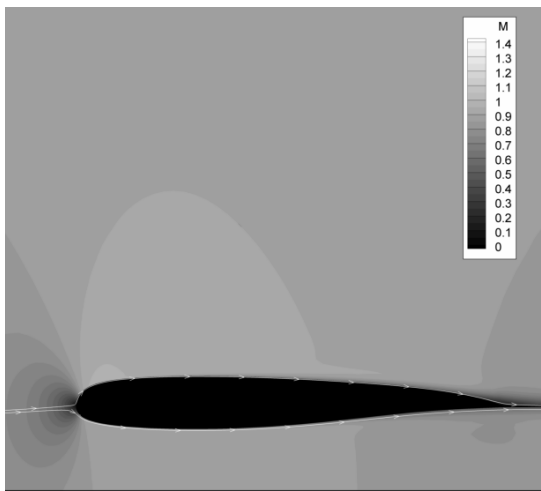


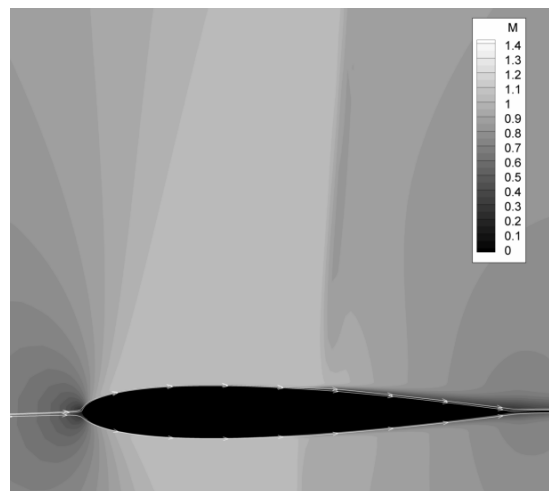
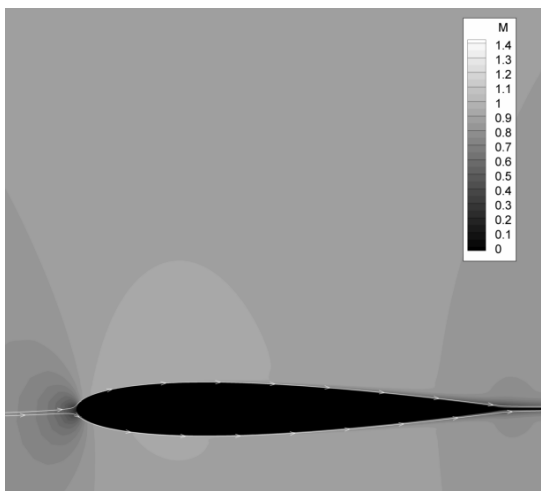
Figure 40: Optimal airfoil shapes and baseline shape for the lifting flow problem.



(A)



(B)



(C)

Figure 41: Mach number contours and flow streamlines for Airfoil 4 (A), Airfoil* (B) and the NACA0012 airfoil (C). $M_\infty=0.85$, $\alpha=1^\circ$, $Re=9\times 10^6$. Left: condition OP1; right: condition OP2.

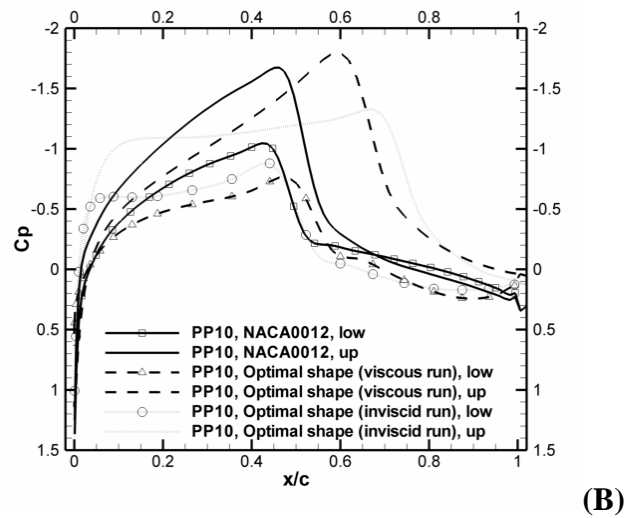
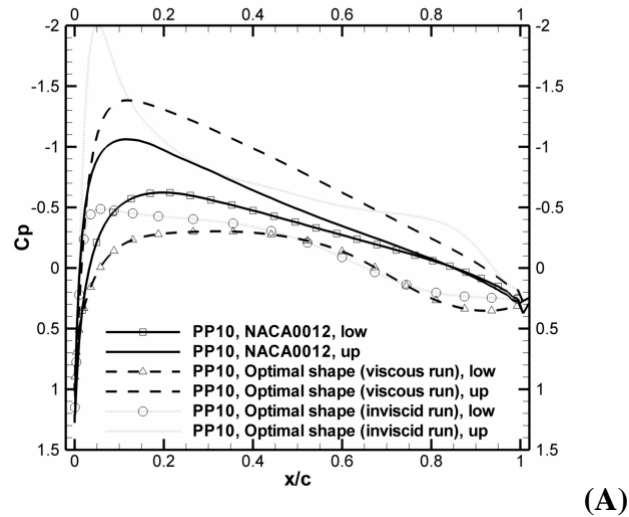


Figure 42: Wall distributions of the pressure coefficient C_p for Airfoil 4, Airfoil*, and NACA0012. $M_\infty=0.85$, $\alpha=1^\circ$, $Re=9\times 10^6$. A) Condition OPI; B) condition OP2.

4.4. Efficiency Maximization for a turbine cascade

The MOGA optimizer, coupled with the flow solver and a structured mesh generator is applied to shape optimization of turbine cascades. Blade shape is parameterized using Bezier polynomials, starting from the baseline profile VKI LS-59. Sixteen control points are imposed to parameterize the profile. Globally the optimization problem depends on twenty-five variables. Geometric constraints are imposed on the maximum blade thickness and on trailing edge thickness (normalized with the blade chord) that may vary within $\pm 10\%$ of the corresponding non-dimensional thickness for the baseline geometry. The turbine cascade is operated with an inlet flow angle of 30° and a pressure ratio of 1.82

corresponding, for a perfect diatomic gas, to sonic isentropic exit conditions. For dense gas flows, inlet thermodynamic conditions, i.e. the thermodynamic operation point, should be also specified. All the computations presented in the following are performed on C-grids composed by 192×16 cells, with average non-dimensional height of the closest cells to the wall approximately equal to 5×10^{-3} . This mesh refinement provides a reasonable tradeoff between accuracy and computational cost. Since the objective function chosen for optimization runs is cascade efficiency (defined as real-to-ideal static enthalpy drop), preliminary computations have been performed, for the baseline configuration, to investigate the sensitivity of this parameter to mesh refinement. Results computed on finer grids composed by 382×32 (first cell height 10^{-3}) at several flow conditions show that the magnitude of cascade efficiency tend to increase of about 2 ÷ 3% when refining the grid, but trends of behavior (e.g. efficiency dependency on inlet conditions) are well conserved. Firstly, a single-objective shape optimization for a diatomic perfect gas (PFG) has been performed in order to maximize turbine efficiency. The initial population of the genetic algorithm is selected after a preliminary DOE over 100 individuals. After about 20 generations the mean and maximum value of the objective function in the population reach approximately the same value, indicating that the GA has converged to a population of almost identical (optimal) individuals. The solution for the baseline blade is characterized by an oblique shock at about 70% the chord and a second shock attached to the trailing edge (Figure 45 a); computed efficiency is 93.2%. Figure 45 b shows the solution after shape optimization: the oblique shock is almost suppressed, the trailing edge shock is weaker with respect to the reference case and efficiency grows to 96.2%. Figure 45 c and Figure 45 d display Mach number and pressure (normalized by inlet stagnation conditions) distributions at the wall. For the optimal configuration the maximum Mach number at the wall and, consequently, shock strength, is noticeably reduced compared to the baseline configuration; consequently, wave drag lowers and cascade efficiency improves. The optimal individual (Figure 43) has a thicker leading edge, thinner trailing edge, and greater camber than the baseline configuration. Then, computations are performed with the BZT fluorocarbon PP10 as the working fluid. Three optimization runs are undertaken. In the first and second run, a single objective function is maximized, i.e. cascade efficiency at fixed operating conditions $p_{inl}/p_c = 1.00$, $\rho_{inl}/\rho_c = 0.752$, $\Gamma_{inl} = 0.416$ (optimization point OPT1) and $p_{inl}/p_c = 1.10$, $\rho_{inl}/\rho_c = 1.09$, $\Gamma_{inl} = 1.91$ (optimization point OPT2), respectively.

Subscript c indicates critical point values. Both operation points lay on an isentrope crossing the inversion zone, respectively at lower and higher pressure than peak efficiency conditions. In the third run, both objectives (i.e. efficiencies at OPT1 and at OPT2) are simultaneously maximized. Here again, a DOE is preliminarily run in order to properly initialize the population of the GA. Figure 44 shows optimal individuals for operating conditions OPT1 and OPT2 and an individual selected on the Pareto front resulting from the two-point optimization. The baseline profile is also represented. For each configuration, a parametric study of cascade efficiency at off-design conditions has been performed. In addition to operation points OPT1 and OPT2, two test points corresponding to operating conditions $p_{inl}/p_c = 1.02$, $\rho_{inl}/\rho_c = 0.813$, $\Gamma_{inl} = 0.886$ (TEST1) and $p_{inl}/p_c = 1.05$, $\rho_{inl}/\rho_c = 0.944$, $\Gamma_{inl} = 1.62$ (TEST2) are considered. Results are summarized in Table 3. Note that optimal individuals provide an improvement of 1 ÷ 2% only over the baseline at optimization conditions. However, improvements up to 7% are obtained at conditions TEST1 and TEST2, which lay close to peak efficiency conditions for the baseline cascade. The best overall results are obtained for the individual derived from the two-point optimization ("Pareto 1"). Note that its shape is quite similar to that of the optimal individual for perfect gas flow. Figure 46 a and Figure 46 b show iso-Mach lines for the baseline configuration and for individual "Pareto 1" at operating condition TEST2. Figure 46 c and Figure 46 d show the Mach number and Γ distributions at the wall for the best individuals from single-objective optimizations, the "Pareto 1" individual and the baseline blade. Here again the mechanism leading to efficiency improvement is a reduction in the maximum Mach number of the flow and hence of shock strength: major gains come from a significant weakening of the trailing edge shock for the optimized configuration. This is related to lower values of Γ at the rear part of the suction side, causing slower growth of the Mach number when the flow re-expands downstream of the first shock.

	OPT1	TEST1	TEST2	OPT2
Γ_{inl}	0.416	0.886	1.62	1.91
Best OPT1	91.25	95.74	97.20	89.71
Best OPT2	89.67	95.45	96.08	90.22
Pareto 1	91.00	96.36	97.47	89.75
VKI LS-59	88.66	90.72	90.80	88.77

Table 3: Efficiencies (%) for optimal blade shapes at several operating conditions.

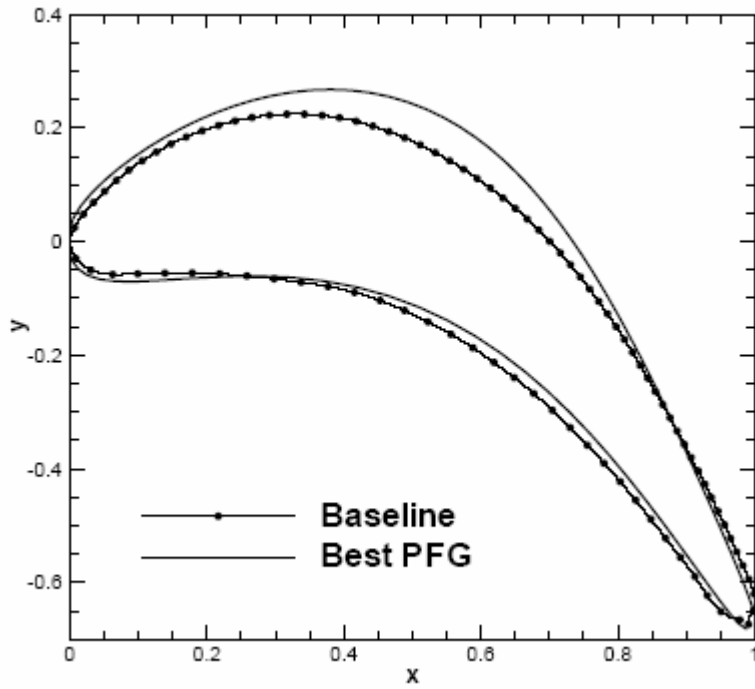


Figure 43: optimal shape for perfect gas flow

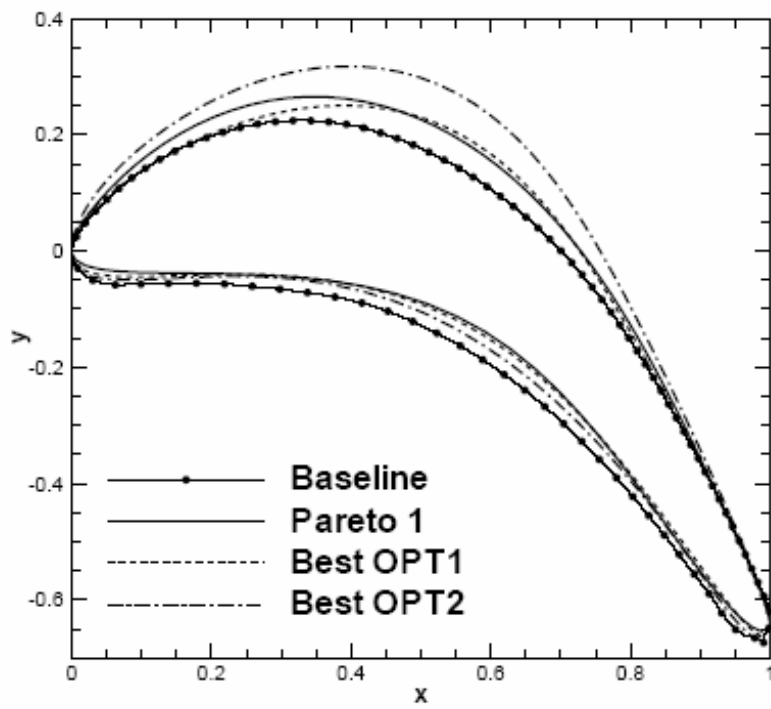
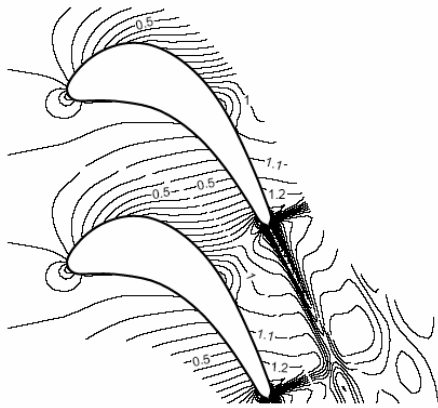
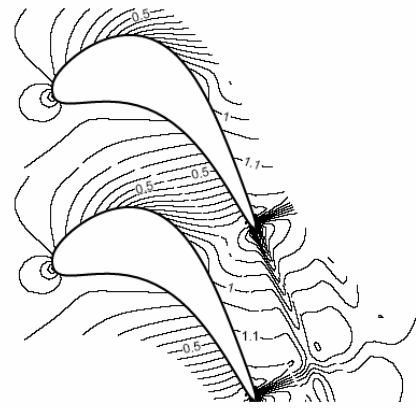


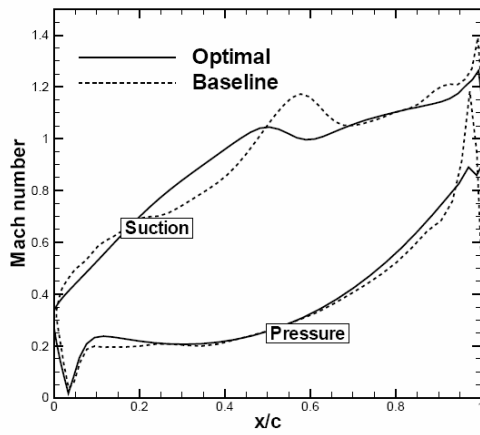
Figure 44: optimal shape for dense gas flow



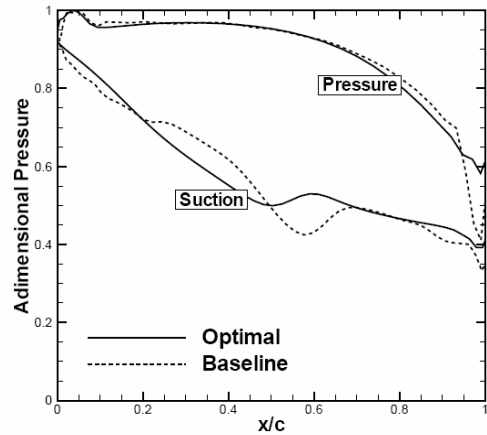
(a)



(b)

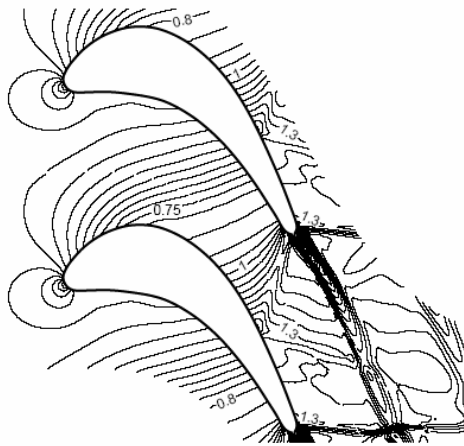


(c)

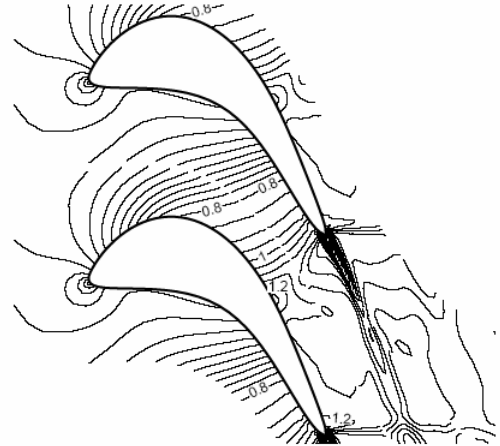


(d)

Figure 45: PFG flow, isoMach lines: a) baseline; b) optimized. c,d) Wall distributions.



a)



(b)

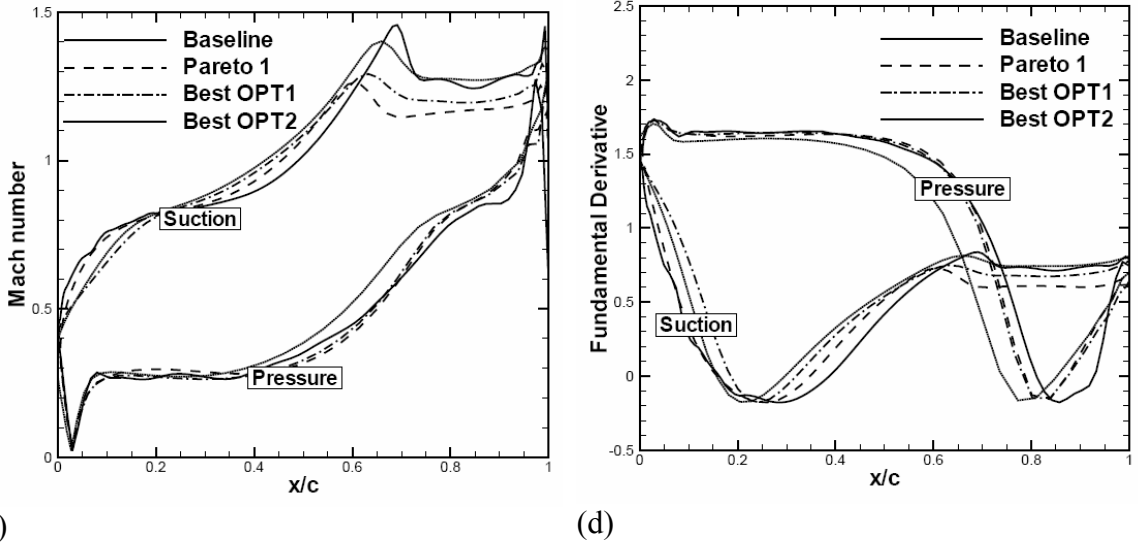


Figure 46: DG flow, isoMach lines: a) baseline; b) optimized. c,d) Wall distributions.

4.5. GA-Hardness of Drag minimization problem

A reference single-objective optimization problem, namely, wave drag minimization for a non-lifting inviscid transonic flow past a symmetric airfoil, is considered. This study shows a difficulty to converge toward a global optimum.

Several optimization runs are performed for a perfect diatomic gas (specific heat ratio $\gamma = 1.4$) and for a polytropic BZT van der Waals gas with $\gamma = 1.02$ flowing past an airfoil at different free-stream conditions. If not specified otherwise, numerical results are obtained using the Jameson's scheme [66] on a half-C grid composed by 100×30 cells; the outer boundary is located about 10 chords away from the airfoil, and the mean height of the closest cell to the wall is about 5×10^{-3} . Sensitivity of GA convergence to different choices of the starting population, computational grid, and discretization scheme is carefully analyzed.

4.5.1. Drag Minimization for a Symmetric Airfoil

An inviscid perfect gas (PFG) flow at $M_\infty = 0.83$, $\alpha = 0^\circ$, with M_∞ the free-stream Mach number and α the angle of attack, is considered first. The chosen value of the Mach number is slightly above the transonic drag rise condition for an airfoil of 12% thickness (about 0.8). As it is well-known, transonic drag rise is related to the occurrence of supersonic flow regions around the airfoil, with subsequent appearance of shock waves and associated losses, i.e. wave drag. As a consequence, for flow Mach numbers above a

critical value (the critical Mach number, M_c), the total drag coefficient increases abruptly. Nevertheless, if M_∞ is just slightly above M_c , shock waves appearing in the flow field remain relatively weak, since the maximum Mach number in the flow is relatively close to one. For a population of airfoils of given relative thickness, shock waves will be more or less strong according to the particular shape of an individual; individuals closest to the global optimum, i.e. with the lowest drag coefficient, are expected to produce particularly weak shocks or, eventually, a completely shock-free flow. In the latter case, C_D exactly equals zero for all airfoil shapes such that $M_{\max} \leq 1$, where M_{\max} is the maximum Mach number in the flow-field, and a continuous subset of global optima exists. Of course, this is due to limitations of the adopted flow model, which excludes viscous effects from considerations. For this reason, it was chosen to optimize the airfoil shape for flow conditions somewhat above the critical ones, in order to get supercritical flow for all individuals in the search space and, consequently, to be able to select a unique global optimum. In practice, because of numerical errors introduced by the numerical scheme and boundary conditions, C_D is not exactly zero even for completely subsonic flow-fields, but takes instead small positive values. In order to distinguish between subcritical and supercritical airfoils, a numerical check on the flow maximum Mach number is introduced, and C_D is forced to be zero if $M_{\max} \leq 1$. For supercritical flows characterized by strong shock waves, contribution of numerical errors to the total drag is generally negligible. Problems can arise for flow-fields characterized by very weak shock waves, i.e. for individuals close to the global optimum. For these individuals, numerical drag can represent a considerable amount of the total drag if the numerical evaluation of the fitness function is not sufficiently accurate; conversely, the more accurate is the numerical scheme and the finer the computational grid, the smaller the numerical error on C_D .

Firstly, two optimization runs are performed using different randomly-generated starting populations. For each run, the GA-driven population appears to have reached a stabilized optimal (minimal) value of the drag coefficient after the prescribed number of generations: the maximum and mean value of the drag coefficient in the final population of airfoil shapes are almost the same in each case, which hopefully indicates that the algorithm has converged to a population of almost identical geometries. Nonetheless, optimal airfoils obtained in the two runs display considerable geometric differences, precisely, about 8%, based on the distance measure ((Eq. 19). Since both optimization runs provide stabilized

solutions, this implies that the GA evolves during a given number of generations, and finally stagnates, generating random individuals in the neighborhood of the optimum without ever reaching it. The two optimal solutions obtained in the two runs are represented in Figure 47(a) along with the classical NACA0012 airfoil shape, which is taken as a reference. The corresponding Mach number distributions at the wall are displayed in Figure 47(b). The drag coefficients obtained in the two cases are equal to 7.02×10^{-3} and 6.94×10^{-3} (it equals 1.64×10^{-2} for the reference NACA0012 airfoil). In order to evaluate the fitness distance correlation of the present minimization problem, an estimation of the solution global optimum is required. This is obtained by refining the GA solution by means of a gradient-based method (see 3.2). The subset of designs used to compute the FDC is the global GA population generated during 30 generation for both optimization runs (about 1800 individuals, some repeated). The resulting FDC value, equal to about 0.7, is relatively far from the ideal value $FDC=1$: as a consequence, the problem can be considered to be GA-hard. GA convergence difficulties can be related to the fact that very weak shocks characterize the best individuals, which provide an almost shock-free flow. Because of numerical errors, a numerical “viscous” drag adds to the small physically relevant wave drag. For sufficiently similar individuals, it is reasonable to believe that this numerical drag, related to the chosen grid density and numerical scheme, is essentially independent from the particular airfoil shape, contrarily to wave drag that is more sensitive to shape changes. In the neighborhood of the global optimum, the effect of numerical drag is to “smooth out” the fitness function minimum, i.e. to reduce fitness function concavity. In these conditions, a GA will continue to generate randomly individuals characterized by more or less the same small drag coefficient without being able to detect the optimal one. In order to check the influence of numerical errors on GA convergence, optimization runs are repeated using a finer grid of 150×50 cells, mean height of the closest cell to the wall 10^{-3} chords. Grid refinement reduces numerical errors and provides sharper shock waves. Optimal shapes obtained using the finest grid are much closer each other (1.9% differences) and to the optimal value determined by refining the solution with the gradient-based method. The FDC for this case is 0.852, a closer value to 1. This result supports the conclusion that, for transonic flows of perfect gas characterized by weak shock waves, numerical viscosity behaves as a low-pass filter that levels a variety of low-drag profiles close to the optimum to the same degree of fitness.

Next, a dense gas flow optimization is considered. The working fluid is supposed to be a BZT polytropic van der Waals with a specific heat ratio equal to 1.02. When dense gas flows are considered, the free-stream Mach number and the angle of attack are no longer sufficient to completely determine the flow field, but information about free-stream thermodynamic conditions has to be added: for all computations presented in the following, the operating pressure and density, normalized with their critical-point values, are taken equal to $p_\infty / p_c = 1.0696$, $\rho_\infty / \rho_c = 0.735$. With this choice, the free-stream value of the fundamental derivative is $\Gamma_\infty = 0$. Viscous effects are neglected. Previous studies on BZT flows past airfoils (see [40]) show that, on the one hand, the peculiar behavior of the sound speed in BZT flows considerably delays the transonic drag rise with respect to a perfect gas flow over an airfoil of the same thickness; for the BZT gas and operating conditions considered in this study, the critical Mach number is found to be around 0.94 for an airfoil of 12% thickness. On the other hand, even when the flow finally becomes supercritical, shock waves characterizing the flow-field for $M_\infty > M_c$ are not only weak, as previously observed about PFG flows, but they also generate losses (entropy gradients) up to one order of magnitude weaker than those generated in a PFG for a shock wave of the same intensity if their jump conditions are located in the vicinity of $\Gamma_\infty = 0$.

Firstly, BZT flow at $M_\infty = 0.95$ is considered, i.e. slightly above critical conditions. In order to get a more detailed knowledge of the search space, a design of experiment (DOE) is performed over a sample of 600 individuals. The DOE analysis uses a Sobol sequence technique, which ensures a uniform covering of the search space. The results are summarized by means of a frequency histogram (see Figure 48). Individuals are collected into 20 classes according to their fitness (drag coefficient). A considerable number of individuals, corresponding to 3% of the whole population, belong to the lowest drag-coefficient class. These are quite different in shape, i.e. a large variety of shapes providing good values of the fitness function exists. The best 36 individuals detected by the DOE are used to initialize the GA, whose population is allowed to evolve during 30 generations. The GA population appears to have reached a stabilized optimal value of the drag coefficient after the prescribed number of generations. In order to investigate the sensitivity of the GA to the starting population, four optimizations runs are performed with different randomly generated starting populations. All optimization runs converge within

the prescribed limit of 30 generation; nevertheless, quite different optimal shapes are generated (differences up to 22.6%). The resulting profiles are shown in Figure 49. The corresponding values of the fitness function are 0.00117, 0.00109, 0.00121, 0.00112, respectively. Evaluation of the FDC for this case returns a value of 0.534, much lower than that obtained for the previous perfect-gas problem. The high sensitivity of the GA to the starting population can be related to the fact that, due to the peculiar BZT fluid properties, shock waves are extremely weak for a large range of airfoil shapes in the neighborhood of the optimum: for all of these shapes, numerical drag represents a large part of the total one and tends to “hide” differences of the fitness function for airfoil shapes close to the optimum. The effect of numerical errors on the computed solution and, subsequently, on GA convergence properties, are investigated through a systematic analysis of the influence of different computational grids and discretization schemes on the results. On the finer grid of 150×50 cells, optimal shapes much closer to each other (3.1% difference) are obtained for different choices of the starting population. The computed fitness of the global optimum is now $C_D = 4.94 \times 10^{-4}$, which is about 40% lower than the value computed on the coarser grid! That is, a considerable amount of the computed drag is due to numerical viscosity. Reduction of numerical errors results in an improvement of the FDC, which grows to 0.654. To further check how the flow physics (shock strength) affects GA convergence, the free-stream Mach number is increased to 0.98: very similar optimal shapes are obtained for any choice of the starting population (about 1.5% maximum difference), even when the second-order scheme and the coarsest mesh are used to evaluate the fitness. In this case however, the flow field is characterized by a strong shock close to the trailing edge and numerical dissipation is negligible (for at least second-order accurate numerical schemes) with respect to wave drag. Accordingly, the computed FDC for this case is much closer to one, $FDC = 0.926$

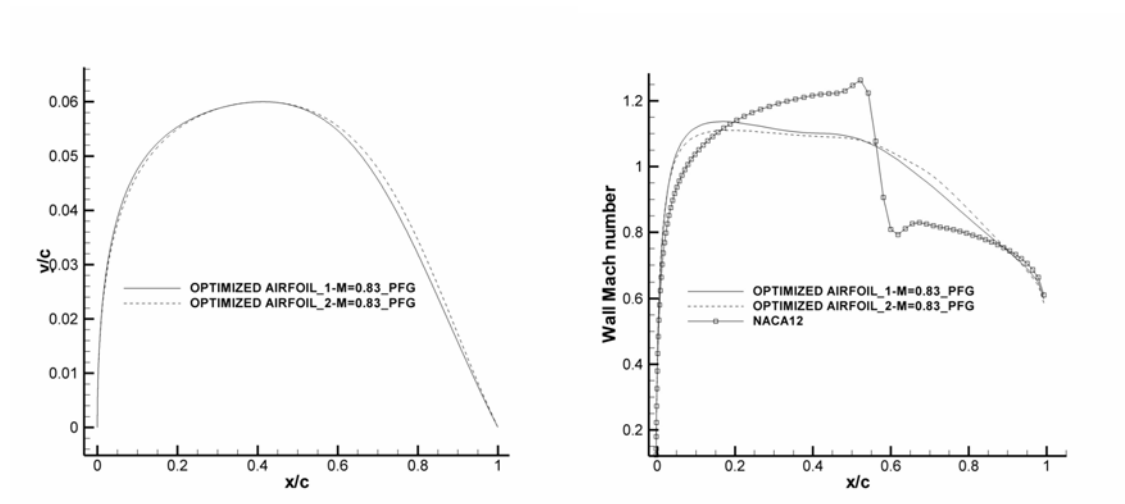


Figure 47: (a) Optimal geometries for the drag minimization problem for an inviscid perfect gas flow with $M_\infty=0.83$ obtained using different initial populations; (b) corresponding wall distributions of the Mach number.

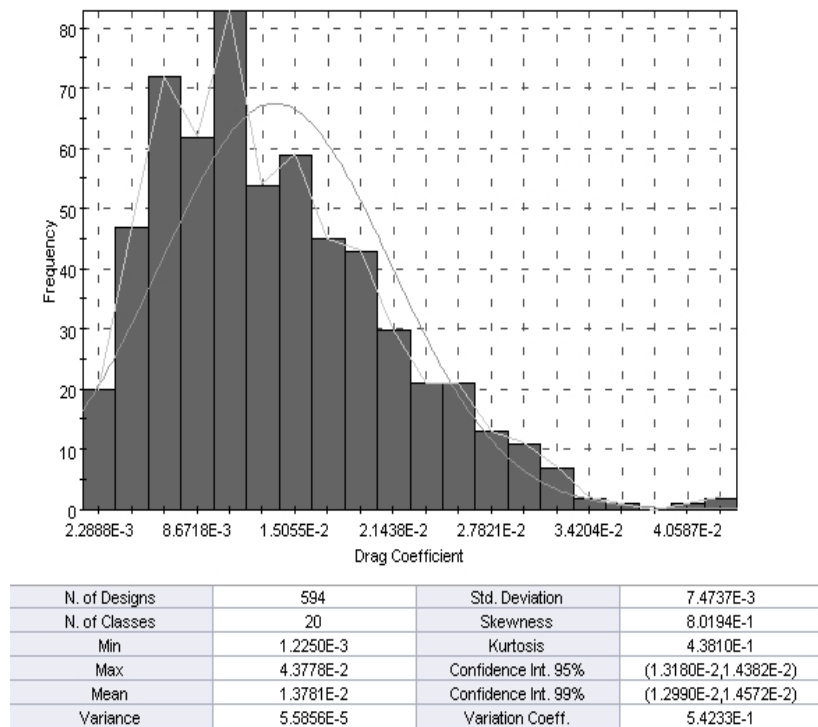


Figure 48: Frequency histogram for DOE data

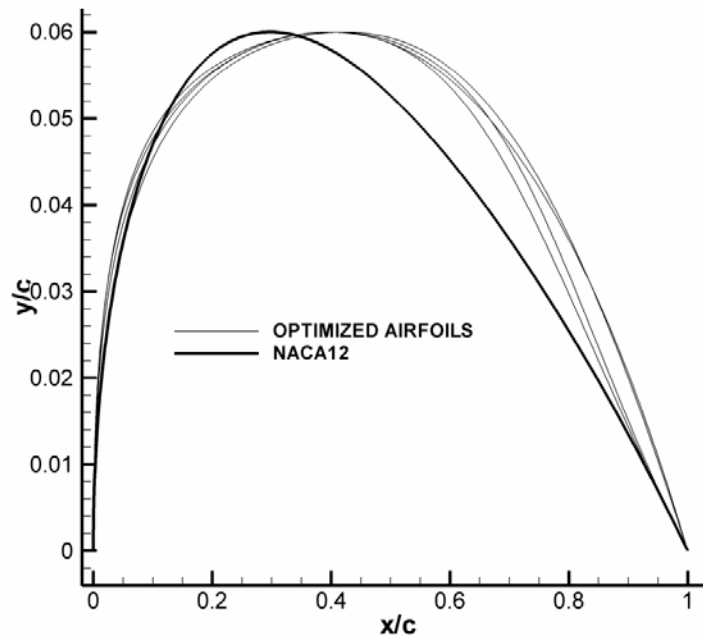


Figure 49: Optimal geometries resulting from four optimization runs with different starting populations

4.5.2. Cures to GA-Hardness

A standard way to improve GA convergence, already explored in several papers in the literature consists in constructing hybrid algorithms combining the GA with a local search gradient-based algorithm. The most used hybridization technique is the following: the GA is preliminarily run in order to roughly localize basins containing global optima; then, the solution is refined by applying a quick local search method that, using information about the solution gradient, quickly converges to the nearest optimum.

Similarly, the coarse-grid solutions provided by the GA is used to initialize a gradient-based method (see 3.2). The fitness-function gradient is approximated by central differences; after about 30 iterations, the solution converges toward a new individual characterized by a better value of the fitness function than both “optimal” individuals detected with the preceding GA runs. The computed drag coefficient is 1.64×10^{-2} for the NACA0012 and 5.00×10^{-3} for the optimized airfoil; this value also improve the results previously obtained by the GA.

The optimal solution for the inviscid dense gas flow at $M=0.95$ previously discusses in 4.5.1 is also locally refined by means of the BFGS algorithm. After convergence, an optimal airfoil shape is found , displaying a drag coefficient $C_D=9.75 \times 10^{-4}$. This value is

about 20.3% lower than the computed value for a flow at the same conditions past the reference airfoil NACA0012 ($C_D = 1.22 \times 10^{-3}$), due to a considerable reduction of shock-wave strength for the flow past the optimal shape with respect to the reference flow past the NACA0012. It also significantly improves previous results returned by the GA (about 1.1×10^{-3} in average). The overall CPU time for hybrid optimization runs required about 1300 fitness function evaluations, 800 required by the GA and 500 by the BFGS. This is due to the relatively high number of design variables used to parameterize the airfoil shape.

In the above, it was shown that for flows characterized by very low wave drag (typically for dense gas flows, but also for perfect gas flows at Mach numbers slightly above the critical one) the solution of the drag minimization problem is very slow and sensitive to numerical parameters used in the flow solver, such as numerical dissipation introduced by the scheme and the computational mesh used to evaluate the fitness function. It was also shown that the use of a more accurate scheme and of finer meshes allows reducing GA-hardness of a given problem. Unfortunately, the use of very fine meshes considerably increases computational costs. In order to alleviate this problem, a simple and effective method has been proposed in 3.3.2. The above strategy is now applied to one of the more difficult test cases of the previous section. Precisely, we consider again the drag minimization problem for a BZT van der Waals gas flow over a symmetric airfoil, with freestream conditions $M_\infty = 0.95$, $\alpha = 0^\circ$, $p_\infty / p_c = 1.0696$, $\rho_\infty / \rho_c = 0.735$. Firstly, a reference solution is computed by using a very fine mesh composed by 200×64 cells. CPU time required for a single fitness evaluation on this grid is about 40 minutes on a Pentium V processor. The whole optimization process requires about 800 fitness evaluations. Then, the same optimization run is performed by applying the multigrid strategy described above: for each individual, the fitness function is first computed using a coarse grid of 50×16 cells, then using a finer grid of 100×32 cells, finally a third value is extrapolated via Richardson's formula. The total CPU time required to obtain the final estimate of the fitness function is about 5 minutes! This noticeable reduction in computational time is due, on the one hand to the lower number of operation required to compute solutions on the coarser grids and, on the other hand to higher convergence rates of the flow solver. An important role is also played by initialization of the medium grid computation with the coarse grid solution. Let us recall that the computed FDC parameter of the GA for this

problem was 0.536 using a grid composed by 100×30 cellules (close to the present medium mesh). For the optimization run using the finer grid FDC grows to 0.676. For the multigrid optimization run, FDC is even better and equals 0.691. These results demonstrate once more the strong link between the fitness function evaluation accuracy and the convergence rate of the GA. Figure 50 shows geometries of optimal individuals obtained, respectively, by using the finest grid and the multigrid strategy to evaluate the fitness function. The two geometries are very close to each other, almost within plotting accuracy. The corresponding values of the drag coefficient are also very similar: $C_D = 7.32 \times 10^{-4}$ for the multigrid optimal individual (*a posteriori* evaluated on the finest mesh) and $C_D = 7.64 \times 10^{-4}$ for the fine grid one. Figure 51 shows iso-Mach lines, and wall pressure and Mach number distributions for the two solutions: once again, they are almost superposed. In summary, the proposed multigrid strategy allows improving GA convergence, and avoids *a posteriori* solution refinement via a gradient-based method. Moreover, computational cost for a single fitness evaluation just slightly increases with respect to a single medium grid evaluation. The resulting solution is very close to that obtained by computing the fitness function on a very fine mesh for all individuals; nevertheless, CPU time required by a single fitness evaluation using the multigrid strategy is about 1/8 with respect to a fine grid evaluation. Since a whole optimization run requires about 800 evaluations, the gain in total CPU time is dramatic.

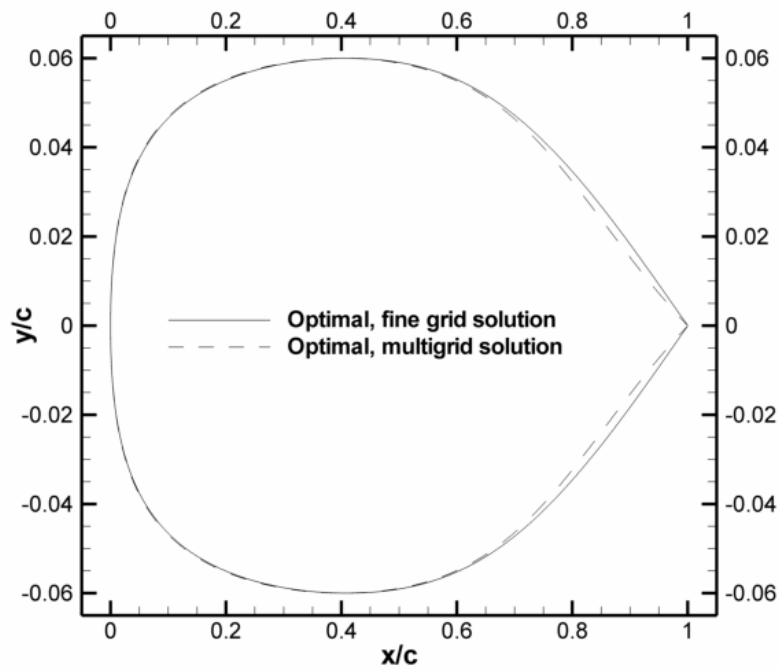


Figure 50: BZT van der Waals gas flow over a symmetric nonlifting airfoil. Optimal geometries obtained using a fine-grid estimate or a multigrid (Richardson extrapolation) estimate of the fitness function

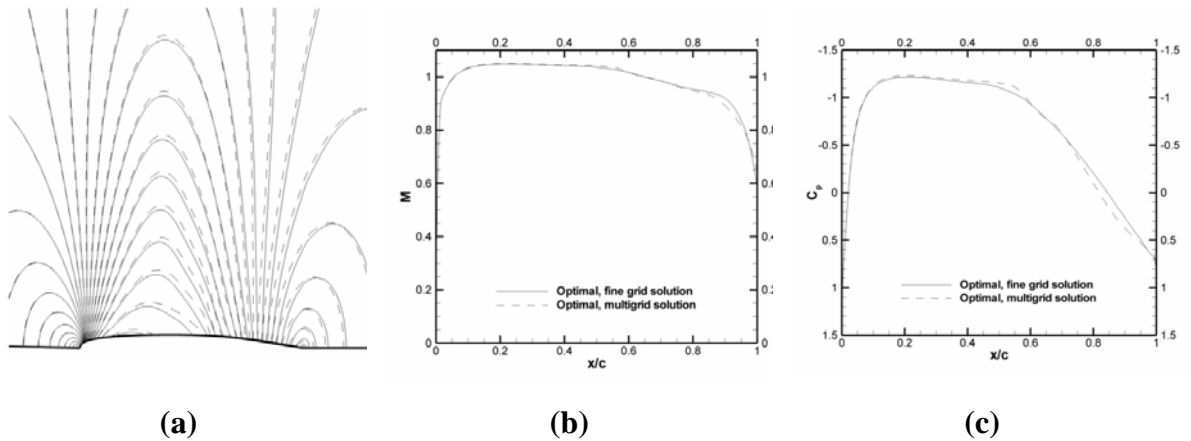


Figure 51: BZT van der Waals gas flow over a symmetric nonlifting airfoil. (a) Pressure coefficient isolines past optimal individuals ($\Delta C_p=0.1$); (b) wall Mach number; (c) Wall pressure coefficient

5. Conclusions

This work is devoted to the understanding of transonic flows of dense gases of the Bethe-Zel'dovich-Thompson (BZT) type, and to their possible exploitation as working fluids in Organic Rankine Cycles. All the studies previously made concerned basically the analysis of the flow in the BZT region, i.e. the thermodynamic region above the upper saturation curve where the fluid exhibits negative values of the Fundamental Derivative, i.e. the inversion zone. This operating region is particularly attractive because of the exotic gas dynamic behaviors which appear in the transonic and supersonic regime, namely, the disintegration of compression shock waves. Unfortunately, the design of ORCs operating the fluid expansion entirely within the inversion zone is made unpractical by its very limited extent in terms of pressure and temperature ranges. Results presented in this work demonstrate that it is possible to enlarge the cycle operating region also outside the inversion zone while conserving part of the advantages related to the use of BZT working fluids. This is done through a detailed study over a fixed airfoil by changing the freestream conditions of pressure, temperature and Mach number. At the same time, shape optimizations are conducted to show the best performances that it's possible to obtain with an airfoil, properly optimized for dense gas flows.

Inviscid and viscous turbulent flows of a dense gas over an airfoil at transonic speeds have been considered. Analyses of the variation of aerodynamic coefficients with free-stream thermodynamic conditions allow identifying three flow regimes in the range of thermodynamic conditions swept in present calculations, representative of the operating range of an Organic Rankine Cycle turbine. While the drag always increases with free-stream pressure and fundamental derivative Γ , the lift coefficient displays an optimum in the second regime, referred-to as low-pressure transonic BZT regime in the present study, and then drops dramatically. The lift-to-drag ratio is very poor for high Γ_∞ flows, but tends to infinity as the free-stream value of the Γ approaches unity from the high-pressure side of the inversion zone. The best compromise solution between high lift and low drag is obtained in the middle regime (the low-pressure BZT regime), for Γ_∞ approximately in the range $1 \div 1.3$: in these conditions, higher lift and significantly reduced wave drag

compared to perfect gas results is observed. Beneficial effects deriving from the use of a dense working fluid are also observed when the aerodynamic performance of viscous turbulent airfoil flows at large Reynolds number and transonic speeds is considered. The nonclassical variation of the Mach number with density favourably affects the boundary layer development, contributes to reducing friction drag and to avoiding boundary layer separation due to large adverse pressure gradients. Specifically, post-shock separations due to shock/boundary layer interaction are suppressed or greatly reduced, which ensures satisfactory lift and aerodynamic efficiency at flow conditions where the aerodynamic performance of perfect gas flows suffers from shock stall.

A shape optimization has been performed for inviscid transonic flows of dense gases over airfoils. Optimal airfoil shapes have been generated by using a multi-objective genetic algorithm coupled with a dense gas flow solver. Though computationally intensive, genetic algorithms are well adapted to the solution of multi-point optimization problems that arise naturally in dense-gas aerodynamics and allow generating airfoil shapes that ensure good performance over a large range of operating conditions. When solved for inviscid flow, the drag minimization problem of a symmetric airfoil with fixed thickness-to-chord ratio yields indeed shock-free shapes for an extended range of freestream Mach number; however, the optimal airfoils display a thick trailing edge that is bound to induce premature flow separation hence an increase in form drag when taking into account the viscous effects in the flow analysis. This point was actually checked by *a posteriori* numerical experiments using an available version of the SGS solver extended to the Reynolds-Averaged Navier-Stokes equations for dense gas flows. The multi-point performance optimization for a lifting airfoil in subcritical and supercritical flow conditions has allowed determining an airfoil shape that provides an overall improvement of the lift coefficient while preserving the high lift-to-drag ratio typical from BZT flows. However, in the case of inviscid flow optimization, it was again necessary to select an optimum shape within the optimal Pareto set that might ensure good performances also for viscous flows, thanks to a not-too-thick trailing edge, less prone to boundary layer separation.

Then, the previous shape optimization has been reconsidered for viscous transonic flows of dense gases over airfoils. Moreover, computational costs related to the great number of evaluations of the objective function by means of the Navier-Stokes solver have been substantially reduced by using a properly calibrated artificial neural network to interpolate the response surface. When solved for viscous flow, the drag minimization problem of a symmetric airfoil with fixed thickness-to-chord ratio yields indeed shock-free shapes for an extended range of the freestream Mach number. However, the problems generated by considering the viscous performances of airfoils produced by inviscid computations are completely overcome by including viscous effects into the optimization process, which provides an airfoil shape whose performance is far superior to the baseline over the whole range of Mach numbers considered for the study. The multi-point performance optimization for a lifting airfoil in subcritical and supercritical flow conditions has allowed determining an airfoil shape that provides an overall improvement of the lift coefficient while preserving the high lift-to-drag ratio typical from BZT flows. Once more, the results show the importance of taking fully into account viscous effects during the optimization process in order to obtain good performance over a large operation range. The overcost related to evaluations of the fitness function via a Navier-Stokes solver is completely justified by performance improvements offered by the optimized airfoils, and could be further alleviated by means of parallel computing. Moreover, significant improvement may be expected from the use of hybrid optimization algorithms, combining the flexibility of genetic strategies with the accuracy and efficiency of gradient-based methods.

Thirdly, shape optimization for flows of perfect and dense gases in turbine cascades has been achieved by means of a multi-objective genetic algorithm. For perfect gas flows, shape optimization allows efficiency improvements of about 3% over the baseline configuration. For dense gas flows, proper optimization starting from the same baseline geometry leads to efficiency gains up to 7%. Multipoint optimization allows improving performance over a large range of thermodynamic operating conditions. For the high cascade pressure ratio considered in this study, BZT effects play a minor role in efficiency improvement. The use of properly designed turbine cascades working with somewhat lower pressure ratios could allow higher efficiency improvements due to BZT effects, opening the door to the development of BZT turbines for Organic Rankine Cycles.

Finally, a detailed analysis of GA convergence for shape optimization problems in perfect and real gas flows has been considered. Specifically, a set of drag minimization problems for a symmetric non-lifting airfoil are considered. A statistical tool, namely, the fitness distance correlation (FDC) parameter, has been introduced: FDC measures how difficult is for a GA to converge toward the global optimum for a given problem. Numerical results show that problems characterized by low values of the FDC tend to stagnate in the vicinity of the global optimum without ever reaching it, and are therefore quite sensitive to the starting population used to initialize the GA, and to numerical parameters such as the computational grid and numerical scheme used to solve the flow governing equations. Analysis of the flow physics shows that the greatest convergence difficulties (and the lowest FDC parameter) are encountered for optimization problems such that airfoil shapes close to the optimum generate flow-fields characterized by extremely weak shocks. For this kind of flows, numerical viscosity acts as a low-pass filter that levels many different airfoil shapes to almost the same degree of fitness, slowing down or preventing at all GA convergence toward the optimum. This is particularly true for flows of BZT gases, whose peculiar property is to give rise to flow discontinuities much weaker than those characterizing perfect-gas flows. In order to improve GA convergence and to reduce its sensitivity to the starting population it is recommended to use high-accurate numerical schemes and fine meshes (as much as allowed by CPU time available to complete an optimization run), in order to minimize numerical errors on the fitness function. A very efficient objective-function evaluation procedure based on Richardson extrapolation is proposed, allowing to drastically reduce GA-hardness with a very moderate increase in computational cost of optimization runs.

Suggestion for futures study

The future study could concern the extension of this work to the 3D case. Then, first a detailed analysis of a 3D dense gas flow over an isolated airfoil and a turbine blade would be necessary. A 3D optimization of a turbine blade could produce the first 3D blade, conceived for an ORC, by taking into full account dense gas effects.

6. Bibliography

- [1] H. A. Bethe. The theory of shock waves for an arbitrary equation of state. Technical Report 545, Office of Scientific Research and Development, 1942.
- [2] Y. B. Zel'dovich. On the possibility of rarefaction shock waves. *Zh. Eksp. Teor. Fiz.*, 4:363–364, 1946.
- [3] Martin, J. J. & Hou, Y. C. 1955, “Development of an equation of state for gases”, *AIChE J.* 1,142-151.
- [4] Thompson, P.A., “A Fundamental Derivative in Gas Dynamics,” *Physics of Fluids*, Vol. 14, No. 9, 1971, pp. 1843-1849
- [5] Lambrakis, K.C., Thompson, P.A., “Existence of real fluids with a negative Fundamental Derivative ”, *Physics of Fluids*, Vol. 15, No. 5, 1972, pp. 933-935.
- [6] Thompson, P.A., Lambrakis, K.C., “Negative shock waves”, *Journal of Fluid Mechanics*, Vol. 60, 1973, pp. 187-208.
- [7] A. A. Borisov, Al. A. Borisov, S. S. Kutateladze, and V. E. Nakaryakov. Rarefaction shock waves near the critic liquid-vapour point. *J. Fluid Mech.*, 126:59–73, 1983.
- [8] Cramer, M.S., and Kluwick, A., “On the Propagation of Waves Exhibiting Both Positive and Negative Nonlinearity,” *Journal of Fluid Mechanics*, Vol. 142, 1984, pp. 9-37.
- [9] Chung, T.H., Lee, L.L. and Starling, K.E., “Applications of Kinetic Gas theories and Multiparameter Correlation for Prediction of Dilute Gas Viscosity and Thermal Conductivity”, *Industrial Engineering Chemistry Fundamentals*, Vol. 23, 1984, pp. 8-23.
- [10] M. S. Cramer and R. Sen. Shock formation in fluids having embedded regions of negative nonlinearity. *Phys. Fluids*, 29:2181–2191, 1986.
- [11] M. S. Cramer and R. Sen., Exact solutions for sonic shocks in van der Waals gases, *Physics of Fluids* -- February 1987 -- Volume 30, Issue 2, pp. 377-385
- [12] S. S. Kutateladze, V. E. Nakoryakov, and A. A. Borisov. Rarefaction waves in liquid and gas-liquid media. *Ann. Rev. Fluid Mech.*, 19:577–600, 1987.

- [13] Chung, T.H., Ajlan, M., Lee, L.L. and Starling, K.E., “Generalized Multiparameter Correlation for Prediction of Dilute Gas Viscosity and Thermal Conductivity”, *Chemistry Research*, Vol. 27, 1988, pp. 671-679.
- [14] Cramer, M.S., “Negative nonlinearity in selected fluorocarbons”, *Physics of Fluids A*, Vol. 1, No. 11, 1989, pp. 1894-1897.
- [15] Cramer, M.S., “Shock Splitting in Single-Phase Gases,” *Journal of Fluid Mechanics*, Vol. 199, 1989, pp. 281-296.
- [16] Cramer, M.S., and Best, L.M., “Steady, Isentropic flows of Dense Gases in Cascade Configurations,” *Phys. Fluids A*, Vol. 3, No. 1, 1991, pp. 219-226.
- [17] Cramer, M.S., and Crickenberg, A., “The dissipative structure of shock waves in dense gases”, *Journal of Fluid Mechanics*, Vol. 223, 1991, pp. 325-355.
- [18] Morren, S., “Transonic Aerodynamics of dense gases”, Master’s Thesis, Engineering Science and Mechanics Department, Virginia Polytechnic Institute and State University, 1991
- [19] Cramer, M.S., and Tarkenton, G.M., “Transonic Flows of Bethe-Zel’dovich-Thompson Fluids,” *Journal of Fluid Mechanics*, Vol. 240, 1992, pp. 197-228.
- [20] Emanuel, G. 1994 Assessment of the Martin–Hou equation for modelling a nonclassical fluid. *J. Fluids Eng.* **116**, 883–884.
- [21] Cramer, M.S., and Whitlock, S., Tarkenton, G., “Transonic and boundary layer similarity laws in dense gases”, *Journal of Fluid Eng*, Vol. 118, 1996, pp. 481-485.
- [22] Monaco, J.F., Cramer, M.S., and Watson, L.T., “Supersonic Flows of Dense Gases in Cascade Configurations,” *Journal of Fluid Mechanics*, Vol. 330, 1997, pp. 31-59.
- [23] Rusak, Z., Wang, C., “Transonic Flows of Dense Gases around an airfoil with a parabolic nose,” *Journal of Fluid Mechanics*, Vol. 346, 1997, pp. 1-21.
- [24] Brown, B., Argrow, B., “Two-dimensional shock tube flow for dense gases”, *Journal of Fluid Mechanics*, vol. 349, Issue 01, p.95-115
- [25] Wang, C.W., Rusak, Z., “Similarity Solutions of $\phi_x^3 \phi_{xx} = \phi_{\bar{y}\bar{y}}$ with Applications to Transonic Aerodynamics of Dense Gases”, *SIAM Journal of Applied Mathematics*, Vol. 59, No. 2, 1998, pp. 514-528.

- [26] Wang, C., Rusak, Z., , “Numerical Studies of transonic BZT gas flows around thin airfoils”, *Journal of Fluid Mechanics*, Vol. 396, 1999, pp. 109-141.
- [27] Cramer, M.S., and Park, S., “On the suppression of shock-induced separation in Bethe-Zel’dovich-Thompson fluids”, *Journal of Fluid Mechanics*, Vol. 393, 1999, pp. 1-21.
- [28] Brown, B.P., and Argrow, B.M., “Application of Bethe-Zel’dovich-Thompson Fluids in Organic Rankine Cycles,” *Journal of Propulsion and Power*, Vol. 16, No. 6, 2000, pp. 1118-1124.
- [29] Rusak, Z., and Wang, C.W., “Low-Drag Airfoils in Transonic Flows of Dense Gases”, *Zeitschrift für angewandte Mathematik und Physik (ZAMP)*, vol. 51, 2000, pp. 467-480.
- [30] G. Angelino and P. Colonna, “Organic Rankine cycles for energy recovery from molten carbonate fuel cells,” in *35th Intersociety Energy Conversion Engineering (IECEC)*, (Las Vegas, NV), pp. 1-11, AIAA, July 2000
- [31] Kluwick, A., “Marginally separated flows in dilute and dense gases”, *Phil. Trans. R. Soc. Lond.*, Vol. 358, 2000, pp. 3169-3192.
- [32] Ferguson, S., Argrow, B., “Construction and operation of a dense gas shock tube”, AIAA-2001-2747 , AIAA Thermophysics Conference, 35th, Anaheim, CA, June 11-14, 2001
- [33] S. H. Ferguson, T. L. Ho, B. M. Argrow, and G. Emanuel. Theory for producing a single-phase rarefaction shock wave in a shock tube. *J. Fluid Mech.*, 445:37–54, 2001.
- [34] P. Colonna and P. Silva, “Dense gas thermodynamic properties of single and multi-component fluids for fluid dynamics simulations,” *J. Fluids Eng.*, vol. 125, pp. 414-427, May 2003.
- [35] S. H. Ferguson, A. Guardone, and B. M. Argrow. Construction and validation of a dense gas shock tube. *J. Thermophys. Heat Tr.*, 17(3):326–333, 2003.
- [36] Kluwick, A., Wrabel, M., “Shock boundary layer interactions in dense gases”, *PAMM*, Vol. 4, 2004, pp. 444-445.

- [37] P. Colonna and S. Rebay, "Numerical simulation of dense gas flows on unstructured grids with an implicit high resolution upwind Euler solver," *Int. J. Numer. Meth. Fluids*, vol. 46, no. 7, pp. 735-765, 2004.
- [38] A. Guardone, L. Vigevano, and B. M. Argrow. Assessment of thermodynamic models for dense gas dynamics. *Phys. Fluids*, 16(11):3878–3887, 2004.
- [39] Cinnella, P., Congedo, P.M., "Numerical Solver for Dense Gas flows", *AIAA J.*, Vol. 43, No. 11, 2005, pp. 2458-2461
- [40] Cinnella, P., Congedo, P. M., , "Aerodynamic Performance of transonic Bethe-Zel'dovich-Thompson flows past an airfoil", *AIAA J.*, Vol. 43, 2005, pp. 370-378.
- [41] P.Cinnella, P.M.Congedo, 2005, "Inviscid and viscous behavior of dense gas flows past an airfoil", *J. Fluid Mech.* 580(2007), 179-217.
- [42] P.M. Congedo, C. Corre, P. Cinnella, 2005,"Airfoil shape optimization for transonic flows of Bethe-Zel'dovich-Thompson fluids". Accepted for publication in *AIAA Journal*.
- [43] Congedo P M, "Optimisation de forme pour des écoulements de gaz denses", (in french), Master's Thesis ENSAM (Paris), Spring 2005.
- [44] Cinnella, P., "Roe-type schemes for dense gas flow computations", *Computer and Fluids*, 2005
- [45] A. Guardone and B. M. Argrow. Nonclassical gasdynamic region of selected fluorocarbons. *Phys. Fluids*, 17(11):116102–1–116102–17, 2005.
- [46] P.Cinnella, P.M. Congedo, 2006, "Optimal airfoil shapes for viscous dense gas flows", accepted for publication in *Computer and Fluids*
- [47] P.M. Congedo, P.Cinnella, , C. Corre, 2006, "Shape optimization for dense gas flows through turbine cascades", presented to the 4th International Conference on Computational Fluid Dynamics (ICCFD 4), Ghant, Belgium, July 2006
- [48] P.Cinnella, P.M. Congedo, 2006, "GA-Hardness of dense-gas flow optimization problems", Paper 522-151. Proceedings of 15th IASTED International Conference on Applied Simulation and Modelling, Rhodes, Greece, June 2006. ISBN: 0-88986-561-2, pp. 489-494

- [49] P. Colonna and A. Guardone, "Molecular interpretation of nonclassical gas dynamics of dense vapors under the van der Waals model," *Phys. Fluids*, vol. 18, pp. 056101-1-14, 2006
- [50] P. Colonna, N. R. Nannan, A. Guardone, and E. W. Lemmon, "Multiparameter equations of state for selected siloxanes," *Fluid Phase Equilib.*, vol. 244, pp. 193-211, 2006
- [51] A. Guardone and P. Colonna, "Point explosions in dense gases," in *9th AIAA/ASME Joint Thermophysics and Heat Transfer Conference*, (San Francisco, CA), pp. 1-10, AIAA, June 2006
- [52] C. Zamfirescu, A. Guardone, and P. Colonna, "Preliminary design of the FAST dense gas Ludwig tube," in *9th AIAA/ASME Joint Thermophysics and Heat Transfer Conference*, no. AIAA 2006-3249, (San Francisco, CA), pp. 1-14, AIAA, June 2006
- [53] P. Colonna, A. Guardone, J. Harinck, and S. Rebay. Numerical investigation of dense gas effects in turbine cascades. In 15th U.S. National Congress on Theoretical and Applied Mechanics Conference, Boulder, CO, 2006.
- [54] P. Colonna, S. Rebay, J. Harinck, and A. Guardone. Real-gas effects in ORC turbine flow simulations: influence of thermodynamic models on flow fields and performance parameters. In ECCOMAS CFD 2006 Conference, Egmond aan Zee, NL, 2006.
- [55] C. Zamfirescu, A. Guardone, and P. Colonna, "Numerical Simulation of the FAST Dense Gas Experiment," in *European Conference on Computational Fluid Dynamics* (P. Wesseling, E. Onate, and J. Périaux, eds.), pp. 1-17, ECCOMAS CFD 2006, TU Delft, September 2006.
- [56] Cramer, M.S., "Rayleigh processes in single-phase fluids", *Phys. Fluids* **18**, 016101 (2006).
- [57] P. Cinnella, P.M. Congedo, 2007, "GA-Hardness of Aerodynamic Optimization Problems: Analysis and Proposed Cures", accepted to the 37th AIAA Fluid Dynamic Conference, Miami, June 2007.
- [58] Y. Davidor, *Epistasis variance: A viewpoint on GA hardness* (Foundations of genetic algorithms, edited by Rawlins, G.J.E, Morgan Kaufmann publishers, Inc, pp 23-35, 1991).

- [59] S. Rochet, M. Slimane, G. Venturini, Epistasis for encoding in genetic algorithms. *Australian and New Zeland Conference on Intelligent Information Systems, IEEE ANZIIS'96*, Adelaide (Australie), 1996, 268-271.
- [60] T. Jones, S. Forrest, Fitness distance correlation as a measure of problem difficulty for genetic algorithms. *Proceedings of the 6th international conference on genetic algorithms*, San Francisco, CA, 1995, 184-192.
- [61] Naudts, B., "Measuring GA-Hardness", Ph.D. Thesis, University of Antwerpen.
- [62] Horn, J., Goldberg, D. E., & Deb, K. (1994). Long path problems. In Y. Davidor, H.-P. Schwefel, & R. Manner (Eds.), *Proceedings of the 3rd conference on parallel problem solving from nature* (p. 149-158). Springer Verlag.
- [63] Wilcox D, "Turbulence Modeling for Cfd", D C W Industries.
- [64] Chung, T.H., Lee, L.L. and Starling, K.E., "Applications of Kinetic Gas theories and Multiparameter Correlation for Prediction of Dilute Gas Viscosity and Thermal Conductivity", *Industrial Engineering Chemistry Fundamentals*, Vol. 23, 1984, pp. 8-23.
- [65] Chung, T.H., Ajlan, M., Lee, L.L. and Starling, K.E., "Generalized Multiparameter Correlation for Prediction of Dilute Gas Viscosity and Thermal Conductivity", *Chemistry Research*, Vol. 27, 1988, pp. 671-679.
- [66] Jameson, A., Schmidt, W., and Turkel E., "Solutions of the Euler Equations by Finite Volume Methods Using Runge-Kutta Time-Stepping Schemes," AIAA Paper 81-1259, June 1981.
- [67] Rezgui, A., Cinnella, P., and Lerat A., "Third-order finite volume schemes for Euler computations on curvilinear meshes", *Computers & Fluids*, Vol. 30, No. 7-8, 2001, pp. 875-901.
- [68] Harten, A., Lax, P.D., van Leer, B., "On upstream differencing and Godunov-type schemes for hyperbolic conservation laws", *SIAM Review*, vol. 25, 1983, pp. 35-61.
- [69] Van Leer, B., "Towards the ultimate conservative difference scheme. V. A second-order sequel to Godunov's method", *Journal of Computational Physics*, vol. 32, 1979, pp. 101-136.

- [70] Barth, T.J., Jespersen, D.C., “The design and application of upwind schemes on unstructured meshes”, AIAA Paper 89-0366 (1989).
- [71] Venkatakrishnan, V., “Convergence to steady-state solutions of the Euler equations on unstructured grids with limiters”, *Journal of Computational Physics*, vol. 118, 1995, pp. 120-130.
- [72] Luo, H., Baum, J., Löhner, R., “A fast, matrix-free implicit method for compressible flows on unstructured grids”, *Journal of Computational Physics*, vol. 146, 1998, pp. 664-690.
- [73] Wang, J.F., Periaux, J., Sefrioui, M., “Parallel evolutionary algorithms for optimization problems in aerospace engineering”, *Journal of Computational and Applied Mathematics*, 149, 2002, pp. 155-169.
- [74] Giannakoglou, K.C., “Design of optimal aerodynamic shapes using stochastic optimization methods and computational intelligence”, *Progress in Aerospace Sciences*, Vol. 38, 2002, pp. 43-76.
- [75] Peigin, S., Epstein, B., “Robust optimization of 2D airfoils driven by full Navier-Stokes computations”, *Computers and Fluids*, Vol. 33, No. 9, 2004, pp. 1175-1200.
- [76] Pulliam, T.H., Nemec, N., Holst, T., Zingg, D.W., “Comparison of Evolutionary (Genetic) Algorithm and Adjoint Methods for Multi-Objective Viscous Airfoil Optimization”, AIAA Paper 2003-0298, 41st Aerospace Sciences Meeting, Reno (NV), January 6-10, 2003.
- [77] Deb, K., *Multi-objective Optimization Using Evolutionary Algorithms*, Wiley, 2001.
- [78] Srinivas, N., Deb, K., “Multiobjective function optimization using nondominated sorting genetic algorithms”, *Evolutionary Computation*, Vol. 2, No 3, 1995, pp. 221-248.
- [79] Rigoni, E., “Bounded BFGS”, Technical Report 2003-007, Esteco.
- [80] Haykin, S., *Neural Networks: a Comprehensive Foundation*, 2nd ed., Prentice Hall International, Upper Saddle, NJ, 1999.
- [81] Z. Michalewicz. *Genetic Algorithms + Data Structures = Evolution Programs*. Springer, Berlin, 1996.

- [82] Roache, P.J., "Verification and Validation in Computational Science and Engineering", Hermosa Publishers, Albuquerque, New Mexico, 1998.
- [83] R. Kiock et al.: ASME J. Eng. Gas Turb. Power 108.